Department of Physics "E. Amaldi"

Università degli Studi Roma Tre

Doctoral School in Mathematical and Physical Sciences

A DESIGN STUDY OF THE PRODUCTION OF Z BOSONS IN ASSOCIATION WITH B JET IN FINAL STATES WITH MUONS WITH THE ATLAS DETECTOR AT THE LHC

Director of the Ph.D. School

prof. Guido Altarelli

Supervisor

prof. Filippo Ceradini

Sara Diglio

A.A. 2008

A nonna Maria

Mondo

Angolo eterno,
la terra ed il cielo.
Per bisettrice il vento.

Angolo immenso,
il dritto sentiero.
Per bisettrice il desiderio.

Le parallele si incontrano
nel bacio.
Oh cuore
senz'eco,
in te inizia e finisce
l'Universo!

Federico Garcia Lorca

Contents

Introduction

The Large Hadron Collider (LHC) is the machine that will provide the highest ever produced energy in the center of mass, reaching the value of $\sqrt{s}$=14 TeV for proton-proton collisions and giving the possibility to produce particles with mass up to few TeV. The main aim of the LHC experiments is the search for the Higgs boson, which is fundamental to verify the symmetry-breaking mechanism in the electroweak sector of the Standard Model Theory. In addition the LHC experiments will explore the existence and the predictions of possible supersymmetric models and will perform precision measurements of the heavy quarks.
Four experiments are actually under commissioning phase on the LHC: ATLAS and CMS are two general purpose experiments, LHCb is mainly dedicated to CP symmetry violation studies and ALICE is going to exploit the heavy ions physics.
The work presented in this thesis is carried on in the framework of the ATLAS experiment. It presents a study of the prospects for measuring the production of a Z boson in association to b jet. This process is interesting in its own and also as background for many Standard Model and beyond Standard Model physics processes.
The wide kinematic range for production of Z + b jet serves as a testing ground for perturbative QCD predictions. In addition the cross section is sensitive to the b quark content in the proton and its precise measurement will help in reducing the current uncertainty on the partonic content of the proton (PDF's). Such uncertainty is presently affecting the potential for discovering new physics at LHC.

The motivations to study this process at LHC appear even more evident from the comparison with the Tevatron cross sections [18]. First of all, the total cross section for Z+b production at LHC is about a factor of 50 larger than at the Tevatron. Moreover the cross section for Z+c production compared to Z+b is more important at Tevatron than at LHC. In general at the LHC, the relative importance of processes other than Z+b (such as Zc, Zq and Zg) is less relevant than at the Tevatron. Finally, the probability of mis-tagging a light jet as a heavy quark is smaller, therefore the LHC provides a cleaner environment for the extraction of the Z+b signal.

Z+b jet events will be also used to calibrate the calorimetric b jet energy measurements, profiting from the high statistics and a relative low and well known background. It will be possible to calibrate the calorimeters using jets reconstructed in the experiment, performing an "in situ calibration" [39–41].

The study of the pp $\rightarrow$ Z + b jet channel has been done considering the decay selection Z $\rightarrow \mu^+\mu^-$ and the identification of the b jet both in an inclusive mode and through the semi-leptonic decay of the b jet into muons. The choice of final states with muons is due to a better identification of the final state (through the isolated muons).
This thesis describes analysis strategies developed to extract the signal from his possible backgrounds and presents the results obtained. In this work computing tools were developed and tested extensively. The study was performed using the signal and background events modelled with Monte Carlo generators, many of which have been newly developed for the LHC analyses. Full and fast simulation of the Atlas detector was performed to obtain realistic estimates of the sensitivity of the measurements.

Chapter 1 is dedicated to a theoretical overview on the state of art in particle physics in order to introduce the topics that will be recovered in subsequent chapters.
A general overview of the ATLAS experiment is given in chapter 2.
Chapter 3 summarizes the software tools inside the Athena framework that have been used to perform the analysis.
Chapter 4 is dedicated to the studies performed using fully simulated data, while in chapter 5 the systematic studies on b PDF and mistagging of c jets using fast simulated samples are shown.
A summary of the main sources of systematic uncertainties on Z+ b jet cross section measument is discussed in chapter 6.

Chapter 1

Theoretical Overview

This chapter presents a basic overview of the Standard Model that describes the current understanding of fundamental matter particles and their interactions.

In the following I will briefly discuss the basic themes and limits of the Standard Model focusing the attention on the ones related to this thesis.

1.1 Standard Model of Particle Physics

The Standard Model (SM) of particle physics is the Quantum Field Theory (QFT) that today provides the best description of fundamental particles and their interactions. It identifies structureless, elementary particles that constitute all the observed matter in the universe: these are the *quarks* and *leptons*. The interactions between the quarks and leptons are mediated by particles called *gauge bosons*. The Standard Model provides the theoretical framework to calculate physical (measurable) quantities, explains observed phenomena, and make predictions that can be checked experimentally. It has been enormously successful in explaining and predicting the results: most of these predictions have been confirmed to spectacular precision (many at CERN, Fermilab, SLAC).

Despite its many successes, there is consensus among particle physicists that the Standard Model is not the final theory of particle physics.

1.1.1 Matter particles and force carriers

The Standard Model describes the constituents of matter and their interactions in terms of fundamental point-like particles. A peculiar property of particles is their internal angular

momentum called *spin*. The particles can be considered in two categories: the fundamental fermionic particles whose spin is $\frac{1}{2}\hbar$ and gauge bosons whose spin is 1 $\hbar$.
The matter is made of *fermions* called *quarks* and *leptons* and their interactions are described by the exchange of *gauge bosons*.

Flavor	Electric Charge (e)	Spin	Mass (GeV)	Baryon Number	L_e	L_μ	L_τ
Quarks							
u (up)	$+2/3$	$1/2$	0.0015–0.004	$1/3$	0	0	0
d (down)	$-1/3$	$1/2$	0.004–0.008	$1/3$	0	0	0
c (charm)	$+2/3$	$1/2$	1.15–1.35	$1/3$	0	0	0
s (strange)	$-1/3$	$1/2$	0.08–0.13	$1/3$	0	0	0
t (top)	$+2/3$	$1/2$	178	$1/3$	0	0	0
b (bottom)	$-1/3$	$1/2$	4.1–4.4	$1/3$	0	0	0
Leptons							
e (electron)	-1	$1/2$	0.511×10^{-3}	0	1	0	0
ν_e (electron neutrino)	0	$1/2$	$<3 \times 10^{-9}$	0	1	0	0
μ (muon)	-1	$1/2$	0.106	0	0	1	0
ν_μ (muon neutrino)	0	$1/2$	$<1.9 \times 10^{-4}$	0	0	1	0
τ (tau)	-1	$1/2$	1.78	0	0	0	1
ν_τ (tau neutrino)	0	$1/2$	$<1.8 \times 10^{-2}$	0	0	0	1
Gauge Bosons							
$W^\pm$ (charged weak)	± 1	1	80.403 ± 0.029	0	0	0	0
Z^0 (neutral weak)	0	1	91.1876 ± 0.0021	0	0	0	0
γ (photon)	0	1	0	0	0	0	0
g_i (i=1,...,8 gluons)	0	1	0	0	0	0	0
g (graviton)	0	2	0	0	0	0	0

Table 1.1: The fundamental particles of the Standard Model and some of their properties. L_e, L_μ, and L_τ are the electron, muon, and tau lepton numbers [1]. For every particle there is a corresponding antiparticle.

The properties of the Standard Model particles are summarized in Table 1.1.
The quarks and leptons can be arranged in generations (see Table 1.2).
Among the three quark generations a mixing mechanism exists that is parametrized by the Cabibbo-Kobayashi-Maskawa matrix (that will be discussed in section 1.2). The Standard Model does not explain the origin of such a mixing.
Analysis on the Z partial decay width into hadrons, leptons and neutrinos at LEP indicates

that there are exactly three families of light neutrinos (assuming lepton universality). Strict lower limits have been set on the mass of 4th generation quarks and leptons.

Generation 1	Generation 2	Generation 3
u	c	t
d	s	b
νe	ν_μ	ν_τ
e	μ	τ

Table 1.2: The fundamental particles of the Standard Model grouped into generations. The main difference between the generations is the masses of their particles.

Quarks do not exist as free particles: different combinations of quarks form the spectrum of particles called hadrons. This item will be discussed in more detail in section 1.3.1.

The weak bosons ($W^{\pm}$ and Z^0) and photon (γ) mediate the electroweak force. Gluons are the mediators of the strong force. An example of force exchange between quarks and gluons interacting through vector bosons is shown in figure 1.1.

1.1.2 Gauge Symmetries

The fundamental particle interactions described by the Standard Model are the following:

- *electromagnetic*;
- *weak*;
- *strong*.

These interactions can be described as a combination of three unitary gauge groups, denoted as SU(3) $\otimes$ SU(2) $\otimes$ U(1) [2]. The group SU(3) is the symmetry group of strong interactions, U(1) describes electromagnetic interactions, and SU(2) $\otimes$ U(1) represents the unified weak and electromagnetic interaction.

These symmetries are of prime importance in particle physics. To illustrate this point, consider that observables depend on the wave function squared ($|\Psi|^2$). If local gauge invariance holds, the transformation

$$\Psi \rightarrow \Psi' = e^{-i\chi(\vec{x},t)}\Psi \tag{1.1}$$

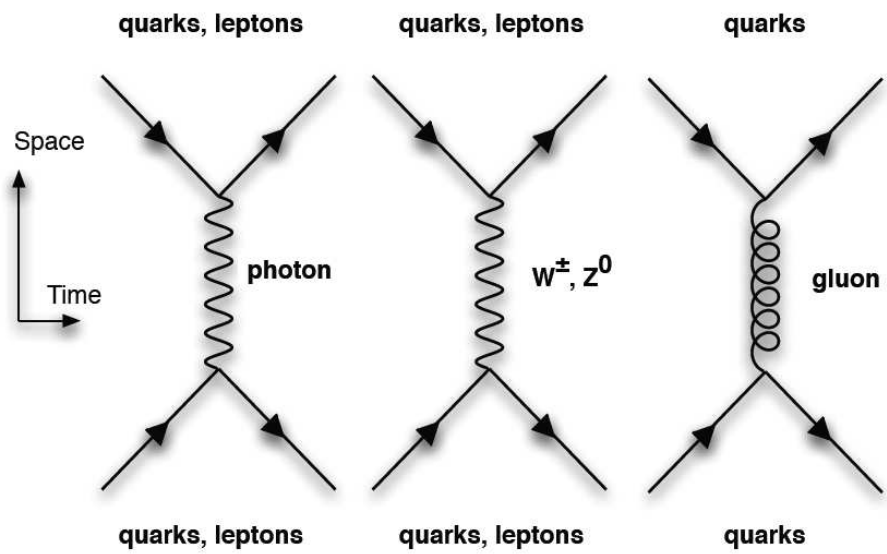

Figure 1.1: Feynman diagrams showing the basic forms of the electromagnetic, weak and strong interactions between two fermions mediated by the exchange of a photon, $W^{\pm}/Z^0$ and a gluon.

where $\chi(\vec{x},t)$ is an arbitrary phase which can depend on space and time coordinates, should leave the observables unchanged. Physically, since the absolute phase cannot be measured, the choice of phase should not matter. If one successively inserts Ψ and $\Psi^{'}$ into the Schrödinger equation for a matter particle,

$$\frac{1}{2m} \bigtriangledown^2 \Psi(\vec{x},t) = i\frac{\partial \Psi(\vec{x},t)}{\partial t}, \tag{1.2}$$

the equation is clearly not invariant under the transformation of equation 1.1.

To guarantee gauge invariance the Schrödinger equation should be modified. For electrically charged particles, the modified Schrödinger equation is

$$\frac{1}{2m}\left(-i\vec{\nabla} + e\vec{A}\right)^2 \Psi = \left(i\frac{\partial}{\partial t} + eV\right)\Psi, \tag{1.3}$$

where e is the electric charge, V is the electric potential, and $\vec{A}$ is the vector potential. With this change, the Schrödinger equation is invariant under the simultaneous transformations (1.1) and

$$A \rightarrow A^{'} = A + \frac{1}{e} \bigtriangledown \chi \tag{1.4}$$

$$V \rightarrow V' = V - \frac{1}{e}\frac{\partial \chi}{\partial t}. \tag{1.5}$$

Thus, the requirement that the theory be locally gauge invariant leads to the required presence of a field A^{μ} =(V;$\vec{A}$). Further, since particles are viewed as excitations of fields in this theory, the requirement of gauge invariance also leads to the presence of gauge bosons.

In the Standard Model, phase symmetries (mathematically, requirements that the theory be invariant under gauge transformations) are used to guide the construction of theories. The gauge fields and particles follow naturally from these symmetries.
The gauge theories introduced above involve only massless gauge bosons. However, massive gauge bosons ($W^{\pm}$,Z^0) have been observed experimentally. Evidence of a mechanism that causes the gauge bosons to acquire their masses is highly sought in particle physics. Currently, the leading candidate is the Higgs mechanism that will be discussed in section 1.2.1.

1.2 Electroweak Theory

The electroweak model is a gauge theory based on the *broken* symmetry group $SU(2)_L \otimes U(1)_Y$. The weak hypercharge (Y) is related to the third component of the weak isospin (I_3) and to the electric charge through the formula:

$$Q = I_3 + \frac{Y}{2} \tag{1.6}$$

The fermions are introduced in *left-handed (L)* doublets and *right-handed* (R) singlets. Handedness is related to the helicity of the fermion: the component of spin along its direction of motion. Quantum numbers of *left-handed* (L) and *right-handed* (R) fermions are summarized in table 1.3. The anti-fermions eigenvalues have opposite sign.

	$\nu_{eL}, \nu_{\mu L}, \nu_{\tau L}$	e_L, μ_L, τ_L	e_R, μ_R, τ_R	u_L, c_L, t_L	d'_L, s'_L, b'_L	u_R, c_R, t_R	d'_R, s'_R, b'_R
I	$\frac{1}{2}$	$\frac{1}{2}$	0	$\frac{1}{2}$	$\frac{1}{2}$	0	0
I_3	$+\frac{1}{2}$	$-\frac{1}{2}$	0	$+\frac{1}{2}$	$-\frac{1}{2}$	0	0
Y	-1	-1	-2	$+\frac{1}{3}$	$+\frac{1}{3}$	$+\frac{4}{3}$	$-\frac{2}{3}$
Q	0	-1	-1	$+\frac{2}{3}$	$-\frac{1}{3}$	$+\frac{2}{3}$	$-\frac{1}{3}$

Table 1.3: SU(2) $\otimes$ U(1) quantum numbers of left-handed and right-handed fermions.

The relation between the coupling costants of weak and electro magnetic interactions is

$$e = g \cdot \sin\theta_W \tag{1.7}$$

where e is the electric charge of the electron, g is the weak coupling costant, θ_W is the Weinberg's angle, that can be measured in the $\nu - e$ diffusion, or in the electroweak interference in e^+e^- processes between γ and Z exchange, or studying the Z width or also from the ratio between masses of the $W^\pm$ and of the Z.
The combined analysis of those experiments quoted the following result [1]:

$$\sin^2\theta_W = 0.23113 \pm 0.0005 \tag{1.8}$$

The W boson couples to quarks and lepton always with the same chiral status (*maximum parity violation*). The Z boson coupling depends also from the electric charge of fermions. The force of this coupling with a generic fermion f can be expressed as:

$$g_Z(f) = \frac{g}{\cos\theta_W} \cdot (I_3 - z_f \cdot \sin^2\theta_W) \tag{1.9}$$

where z_f is the electric charge of the fermion in elementary electric charge e units and I_3 is the third component of the weak isospin.

Coupling constants for left-handed or right-handed fermions are different (see table 1.4). They can be written as

$$g_L = I_3 - z_f \cdot \sin^2\theta_W \tag{1.10}$$

$$g_R = -z_f \cdot \sin^2\theta_W \tag{1.11}$$

	ν_e, ν_μ, ν_τ	e, μ, τ	u, c, t	d', s', b'
g_L	$\frac{1}{2}$	$-\frac{1}{2} + \sin^2\theta_W$	$\frac{1}{2} - \frac{2}{3} \cdot \sin^2\theta_W$	$-\frac{1}{2} + \frac{1}{3} \cdot \sin^2\theta_W$
g_R	0	$+\sin^2\theta_W$	$-\frac{2}{3} \cdot \sin^2\theta_W$	$\frac{1}{3} \cdot \sin^2\theta_W$

Table 1.4: Couplings between the Z boson and fermions

In addition, the mass eigenstates are not eigenstates of the weak interaction of quarks: they are mixed, parameterised by three mixing angles and one phase angle according to the Cabibbo-Kobayashi-Maskawa (CKM) formalism.

$$\begin{pmatrix} d' \\ s' \\ b' \end{pmatrix} = \begin{pmatrix} V_{ud} & V_{us} & V_{ub} \\ V_{cd} & V_{cs} & V_{cb} \\ V_{td} & V_{ts} & V_{tb} \end{pmatrix} \cdot \begin{pmatrix} d \\ s \\ b \end{pmatrix} \tag{1.12}$$

The values of the magnitudes of the elements of the matrix as quoted in [1], assuming the matrix is unitary, are

$$V_{CKM} = \begin{pmatrix} 0.9739-0.9751 & 0.221-0.227 & 0.0029-0.0045 \\ 0.221-0.227 & 0.9730-0.9744 & 0.039-0.044 \\ 0.0048-0.014 & 0.037-0.043 & 0.9990-0.9992 \end{pmatrix} \tag{1.13}$$

Each generation has a small off-diagonal mixing element leading to coupling between quarks of different generations. Flavor mixing in the lepton sector was in fact confirmed in 1998, implying that neutrinos have non-zero mass. However, this effect is even smaller than quark mixing and the coupling of leptons with different doublets is minute.

1.2.1 Electro Weak Symmetry Breaking

The electroweak model is passing experimental tests with high precision. However, the symmetry in the electroweak model requires all four bosons to be massless. This is obviously a broken assumption as we observe very massive weak bosons.
In 1964 Franois Englert, Robert Brout, Peter Higgs and independently Gerald Guralnik, C. R. Hagen, and Tom Kibble conjectured that the massless gauge bosons of weak interactions acquire their mass through interaction with a scalar field (the Higgs Field), resulting in a single massless gauge boson (the photon) and three massive gauge bosons ($W^{\pm}$ and Z^0) [3–5]. This is possible because the Higgs field has a potential function which allows degenerate vacuum solutions with a non-zero vacuum expectation value.
The interaction between the particle and this Higgs field contributes to the particles energy respect to the vacuum. This energy is equivalent to a mass. In the minimal Standard Model only a doublet of scalar fields is introduced. In the simplest model masses of quarks, leptons and bosons are all interpreted as the interaction with a unique scalar field. Particles which interact strongly are the heaviest, while particles that interacts weakly are lighter. There is always a particle associated to a quantum field, so the theory predicts the observation of a spin-0 Higgs boson which is now the only remaining particle to be discovered within the Standard Model.
Several theories have been proposed which include the Higgs mechanism to give the

gauge bosons masses. In those theories more than one Higgs boson is predicted. Among all the theories there is SuperSymmetry (SUSY) that will be briefly discussed in section 1.4.2.

1.2.2 Phenomenology of Higgs Boson

As it was discussed in the previous section, the Standard Model predicts the existence of a scalar neutral boson that is the results of the spontaneous electroweak symmetry breaking $SU_L(2) \otimes U_Y(1)$.
The Higgs boson couples to quarks and leptons with a force proportional to $(g \cdot m_f)/(2m_W)$ where g is the coupling costant of the gauge theory $SU_L(2)$ and m_f is the fermion mass.
The Higgs mass is related to the Higgs potential parameters v and λ as: $m_H = \sqrt{2v^2\lambda}$.
The parameter v is the vacuum expectation value of the Higgs field that is predicted by the theory v=246 GeV. In spite of this prediction the theory is not able to predict the value for the real parameter λ and as a consequence neither the value for the Higgs mass. It is possible only to fix some theoretical constraints to the Higgs particle mass as a function of the energy scale at which the Standard Model is valid. Those limits are shown in figure 1.2.

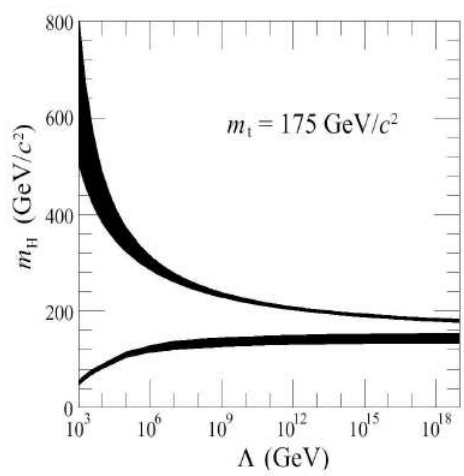

Figure 1.2: Theoretical limits on the Higgs boson mass as a function of the energy scale Λ until which the Standard Model is valid. The thickness of the bands indicates the theoretical uncertainties.

Figure 1.2 shows a very important feature: if the Higgs boson exists and his mass is between $\sim 150\ \frac{GeV}{c^2}$ and $\sim 180\ \frac{GeV}{c^2}$ the Standard Model could be valid until Planck mass scale $\sim 10^{19}\frac{GeV}{c^2}$.
From an experimental point of view, lower limits on m_H come from direct measurements done at Tevatron [19] and LEP (Large Electron Positron collider) [11]. A global fit on LEP and Tevatron data with m_H treated as free parameter is in figure 1.3. The global fit to the electroweak data gives $m_H = 84^{+34}_{-26}$ Direct searches at LEP gave a lower limit of $m_H > 114.3\ GeV$ at 95% confidence level.

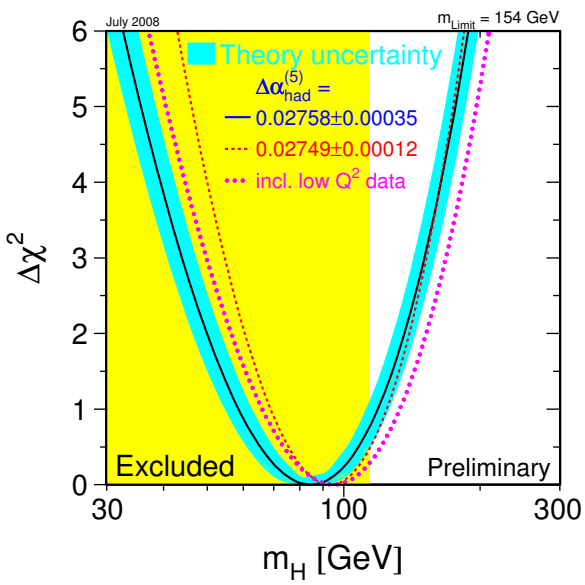

Figure 1.3: Global fit to the electroweak data as a function of m_H. The band represents an estimate of the theoretical error due to missing higher order corrections. The vertical band shows the 95% CL exclusion limit on m_H from the direct search. [11].

Thanks to the high luminosity and to an energy never reached by any other collider (14 TeV in the center of mass), at LHC it will be possible to investigate the origin of the spontaneous symmetry-breaking mechanism in the electroweak sector of the Standard Model looking for the Higgs boson.
The theoretical production cross sections for the Higgs boson at LHC as a function of the boson mass is shown in figure 1.4. Feynman diagrams of the principal production mechanisms at the LHC are shown in figure 1.5, while the Higgs Branching Ratios (BR)

decay channels as a function of the Higgs mass are shown in figure 1.6.

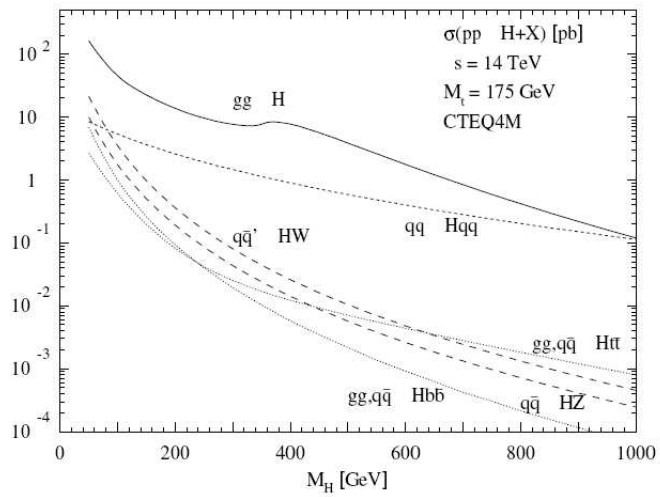

Figure 1.4: Production cross sections for the Higgs boson at LHC as a function of the boson mass.

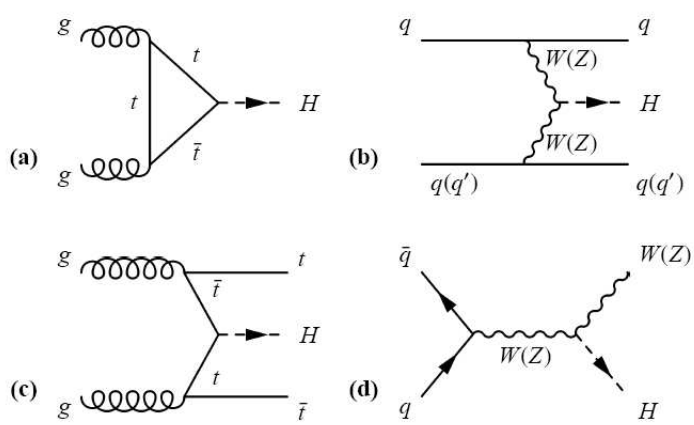

Figure 1.5: Diagrams of the main production processes of the Higgs boson: (a) gluon gluon fusion, (b) Z or W fusion, (c) associated production with $t\bar{t}$ pair, (d) associated production with a Z or W boson.

As it can be seen in figure 1.6 , for $m_H < 130$ GeV $H \to b\bar{b}$ is the most favourite channel, $b\bar{b}$ being the heaviest fermion pair accessible to the Higgs.

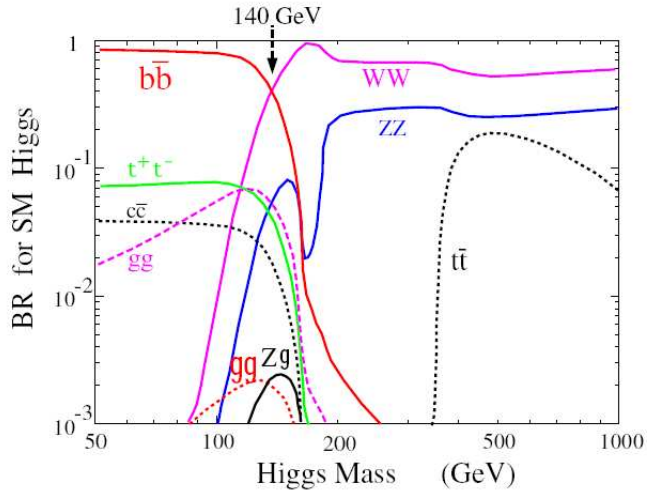

Figure 1.6: Branching Ratios of Higgs decays as a function of the Higgs mass.

I want to focus the attention on the process (d) in figure 1.5 when an Higgs is produced in assosiation to a Z boson: this process can be mimed by the process object of this thesis ($Z + b\,jets$) whenever b and $\overline{b}$ from the Higgs decay are not resolved as two different jets (see fig 1.7) [16, 17].

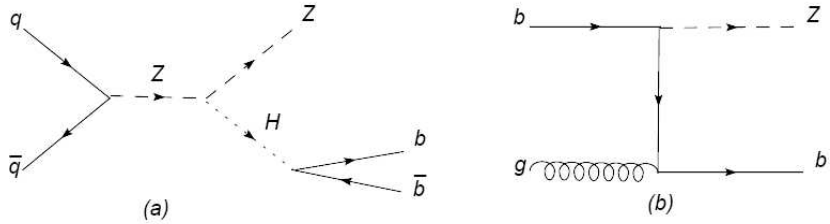

Figure 1.7: Diagrams: (a) associated production of an *Higgs* decaying into b with a Z boson; (b) associated production of a Z boson with a b-jet.

1.3 Theory of Strong Interaction

This section introduces the theory of the strong interactions also called *Quantum Chromo Dynamics* (QCD). The main features of QCD that are relevant to understand and describe

the hadron structure and calculate the evolution of partons that constitute hadrons will be discussed in the following.

1.3.1 Parton Model

According to the *Parton Model* the hadrons are strongly interacting particles built from *valence quarks* that define the quantum numbers (charge, spin, isospin) of the hadrons and from *sea quarks* that result from the gluon splitting inside the hadrons. The fundamental particles that constitue the hadrons (*quarks* and *gluons*) are called *partons*.
It is possible to distinguish between two different combinations of valence quarks that give origin to two different families of hadrons:

- **MESONS** $q\overline{q}$;
- **BARYONS** qqq (ANTI-BARYONS $\overline{qqq}$).

As an example the proton is a baryon made from the combination $\{\text{uud}\}$. The charge of the proton (in units of the electron charge) is the sum of the charges of its constituent quarks, $2/3+2/3+(-1/3)=+1$, its baryon number is 1, and its lepton number is 0 (baryon number and lepton number are additive quantum numbers. See Table 1.1). A neutron is made from the combination $\{\text{udd}\}$. It has electric charge $2/3+(-1/3)+(-1/3)=0$, baryon number 1, and lepton number 0. The success of the quark model in explaining and predicting other experimentally observed states led to its acceptance.
Despite this success, there are problem with this simplicistic description: the combination $\{\text{uuu}\}$ has been observed as the Δ^{++} baryon. The existence of the Δ^{++} presents a problem because its spin, $\text{J}=3/2$, is obtained by combining three identical fermions with the same quantum numbers. This violates Fermi statistics. Another problem is that neither combinations of more than three quarks or single quarks are observed.
The solution to these problems is the introduction of another quantum number called color. It can have one of three values, called red (R), green (G), and blue (B), with antiquarks having the values $\overline{\text{R}}$, $\overline{\text{G}}$, and $\overline{\text{B}}$. In QCD, bound states must be colorless, so mesons are formed from one quark and one antiquark which carry a color and its anti-color (like $\text{R}\overline{\text{R}}$), while baryons are formed from three quarks, one of each color, in an antisymmetric combination. Thus the Δ^{++} baryon consists of one u quark of each color.
Color is exchanged between quarks and gluons (both of which carry a color charge). Gluons are the mediators of the strong force. They are colored objects that carry color charge. Unlike photons, which mediate a force that gets weaker with distance, gluons are responsible for a binding force that strengthens with distance.

Gluons (and quarks) are colored, so cannot be observed directly because bound states are formed only as colorless objects. This behaviour is called color confinement. Eventually, when colored objects are pulled apart from other colored objects (as occurs in high-energy collisions), the energy released is converted into new colored objects, and colorless objects are formed from groups of the colored objects. Only colorless objects are observed in particle detectors and are detected as streams, or jets, of particles. It should be emphasized that leptons do not carry a color charge, and thus do not feel the strong force. This is the distinction between quarks and leptons.

1.3.2 Hadron-Hadron collision

According to QCD the observed hadrons are composite particles made of partons (quarks and gluons). The quarks and gluons are the fundamental degrees of freedom to participate in strong reactions at high energies. The collision between two hadrons (two protons at the LHC) can be described as an interaction between partons that constitute the hadrons. A scheme of this interaction is shown in figure 1.8.

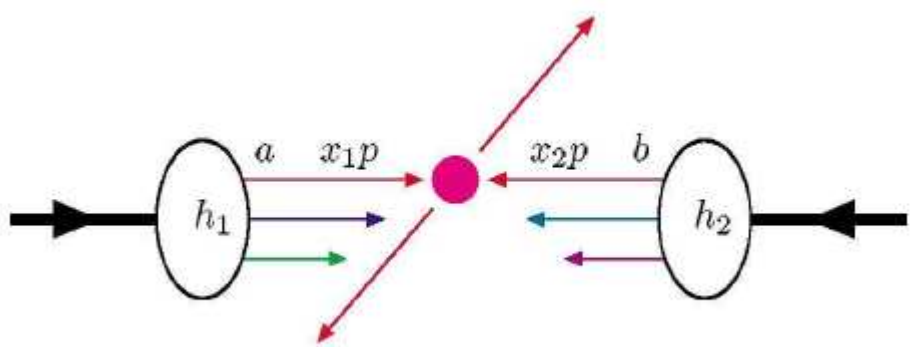

Figure 1.8: Simplified scheme of hadron-hadron interaction.

Scattering processes at high-energy hadron colliders can be classified as either hard or soft. Quantum Chromodynamics (QCD) is the underlying theory for all such processes, but the approach and level of understanding is very different for the two cases. For hard processes, e.g. Higgs boson or high p_T jet production, the rates and event properties can be predicted with good precision using perturbation theory. For soft processes the rates and properties are dominated by non-perturbative QCD effects, which are less understood.

Assuming that the masses of the partons are negligible and that the transferred quadri-momentum Q from the initial to the final state satisfied the relation $Q^2 \gg M^2$ (where M is the mass of the hadron), the *Bjorken scale variable* is defined:

$$x = \frac{Q^2}{2M\nu} \tag{1.14}$$

Being ν the energy transfer in the interaction, the x variable represents the fraction of the quadri-momentum of the hadron carried by the interacting parton.
The available energy in the center of mass of the collision, $\sqrt{\hat{s}}$, is related to the total energy in the center of mass $\sqrt{s}$ through the two Bjorken variables (one for each interacting parton) by the relation:

$$\hat{s} = x_1 x_2 s \tag{1.15}$$

where x_1 is the fraction of the quadri-momentum carried by the first parton belong to an interacting hadron and x_2 is the one carried by the second parton belong to the other interacting hadron (see fig. 1.8).

In the following I will discuss how the so called *QCD factorization theorem* can be used to calculate a wide variety of hard-scattering cross sections in hadron- hadron collisions. The QCD factorization theorem states that the cross sections of high energy hadronic reactions with a large momentum transfer can be factorized into a parton-level hard scattering convoluted with the parton distribution functions.
Theoretical predictions for processes at high transferred quadri-momentum Q are based on the following formula, which relies on the factorization theorem:

$$\sigma_{H_1 H_2} = \sum_{a,b} \int dx_1 dx_2 f_{a,H_1}(x_1, Q^2) f_{b,H_2}(x_2, Q^2) \times \hat{\sigma}_{a,b}(x_1, x_2, Q^2) \tag{1.16}$$

where $f_{c,H}(x, Q^2)$ is the parton density function (PDF) of the parton c carrying a fraction x of the hadron H momentum and $\hat{\sigma}_{a,b}$ is the parton-parton hard scattering cross-section describing the partonic reaction at the scale Q^2.

The parton-level hard scattering cross section can be calculated perturbatively in QCD, while the parton density functions parameterize the non-perturbative aspect and can be only obtained by some ansatz and by fitting the data.
A more detailed description of parton density function will be given in section 3.1.2.

1.4 Beyond the Standard Model

As said before there are indications that the Standard Model is not the final theory of particle physics and that more fundamental physics is left to be discovered. Experiments in the years ahead will give insight into which, if any, of the proposed theoretical extensions to the Standard Model is correct. In this section, a few of the reasons for the extensions are discussed.

1.4.1 Limitations of the Standard Model

One reason for introducing an extension to the Standard Model is revealed when calculations using the Standard Model framework include a Higgs boson. The inclusion of the Higgs boson in the theory leads to unphysical results in some calculations. Perturbative calculations of the mass of the Higgs boson squared have quadratic divergences. Infinite terms appear in the sum. It is theoretically possible to introduce counterterms in the perturbation series which cancel these divergences, but this has no physical justification, and is considered unnatural.

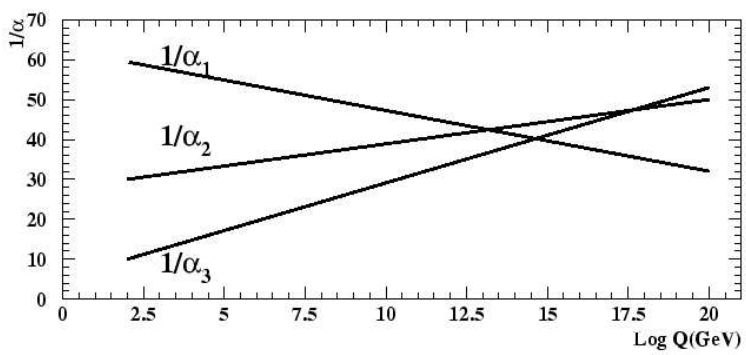

Figure 1.9: Evolution of the coupling strengths as a function of energy in the Standard Model, where α_1 corresponds to U(1) (electromagnetic force), α_2 corresponds to SU(2) (electroweak force), and α_3 corresponds to SU(3) (strong force). Diagram from [7].

A second reason arises from the fact that several theoretical unifications of forces have already occurred. Electricity and magnetism were once thought of as unrelated, as were the electromagnetic and weak forces. Thus, many theorists expect that a theory that unifies all of the forces should be the final theory. The Standard Model separates the unified electroweak forces from the strong force, and does not include gravity.
The fundamental forces are each characterized by a coupling strength. The coupling

strength appears in all physical calculations, and is indicative of the strength of the interaction. These coupling strengths have a dependence on the interaction energy; more precisely, they depend on the momentum transfer Q between two particles involved in an interaction. Figure 1.9 shows the values of the coupling strengths as a function of Q. Theoretical calculations in the Standard Model predict that the coupling strengths are closer at high energies than at lower energies. The experimental data taken so far agree. However, the coupling strengths will not meet exactly without the existence of some new physics which affects their dependence on the energy. Supersymmetry is one candidate for this new physics.

1.4.2 Super Symmetry

Supersymmetry is a proposed symmetry which relates fermions to bosons [**?**]. It postulates that for every particle there is a corresponding sparticle, identical to the particle but with a spin different by $1/2$. If it exists, supersymmetry must be a broken symmetry because no sparticles have been detected with masses equal to the Standard Model particles.

Supersymmetry solves the problems raised in section 1.4.1, including Higgs bosons to give mass to the particles. It introduces new terms into the calculation of the Higgs mass squared which cancel the terms that lead to the quadratic divergence. It also modifies the evolution of the coupling constants so that they unify at a high energy (see figure 1.10).

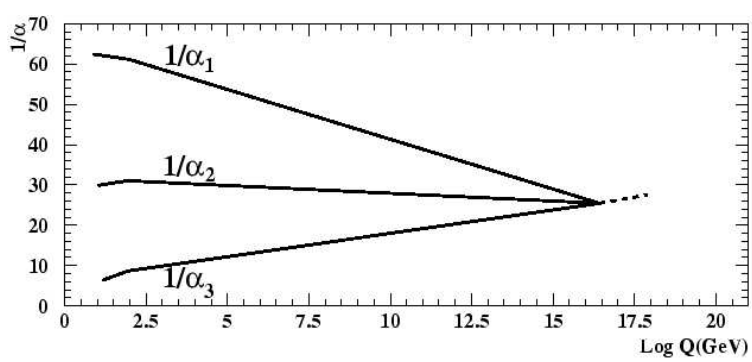

Figure 1.10: The evolution of the coupling strengths as a function of energy in supersymmetry, where α_1 corresponds to U(1) (electromagnetic force), α_2 corresponds to SU(2) (electroweak force), and α_3 corresponds to SU(3) (strong force).

An example of spectrum of supersymmetric sparticles corresponding to the particles

of the Standard Model is shown in table 1.5.

	Standard particles		**Supersymmetric partners**			
Electric charge	Particle	Spin	Sparticle	Spin	Sparticle name	Mass eigenstate
-1	e	$\frac{1}{2}$	$\widetilde{e}_L, \widetilde{e}_R$	0	selectron	
-1	μ	$\frac{1}{2}$	$\widetilde{\mu}_L, \widetilde{\mu}_R$	0	smuon	
-1	τ	$\frac{1}{2}$	$\widetilde{\tau}_L, \widetilde{\tau}_R$	0	stau	
0	ν=ν_e, ν_μ, ν_τ	$\frac{1}{2}$	$\widetilde{\nu}$	0	sneutrino	
-$\frac{1}{3}$,+ $\frac{2}{3}$	q=d,u,s,c,b,t	$\frac{1}{2}$	$\widetilde{q}_L, \widetilde{q}_R$	0	squark	
0	g	1	$\widetilde{g}$	$\frac{1}{2}$	gluino	
0	γ	1	$\widetilde{\gamma}$	$\frac{1}{2}$	photino	neutralinos
0	Z	1	$\widetilde{Z}^0$	$\frac{1}{2}$	zino	$\widetilde{\chi}_1^0$ ... $\widetilde{\chi}_4^0$
0	h^0,H^0,A^0	0	$\widetilde{H}_1^0, \widetilde{H}_2^0$	$\frac{1}{2}$	neutral higgsino	
±1	$W^\pm$	0	$\widetilde{W}^\pm$	$\frac{1}{2}$	wino	charginos
±1	$H^\pm$	0	$\widetilde{H}^\pm$	$\frac{1}{2}$	charged higgsino	$\widetilde{\chi}_1^\pm, \widetilde{\chi}_2^\pm$

Table 1.5: The particles of the Standard Model and their corresponding sparticles in supersymmetic models.

Note that in supersymmetry there are multiple Higgs bosons, and that the observable gauge sparticles are formed as mixtures of the superpartners of the Standard Model gauge particles. The superpartners are technically flavor eigenstates. There is one flavor eigenstate corresponding to each degree of freedom of the Standard Model particles. The observable spectrum of sparticles (the mass eigenstates) are linear combinations of the flavor eigenstates.

As it is visible from table 1.5 for each standard fermion (two helicity states) there are two superymmetric spin 0 partners: $\widetilde{f}_L$ and $\widetilde{f}_R$. These particles are called *sfermions* (*squarks, sleptons, sneutrinos*). For each gauge boson there is a superpartners of spin $\frac{1}{2}$ called *gaugino* (*wino, zino, photino*).
The strenght of interaction forces between these new particles are exactly the same of those between Standard Model particles.

If SUSY were an exact symmetry, supersymmetric partners should have the same masses as standard particles. The fact that we have not still observed supersymmetric particles can be traslated in the hypothesis that SUSY is an *hidden* or a *broken* symmetry.

Up to now we have not experimental observations of superparticles: this shoud mean that they are not existing particles or that their masses are not accessible with current available collider energies.

I want to focus the attention on the lighter Higgs (h). In the Standard Model, the production of a Higgs boson in association with b quarks is suppressed. However, in a supersymmetric theory for a large value of the ratio of the Higgs doublets vacuum expectation values (called $\tan\beta$), the b-quark Yukawa coupling can be strongly enhanced, and Higgs production in association with b quarks becomes the dominant production mechanism [17].

As it can be seen in figure 1.11, the process of a lighter susy Higgs produced in association to a b-jet can be mimed by the $Z + b\,jet$ process when the Z boson and the Higgs boson decay to the same final state ($b\bar{b}$,e^+e^-, $\mu^+\mu^-$, $\tau^+\tau^-$).

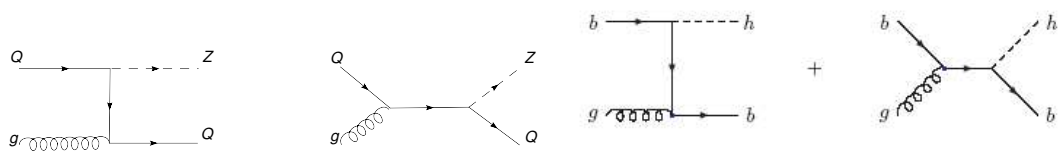

(a) (b)

Figure 1.11: (a) Associated production of a Z boson and a single heavy quark (Q=c,b), (b) associated production of the Higgs boson and a single bottom quark.

Chapter 2

Experimental Apparatus

2.1 The LHC Accelerator Complex

The Large Hadron Collider [10] is a proton proton collider that has been installed at CERN into the tunnel where the Large Electron Positron collider (LEP [11]) was.

Figure 2.1: The Large Hadron Collider.

The CERN existing accelerators (LINAC, BOOSTER, PS, SPS) are used to accelerate protons up to 450 GeV. After the injection into the LHC, the two beams will reach the energy of 7 TeV. In addition to the p-p operation, the LHC will be able to collide heavy nuclei (Pb-Pb) at an energy of 1125 TeV.

The LHC will provide a rich physics potential, ranging from the search for new physics phenomena to more precise measurements of Standard Model parameters. Furthermore, nucleus-nucleus collisions at the LHC provide an unprecedented opportunity to study the properties of strongly interacting matter at extreme energy density.
The two proton beams will travel in the opposite direction along two rings (the radius of each ring is about 4.2 Km) crossing each other in eight points. In four of these intersections there are the following detectors:

- ATLAS, **A** **T**oroidal **L**HC **A**pparatu**S**
- CMS, **C**ompact **M**uon **S**olenoid
- ALICE, **A** **L**arge **I**on **C**ollider **E**xperiment
- LHCb, **L**arge **H**adron **C**ollider **b**physics

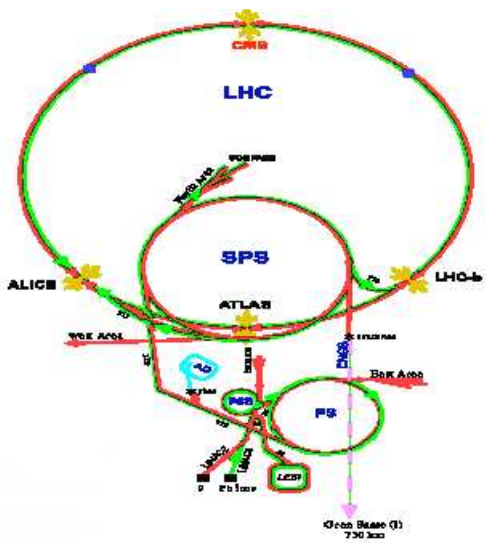

Figure 2.2: System to inject proton beams into the final collider LHC.

The two proton beams will pass through oppositely directed field of 8.38 Tesla. These fields are generated by superconducting magnets operating at 1.9 K. The protons will come in roughly cylindrical bunches, few centimeters long and few microns in radius. The distance between bunches is 7.5 m, in time 25 ns.In the high luminosity phase ($10^{34} cm^{-2} s^{-1}$), the two beams will be made of 2808 bunches of about 10^{11} protons each. During the initial phase, LHC will run at a peak lower luminosity of $10^{33} cm^{-2} s^{-1}$.

The uminosity $\mathscr{L}$ of a collider is a parameter of the machine that connects the interaction cross section (σ) with the number of events per unit time (N_e):

$$N_e = \mathscr{L}\sigma \tag{2.1}$$

The luminosity is related to the properties of the colliding beams and can be expressed in terms of the machine parameter:

$$\mathscr{L} = F\frac{fn_1n_2}{4\pi\sigma_x\sigma_y} \tag{2.2}$$

where the f is the particle bunch collision frequency, n_1 and n_2 are the number of particles per bunch, σ_x e σ_y are the parameters which characterise the beam profile in the directions orthogonal to the beam and F, equal to 0.9, depends on the crossing angle between the beams.
LHC could reach a design luminosity of $10^{34}cm^{-2}s^{-1}$: this is important to study processes with a small cross section value.

2.2 The ATLAS Detector

At the LHC the high interaction rates, radiation doses, particle multiplicities and energies, as well as the requirements for precision measurements have set new standards for the design of particle detectors.
ATLAS is a general-purpose detector designed to maximize the physics discovery potential offered by the LHC accelerator. Requirements for the detector system [12] have been defined using a set of processes covering much of the new phenomena which one can hope to observe at the TeV scale. In the following I will focus the attention in describing subdetectors that are fundamental for the reconstruction of the channel with a Z boson produced in association to a b-jet and the Z decaying into two muons of opposite charge.

2.2.1 The coordinate system and nomenclature

The coordinate system and nomenclature used for describing the detector and the particles emerging from the p-p collisions are briefly summarised here as they are used repeatedly throughout this thesis.
The beam direction defines the z-axis and the $x-y$ plane is transverse to the beam direction. The positive x-axis is defined as pointing from the interaction point to the centre of

the LHC ring and the positive y-axis is defined as pointing upwards. The side-A of the detector is defined as that with positive z and side-C is that with negative z.

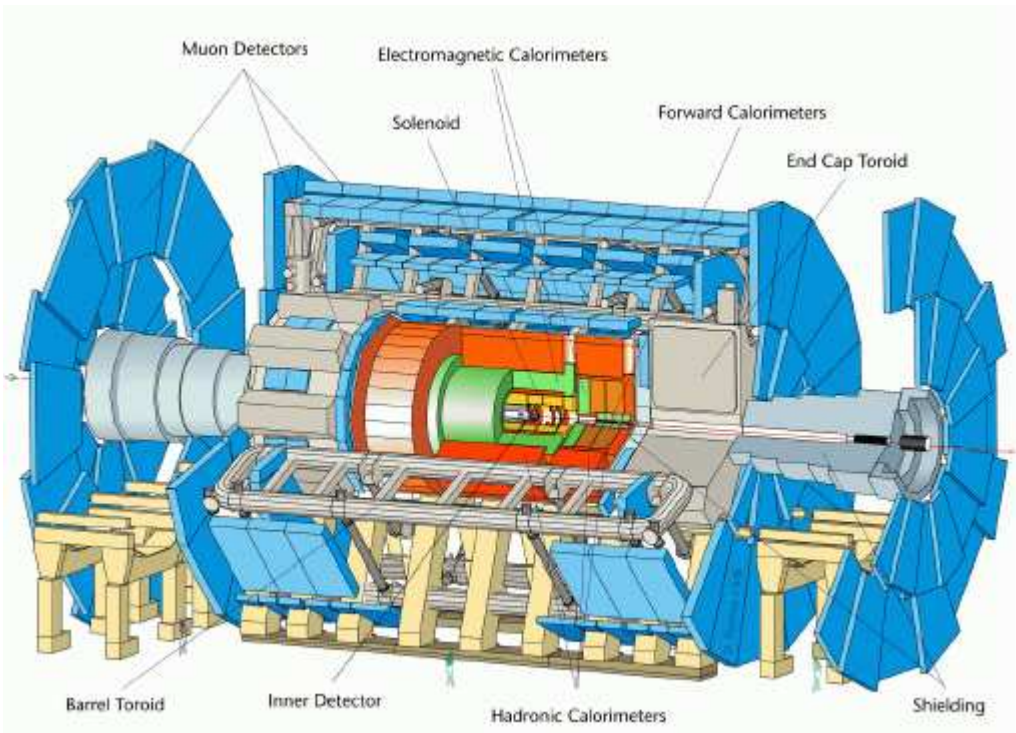

Figure 2.3: Schematic design of the ATLAS detector.

As it is shown in figure 2.3 the ATLAS has a cylindrical geometry, so it is useful to define a cylindrical coordinate system (z,R,ϕ) in order to measure particles coming from the collision: z is the position in the direction along the beam axis, R is the radius in the $x-y$ plane measured from the nominal interaction point and ϕ is the azimuthal angle measured around the beam axis. The relation between R and z can be expressed using the polar angle θ. The mathematical descriptions of these variables are the following:

$$R = \sqrt{x^2 + y^2} \tag{2.3}$$

$$\theta = \arccos \frac{z}{\sqrt{R^2 + z^2}} \tag{2.4}$$

$$\phi = \arctan \frac{y}{x} \tag{2.5}$$

A convenient set of kinematic variables for particles produced in hadronic collisions is the transverse momentum p_T , the rapidity y and the azymuthal angle ϕ. For a particle with energy E and three momentum $\vec{p} = \{p_x, p_y, p_z\}$

$$p_x = p_T \cos\phi, \qquad p_y = p_T \sin\phi, \qquad p_T = \sqrt{p_x^2 + p_y^2}, \qquad p_z = p_l. \tag{2.6}$$

Since the motion between the parton center of mass frame and the hadron laboratory frame is along the beam direction ($\vec{z}$), variables involving only the transverse components are invariant under longitudinal boosts. It is thus convenient to write the phase space element in cylindrical coordinates as

$$\frac{d^3\vec{p}}{E} = dp_x dp_y \frac{dp_z}{E} = p_T dp_T d\phi \frac{dp_z}{E} \tag{2.7}$$

Both p_T and ϕ are boost invariant, so is $\frac{dp_z}{E}$.

We can also write the phase space element in term of the rapidity variable defined as

$$y = \frac{1}{2} ln(\frac{E + p_z}{E - p_z}) \tag{2.8}$$

such as

$$\frac{d^3\vec{p}}{E} = p_T dp_T d\phi dy \tag{2.9}$$

The use of boost invariant variables facilitates the description of particle production in hadronic collisions, since these phenomena are approximately boost invariant for not too extreme values of rapidity. This fact is particularly simple to understand for high energy scattering phenomena, where the incoming hadrons behave as beams of quark and gluons, with a given distribution in longitudinal momenta and limited transverse momentum. It is clear that, depending upon the energy of the incoming constituents, the same hard scattering phenomenon can take place with an effective center of mass (i.e. with a center of mass for the incoming constituents) that is moving along the collision direction. Experimentally, it is convenient to use the pseudorapidity: the pseudorapidity η is defined as

$$\eta = -ln(\tan\frac{\theta}{2}) \tag{2.10}$$

In terms of momenta it can be definied as

$$\eta = ln(\frac{p + p_l}{p_T}) \tag{2.11}$$

Being only a function of the angle, pseudorapidity is much easier to measure than rapidity, and it is simple to proof that in the limit $p \gg m$,we obtain $\eta = y$.

The detector is geometrically divided in three sections:

Barrel: $|\eta| < 1.05$

Extended Barrel: $1.05 < |\eta| < 1.4$

Endcap: $|\eta| > 1.4$

Other variables useful to describe particles emerging from the interaction are the tranverse energy E_T, the missing transverse energy E_T^{miss} and the angular distance ΔR:

$$E_T = \sum \sqrt{p_x^2 + p_y^2} \tag{2.12}$$

$$E_T^{miss} = \sqrt{(\sum p_x)^2 + (\sum p_y)^2} \tag{2.13}$$

$$\Delta R = \sqrt{\Delta\eta^2 + \Delta\phi^2} \tag{2.14}$$

where the sum is over all particles originating from the interaction.

2.2.2 Physics requirements

The formidable LHC luminosity and resulting interaction rate are needed because of the small cross-sections expected for many of the processes mentioned above (see figure 2.4).

However, with an inelastic proton-proton cross-section of 80 mb, the LHC will produce a total rate of 10^9 inelastic events/s at design luminosity. This presents a serious experimental challenge as it implies that every candidate event for new physics will on the average be accompanied by $\sim$20 inelastic events per bunch crossing.
The nature of proton-proton collisions imposes another difficulty: jet production cross-section dominate over the rare processes mentioned above, requiring the identification of experimental signatures characteristic of the rare physics processes in question, such as E_T^{miss} or secondary vertices. Identifying such final states for these rare processes imposes further demands on the particle-identification capabilities of the detector and on the integrated luminosity needed. Viewed in this context, these benchmark physics goals can be turned into a set of general requirements for the detector:

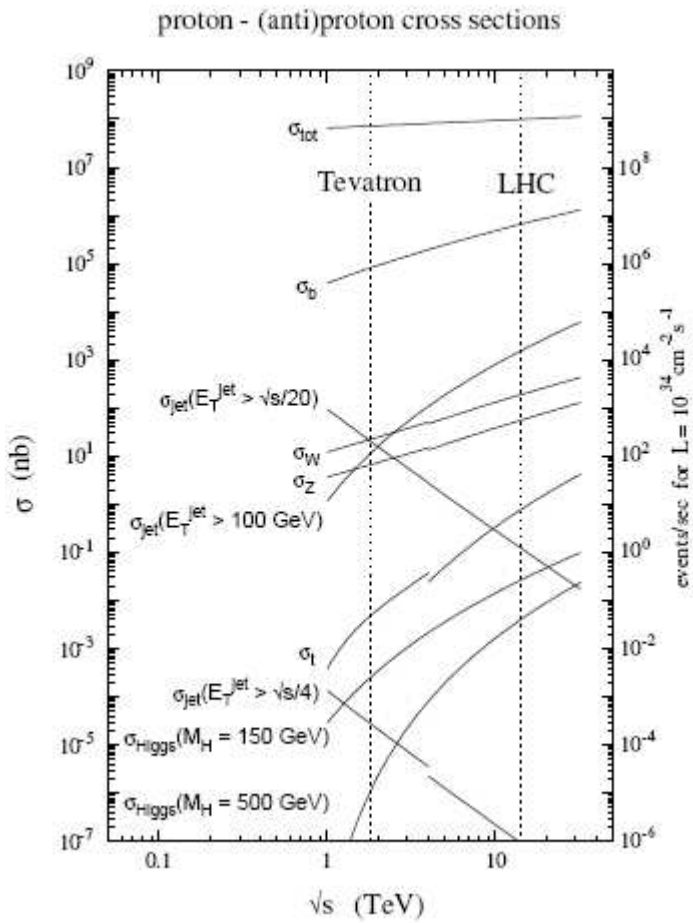

Figure 2.4: Proton-(anti)proton cross sections for several processes as a function of the center of mass energy.

- a good charged-particle momentum resolution and reconstruction efficiency in the inner tracker. For offline tagging of τ -leptons and b-jets, vertex detectors close to the interaction region are required to observe secondary vertices;

- a very good electromagnetic (EM) calorimetry for electron and photon identification and measurements;

- a full-coverage hadronic calorimetry for accurate jet and missing transverse energy measurements;

- an high precision muon system that guarantees accurate muon momentum measurements over a wide range of momenta;
- a very efficient trigger system on high and low transverse-momentum objects (*minimum bias* events) with sufficient background rejection.

ATLAS has been designed in order to satisfy these requeriments.
The magnetic system, subdetectors and the trigger system are briefly introduced in the following sections.

2.3 Magnetic System

The magnetic system consists of a central solenoid (CS) that provides a solenoidal field of 2 Tesla for the inner detector and three large air-core toroids, two in the end-caps (ECT) and one in the barrel (BT) that generate the magnetic field in the muon spectrometer (see figure 2.5).

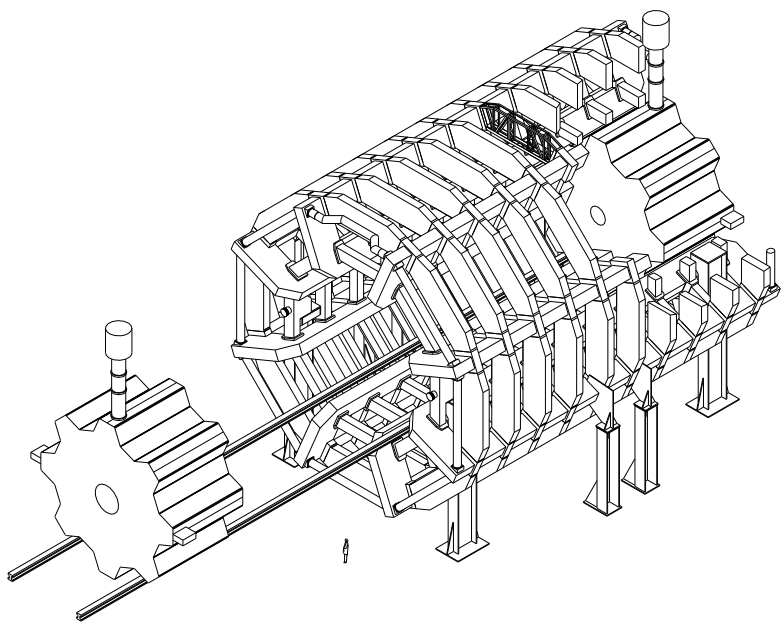

Figure 2.5: View of the superconducting air-core toroid magnet system.

The CS creates a solenoidal field with a nominal strength of 2 T at the interaction point. The real field provided by the CS is not uniform in z nor in R direction. The posi-

tion in front of the Electromagnetic calorimeter requires a careful minimisation of matter in order to avoid showering of particles before their enter the calorimeter.

The design of magnetic system was motivated by the need to provide the optimised magnetic field configuration while minimizing scattering effects.
The two end-cap toroids (ECT) are inserted in the barrel toroid (BT) at each end and line up with the central solenoid. Each of the three toroids consists of eight coils assembled radially and symmetrically around the beam axis.
Both BT and ECT generate a precise, stable and predictable magnetic field ranging from 3 to 8 Tm for the muon spectrometer. This field is produced in the barrel region ($|\eta| \leq 1.0$) by the BT and in the forward region ($1.4 \leq |\eta| \leq 2.7$) by the ECT, while in the transition region ($1.0 \leq |\eta| \leq 1.4$), it is produced by a combination of the two.
Due to the finite number of coils, the magnetic field provided by the toroids is not perfectly toroidal: it presents strong discontinuities in transition regions, as it can be seen in figure 2.6. The lines are drawn in a plane perpendicular to the beam axis in the middle of an end-cap toroid and the range between two consecutive lines is of 0.1 T.

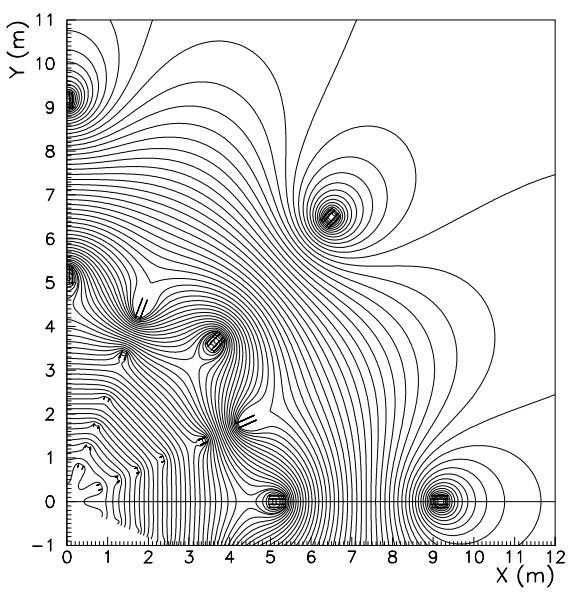

Figure 2.6: Magnetic toroid field map in the transition region, the lines are drawn in a plane perpendicular to the beam axis in the middle of an end-cap toroid.

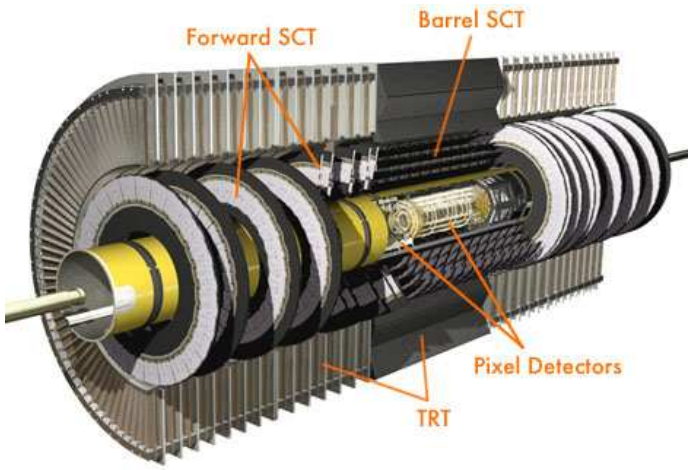

Figure 2.7: 3D view of the Inner Detector system.

2.4 Inner Detector

The inner detector (ID) is the innermost part of ATLAS and is designed to reconstruct the production and decay points (vertices) of charged particles as well as their tajectories (see figure 2.7).
It combines high resolution detectors (pixel) at the inner radii, with tracking elements at the outer radii covering the range of $|\eta| < 2.5$ and it is placed within a solenoidal magnetic field of 2T. The outer radius of the ID cavity is 115 cm and its length is 7 m.

The overall layout consists of three different technologies: the pixel detector, at radii between 5 and 15 cm from the interaction region and the silicon strip detector (SCT) at radii between 30 and 50 cm (both of which use semiconductor tracking technology) and the transition radiation tracker (TRT) at outer radii.

Performance requirements of the ID include [12]:

- Resolution: $\sigma_{P_T}/P_T = 0.05\% P_T \oplus 1\%$.
- Tracking efficiency better than 95% over the full coverage for isolated tracks with $P_T > 5$ GeV and a fake-track rate $\leq 1\%$ ($\leq 10\%$) of signal rates.
- At least 90% efficiency for reconstructing both primary ($P_T \geq 5$ GeV) and secondary ($P_T \geq 0.5$ GeV) electrons. For primary electrons both bremsstrahlung and trigger efficiency are taken into account.

- Tagging of b-jets by displaced vertex with an efficiency $\geq 40\%$. This is done with a rejection of non b-hadronic jets ≥ 50. (At low luminosity, efficiency $\geq 50\%$ for tagging b-jets).
- Identification of individual particles in dense jets and of electrons and photons that form similar clusters in the EM calorimeter. Combined efficiency of ID and EM calorimeter for photon identification should be $\geq 85\%$.

Pixel Detector

The pixel detector is the closest to the interaction point. It consists of three layers in the barrel and five disks in each end-cap. The system provides three precise measurements over the full solid angle (typically three pixel layers are crossed), with the possibility to determine the impact parameter and to identify short-life particles.
The required high resolution is provided by 140 millions individual square pixels of 50 μm in $r-\phi$ and 400 μm in z. The pixel detector yields excellent spatial resolution in the bending plane of the solenoidal magnetic field, essential for transverse momentum measurement. The position along the beam axis is measured with slightly less precision.

SCT

The semi-conductor tracker (SCT) is designed to provide eight precision measurements per track to determine momentum, impact parameter and vertex position. It consists of four double layers of silicon strips. It has a resolution of 17 μm in rϕ and 580 μm in z, and can resolve 2 parallel tracks separated by 200 μm or more: this permits to resolve ambiguities in the pattern recognition (assigning hits to track in the dense tracking environment).

TRT

The TRT constitutes the outermost part of the ID system. It consists of 36 layers of 4 mm diameter straw tubes interspaced with a radiator to emit transition radiation (TR) from electrons. The track density is relatively low at large radii giving a number of 36 points per track. This insures good pattern recognition performance.
The drift-time measurement gives a spatial resolution of 130 μm per straw as well as a low and a high threshold. Thus, the TRT can discriminate between transition radiation hits that have passed the high threshold, and tracking hits that have passed the low threshold.

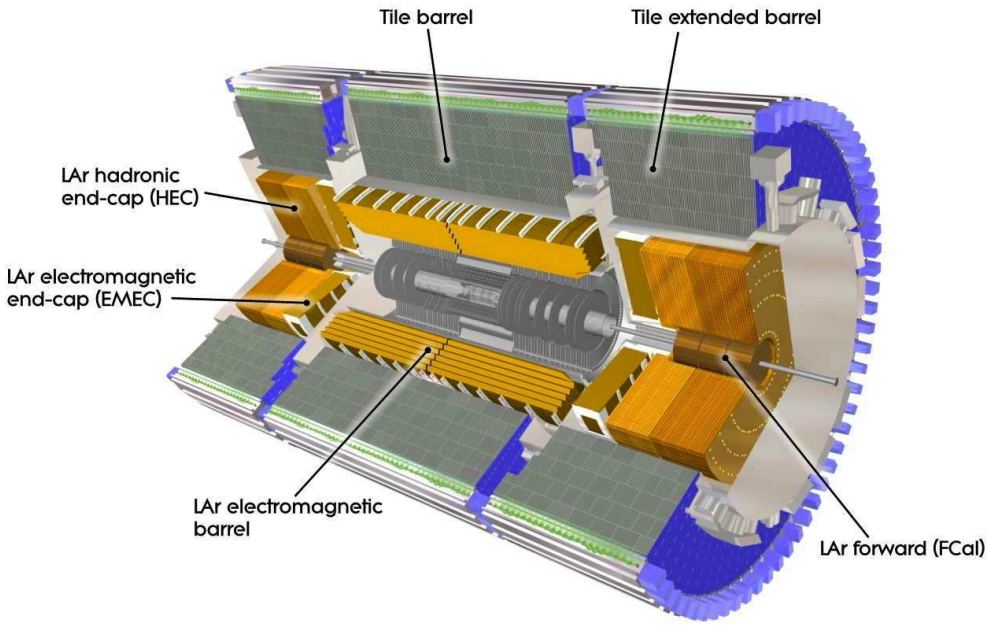

Figure 2.8: General layout of the calorimeters showing a good hermeticity.

2.5 Calorimeter System

The calorimeter (see figure 2.8) has been designed to provide measurements of the energy of electrons, photons, isolated hadrons and jets as well as missing transverse energy. It is divided into an Electromagnetic (EM) Calorimeter and a Hadronic Calorimeter each consisting of a barrel and two end-caps.
The Electromagnetic Barrel Calorimeter (EMB) covers the pseudorapidity $|\eta| < 1.475$, the Electromagnetic End-Cap Calorimeter (EMEC) covers $1.375 < |\eta| < 3.2$, the Hadronic End-Cap Calorimeter (HEC) covers $1.5 < |\eta| < 3.2$, the Forward Calorimeter (FCAL) covers $3.1 < |\eta| < 4.9$, and the Tile Calorimeter (TileCal) covers $|\eta| < 1.7$.

Because of its good hermeticity, the calorimeter as a whole provides a reliable measurement of the missing transverse energy (E_T^{miss}). Together with the Inner detector, the calorimeter provides a robust particle identification exploiting the fine lateral and good longitudinal segmentation.

Electromagnetic Calorimeter

The Electromagnetic Calorimeter is a highly granular lead-liquid argon sampling calorimeter with accordion-shaped lead absorbers and kapton electrodes. This geometry enables the detector to have a hermetically uniform azimuthal coverage.
The eletromagnetic shower develops in lead absorber plates. The absorbers are folded into an accordion shape and oriented along R (z in the end-caps) to provide complete ϕ symmetry without azimuthal cracks.
The total EM calorimeter presents a ~ 20 radiation lengths in the barrel and in the end-caps region to reduce the error in the energy resolution due to longitudinal fluctuations of high energy showers due to longitudinal leakage.
The particle identification is achieved by a fine longitudinal and lateral segmentation. The EM calorimeter is longitudinally segmented in three layers plus a pre-shower sampler that corrects the energy loss in the material in front of the EM.

The design of the electromagnetic calorimeter is driven by the requirements for energy and spatial resolution for the Higgs processes involving decays to electrons or photons for the detection of new gauge bosons (Z' or W') decaying to electrons. The dinamical range of electronics for the calorimeter extends from a few MeV for electrons from B-meson decays to a few TeV for the decay of a heavy vector boson. The ability to identify low energy electrons can improve b-tagging by about 10%. The EM calorimeter is expected to provide excellent energy resolution,

$$\frac{\sigma}{E(GeV)} = \frac{10\%}{\sqrt{E}(GeV)} \oplus 0.7\%$$

Hadronic Calorimeters

The hadronic calorimeters cover the pseudorapidity range $|\eta| < 4.9$ using three different techniques because of the wide spectrum of physics requirements and differing radiation environments. The hadronic calorimetry in the region $|\eta| < 1.7$ (Tile Calorimeter) uses iron absorbers with scintillator plates. This technique offers good performance combined with simple, low-cost construction. At larger rapidity (Forward Calorimeters and End Cap Calorimeters), where higher radiation resistance is required, the hadronic calorimetry is based on the use of liquid argon.

The hadronic calorimeters are required to identify and measure the energy and direction of jets as well as the total E_T^{miss}. The required jet-energy resolution depends on the pseudorapidity region and is given by:

$$\frac{\sigma}{E(GeV)} = \frac{50\%}{\sqrt{E}(GeV)} \oplus 3\%$$

for $|\eta| < 3.2$ and

$$\frac{\sigma}{E(GeV)} = \frac{100\%}{\sqrt{E}(GeV)} \oplus 10\%$$

for $3.1 < |\eta| < 4.9$

Through their ability to measure quantities such as leakage and isolation, the hadronic calorimeters are well suited to complement the EM calorimeters in electron and photon identification. Because of their total thickness in terms of interaction length (11 λ), the hadronic calorimeters are capable of containing hadronic showers and minimizing punch-throughs into the muon system.

2.6 Muon System

The Muon Spectrometer forms the outer part of the detector and it is, in terms of volume, the largest component of the detector. It is designed to detect charged particles exiting the barrel and end-cap calorimeters and to measure their momentum in the pseudorapidity range $|\eta| < 2.7$. The accurate determination of the momenta of muons allows the precise reconstruction of the short-lived particles that decay into muons (particles cointaining b or c quarks). Since many of the physics processes of interest involve the production of muons, therefore, the identification of muons provide also an important signature for the event selection (trigger) of the experiment. In fact the Muon Spectrometer is also designed to trigger on these particles in the region $|\eta| <$2.4.

The conceptual layout of the Muon Spectrometer is shown in figure 2.9: the different technologies employed are indicated. In order to have an accurate measurement of the momentum, independently from the inner detector, the design of the muon spectrometer uses four different detector technologies including two types of trigger chambers and two types of high precision tracking chambers. The muon chambers form three concentric cylindrical layers (each called *station*) at radii around 5, 7.5 and 10 m in the barrel region and cover a pseudorapidity range of $|\eta| < 1.0$. In the forward region ($1.0 < |\eta| < 2.7$), the chambers are arranged in four vertical disks concentric and perpendicular to the beam axis at distances of 7.4, 10.8, 14 and 21.5 m from the interaction point (see figure 2.10).

The precision measurements of the muon momentum in the barrel region are based on the sagitta of three stations in the magnetic field, where the sagitta is defined as the

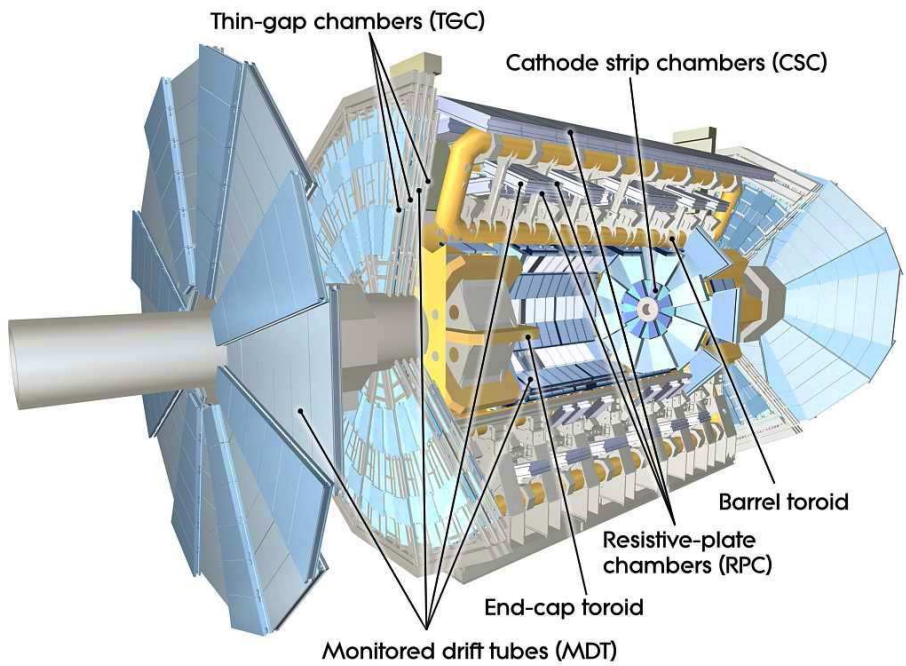

Figure 2.9: 3D view of the muon spectrometer showing areas covered by the four different chamber technologies.

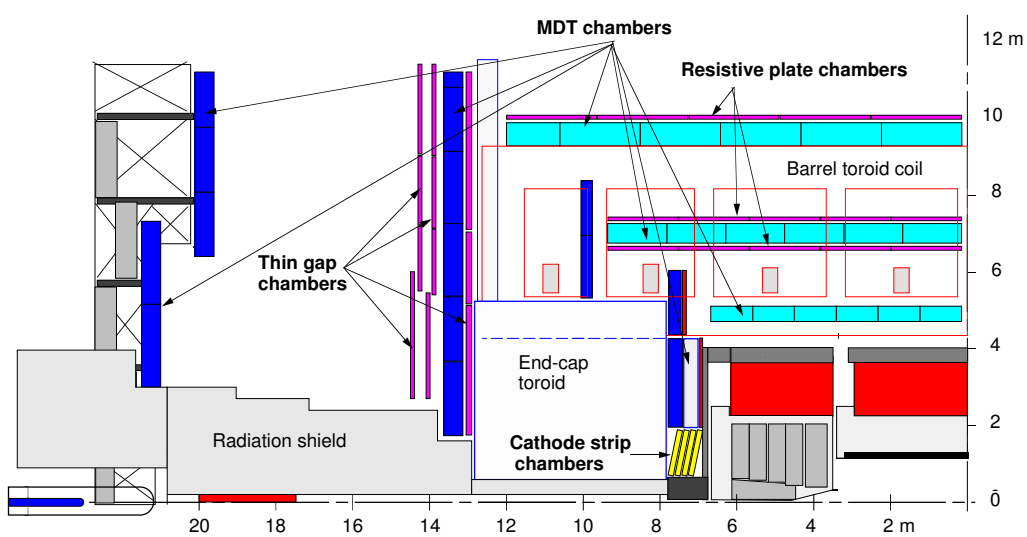

Figure 2.10: R-Z view of one quadrant of the muon spectrometer. High energy muons will typically traverse at least three stations.

distance from the point measured in the middle station to the straight line connecting the points in the inner and outer stations.
In the end-caps, the situation is different; the magnetic field is present only between the inner and the middle stations, therefore the momentum is determined with a point-angle measurement: a point in the inner station and an angle in the combined middle-outer stations.

The driving performance goal is a stand-alone transverse momentum resolution of approximately 10% for 1 TeV tracks, which translates into a sagitta of about 500 μm, to be measured with a resolution of $\leq$ 50 μm. Muon transverse momenta down to a few GeV ($\sim$ 3 GeV, due to energy loss in the calorimeters) may be measured by the spectrometer alone. Even at the high end of the accessible range ($\sim$ 3 TeV), the stand-alone measurements still provide adequate momentum resolution and excellent charge identification (see fig. 2.13).

2.6.1 Muon Chamber Types

As discussed in the previous section, the chambers are positioned at three stations along the muon trajectory.
The *high precision tracking system* comprises the Monitored Drift Tubes (MDT) and the Cathode Strip Chambers (CSC). The precision chambers are required to measure spatial coordinates in two dimensions and to provide good mass resolution as well as a good transverse momentum resolution in both the low and high P_T regions. The performance benchmark, given the magnetic field and the size of the spectrometer, requires a position resolution of 50 μm. The spectrometer is designed such that particles from the interaction vertex traverse always three stations of chambers.
The *muon trigger system* comprises the Resistive Plate Chambers (RPC) in the barrel region and Thin Gap Chambers (TGC) in the forward region. These chambers determine the global reference time (bunch crossing identification) and the muon track coordinate in both directions. The trigger system is designed to reduce the LHC interaction rate from about 1 GHz to the foreseen storage rate of about 100 Hz. The trigger chambers must be able to trigger with a well defined P_T cut-off and to measure the coordinates in the direction orthogonal (ϕ coordinate) by the precision chambers with a resolution of 5-10 mm.

Precision chambers

Monitored Drift Tube (MDT) A monitored drift tube (MDT) chamber consists of three or four layers (a *multilayer*) of 30 mm diameter cylindrical drift tubes each outfitted with

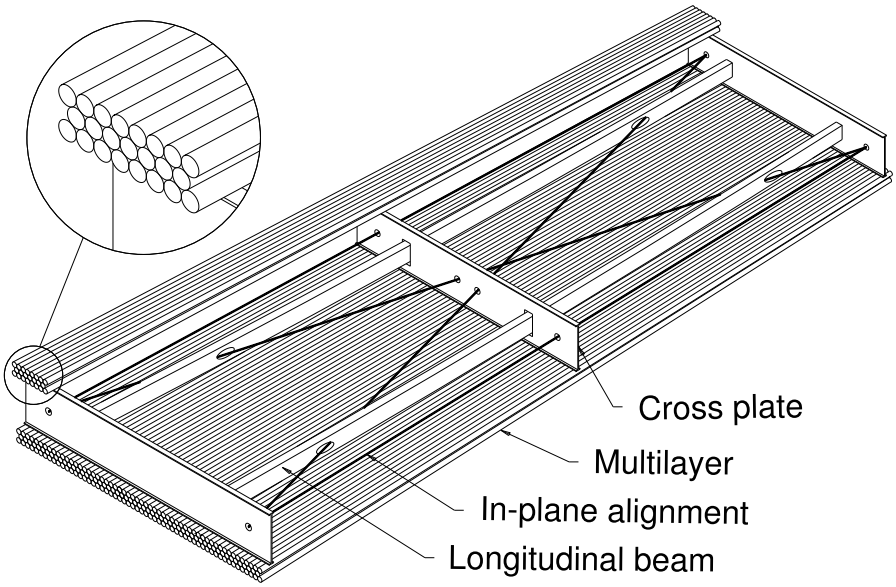

Figure 2.11: Schematic view of an MDT module with detail of the tube arrangement in the inlet.

a central W-Re wire of 50 μm (see figure 2.11) on each side of a supporting frame. The MDT chambers perform the precision coordinate measurement in the bending direction of the air-core toroidal magnet and therefore provide the muon momentum measurement. The four layers chambers are located in the innermost muon detector stations where the background hit rates are the highest. An additional drift-tube layer makes the pattern recognition in this region more reliable.

The MDTs are operated with a gas mixture of 93% Argon and 7% CO_2 at a pressure of 3 atm. The tube lengths vary from 70 to 630 cm as a function of chamber position around the detector. The chambers are positioned orthogonal to the $r-z$ plane (wires parallel to magnetic field lines) in both the barrel and end-cap regions, thus providing a very precise measurement of of the axial coordinate (z) in the barrel and the radial coordinate (r) in the transition and end-cap regions. The MDTs provide a maximum drift time of about 700 ns and a single tube (wire) resolution of 80 μm, while the resolution in the bending direction is 40 μm. The momentum resolution is shown in figure 2.13.
The precision measurement of muons tracks are done everywhere using MDTs except in the innermost ring of the inner station of the end-cap, where particle fluxes are highest. In this region the CSCs are used.

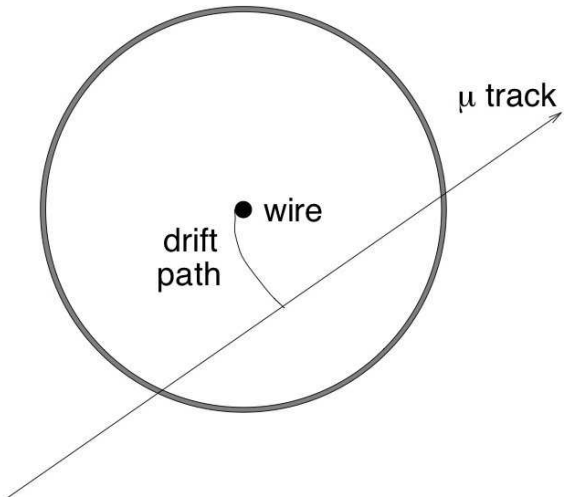

Figure 2.12: Drift path of an ionized particle in a magnetic field.

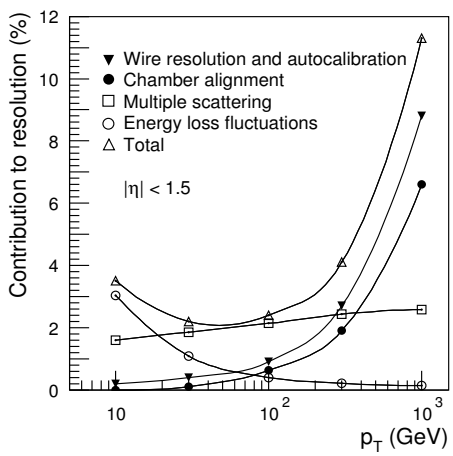

Figure 2.13: $\Delta p_T/p_T$ as a function of p_T for muons reconstructed in the barrel region ($\eta \leq 1.5$).

Cathode Strip Chambers (CSC) The CSC are multiwire proportional chambers with both cathodes segmented, one with the strips perpendicular to the wires providing the precision coordinate and the other parallel to the wires providing the transverse coordinate. The position of the track is obtained by interpolation between the charges induced

on neighbouring cathode strips. The CSC wire signals are not read out.

Each CSC chamber consists of 4 layers. The CSC are operated with a non flammable gas mixture of 80% Argon and 20% CO_2 and provide a maximum drift time of 30 ns. An r.m.s time resolution of 3.6 ns results in a reliable tagging of the beam-crossing..
The precision coordinate is obtained by measuring the charge induced on the cathode strips by the avalanche formed on the anode wire. The cathode strips are oriented orthogonal to the anode wire and are segmented, to obtain a position measurement with a resolution of $60\mu m$ per CSC plane. In the non-bending direction the cathode segmentation is coarser leading to a resolution of 5 mm.
The parallel strips provide the ϕ coordinate. Installed at a distance of seven meters from the interaction point and $2.0 < |\eta| < 2.7$, these muon detectors are built to survive the high radiation environment produced by the colliding high-energy protons.

Trigger chambers

Resistive Plate Chambers (RPC) The trigger system in the barrel consists of three concentric cylindrical layers around the beam axis, referred to as the three trigger stations.

The RPC is a gaseous parallel electrode-plate (i.e. no wire) detector. Each of the two rectangular detector layers are read out by two orthogonal series of pick-up strips: the η strips are parallel to the MDT wires and provide the bending view of the trigger detector, the ϕ strips orthogonal to the MDT wires provide the second coordinate measurement which is also required for the offline pattern recognition. The use of the two perpendicular orientations allows the measurements of the η and ϕ coordinates. The RPC combine an adequate spatial resolution of 1 cm with an excellent time resolution of 1 ns.
The number of strips (average strip pitch is 3 cm) per chamber is variable: 32, 24, 16 in η and from 64 to 160 in ϕ. When a particle goes through an RPC chamber, the primary ionization electrons are multiplied into avalanches by a high electric field of typically 4.9 kV/mm. The signal is read out via a capacitive coupling of strips on both sides of the chamber.

Thin Gap Chambers (TGC) Thin Gap Chambers (TGC) provide two functions in the end-cap muon spectrometer: the muon trigger capability and the determination of the second, azimuthal coordinate to complement the measurement of the MDT in the bending direction.

They are very thin multi-wire proportional chambers The peculiarity of TGC compared to regular MWPC is that cathode-anode spacing is smaller than the anode-anode (wire-wire) spacing. This characteristic allows a shorter drift time and an excellent response in time of less than 20 ns, which meets the requirement for the identification of bunch crossings at 40 MHz.

The TGC are filled with a highly quenching gas mixture of 55%$CO_2$and 45%n-pentane C_5H_{12}. This allows TGC to work in a saturation operation mode with a time resolution of 5 ns and with good performances in a high particle flux.

2.7 The Trigger and Data Acquisition System

As already discussed, LHC should work at a design luminosity of $10^{34} cm^{-2} s^{-1}$ in order to allow the studies of rare events. This condition will lead to over 23 interactions per bunch crossing. Thus, each second close to 10^9 interactions occur. Most of these interactions are minimum bias events that have a limited interest corresponding to an amount of data of $\approx 4 \times 10^4$ Gbyte s^{-1}. Therefore it is necessary to select interesting data in order to register only the interesting portion of the total amount of data coming from the collision. To satisfy this request, a trigger system and a data aquisition system (DAQ) (see figure 2.14) have been designed with the challenging role of selecting bunch crossings containing interesting events by reducing the data rate from 40 MHz (collision rate) to 100-200 Hz.

The trigger and Data Acquisition system (TDAQ) is organized in three trigger-levels (LVL-1, LVL-2 and LVL-3 or event filter) as shown in figure 2.14. Decisions made by a given trigger level are used as input at the subsequent level.

LVL1 The first level trigger (LVL1) is designed to operate at a maximum pass rate of 75 kHz. The LVL1 decision is based on information with a coarse granularity of two sub-detector systems: the muon trigger chambers and the calorimeters. It searches for signatures of high-P_T muons in the muon system trigger chambers (RPC and TGC), and for signatures of jets, electrons/photons clusters, τ-leptons decays, and large missing transverse energy (E_T^{miss}) in the calorimeter. It also identifies Regions-of-interest (RoI) of the detector associated with those signatures and informs the front-end electronics.

LVL2 The second level trigger (LVL2) reduces further the event rate to a maximum of 3.5 kHz by using detailed information from the RoI.
For a LVL1 muon trigger, the LVL2 will use the information from the precision MDT chambers to improve the muon momentum estimate, which allows a tighter cut on this quantity. For a LVL1 calorimeter trigger, the LVL2 has access to the full detector granularity, and has in addition the possibility to require a match with a track reconstructed in the inner detector. The LVL2 has an event dependent latency, which varies from 1 ms for simple events to about 10 ms for complicated events. For events accepted by the LVL2, the data fragments stored in the RoI are collected

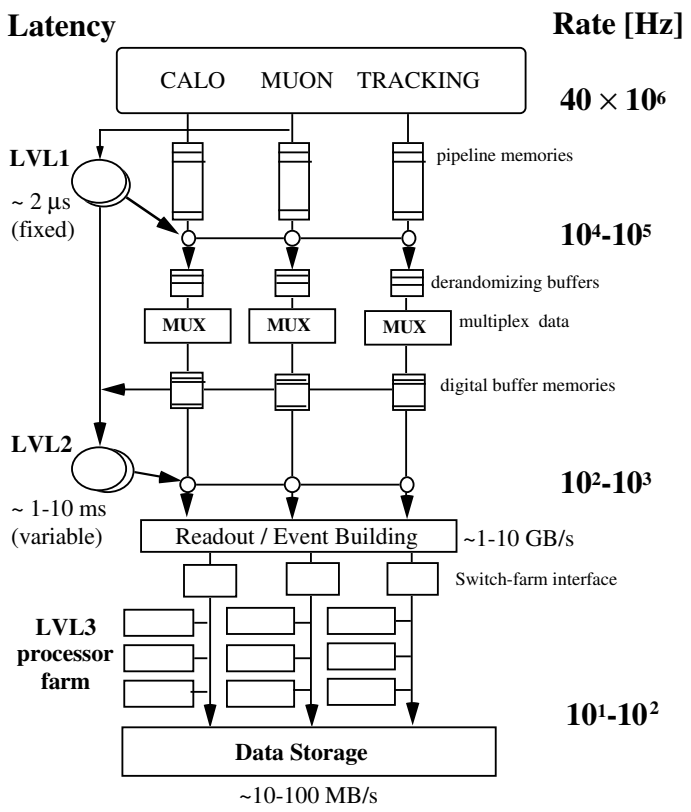

Figure 2.14: The trigger levels and DAQ.

by the so-called Event Builder and written into the Full Event Buffers. The event builder system assembles and ships to the LVL-3 trigger the full event data of all events accepted by the LVL-2. The average event processing time at this level is about 40 ms per event.

LVL3 The third trigger stage is called LVL3 and uses up to date detector information including magnetic field maps, calibration results and full granularity and precision of the calorimeter, muon system and ID to further reduce the event rate. The LVL3 can use complex offline algorithms like track reconstruction, vertex finding, etc., because it has access to the complete event. The stored data is reconstructed to yield quantities like tracks, energy clusters, jets, missing transverse energy, secondary decay vertices, etc. These quantities are subject to various physics selection criteria in offline analyses too, for example to maximise the discovery potential for the Higgs particle. For the maximum trigger rate of 100-200 Hz the average event

processing time will be of order four seconds.

All the data flow between various front-end electronics and different trigger levels is handled by the Data Acquisition (DAQ) system. It stores the information from all detectors in pipelined memories while decision is being made (latency) by the trigger system. The DAQ also provides configuration, control and monitoring of the detector during data-taking.

The different input and output data flows for the three levels trigger are summarized in table 2.1.

Trigger level	**Maximum flow of input data**	**Maximum flow of output data**
LVL1	40 MHz	75 kHz
LVL2	75 kHz	3.5 kHz
LVL3	3.5 kHz	100-200 Hz

Table 2.1: Input and Output data flows from the three levels of the TDAQ.

Chapter 3

Software tools

In order to provide realistic predictions for the experimental capabilities of detecting physical processes, the simulation of the detector response interfaced to a Monte Carlo generator is crucial.
The whole software is implemented in a global framework written in C++ programming language, called ATHENA [21]. This framework is a working environment under which the user can apply his own analysis algorithm to select the signal and the backgrounds he is interested in. The ATLAS software framework is continously updated to allow developers to insert new code and amend bugs. Periodically the whole software is 'released' and given a Release Number. This is a group of three integers separated by dots, where the first number is the major release, the second indicates developer release, and the third indicates minor changes. A summary of all releases and their properties can be found in [22].

A detailed description of the performances of the detector and its response to all the interesting physics processes before the start up of LHC requires the use of three separate software modules that can be run either separately or in sequence under the ATHENA infrastructure:

- event generation ;
- detector simulation;
- digitization.

The results of this thesis have been obtained using the ATHENA framework. Different releases have been used. They will be specified for each study decribed in the following chapters.

Event generation The first step of the event generation phase is implemented within ATHENA using physics event generators.
Generally the generators simulate the collisions of various particle species (protons, electrons, ...) at a given center of mass energy (see section 3.1). Generators also simulate particles emerging from the interaction region. A physics event generator produces lists of particles. The input to the generator is usually in the form of beam energy, tables of decay probabilities, specific particle reactions, and specific final state particles. The output is a list of events which serve as input to the simulation. Each particle is parameterized by particle-type, initial vertex, initial and final four-momentum vectors. Event generators are frequently updated to keep up with the latest theoretical insights. In the case of LHC phenomenology, calculations must include QCD uncertainties due to the parton distribution functions and the hadronisation.

Detector simulation Detector simulation is the simulated response of the detector to particles generated in the interactions and their decay products.
There is not an unique way of implementing the detector simulation. The accuracy by which the detector performance need to be simulated strongly depends on the purpose of the analysis.
Two types of detector simulation exist in the Atlas software framework: Geant4 full detector simulation [29] (*full simulation* see section 3.2) and $Atlfast$ fast detector simulation [38] (*fast simulation* see section 3.3).
The former is based on complete detector material description including the best possible details. The latter does not consider detector materials in details; it only smears the kinematics of the MC particles according to the expected detector performance.
Full simulation is desiderable to study detector performances and systematic uncertainties originating from the intrinsically limited detector resolution, but it is an intensive computing process that can take up to $\sim$ 30 minutes per event, using a large amount of memory, CPU and disk space.
Fast simulation, on the other hand, takes a small fraction of a second per event. For some feasibility studies that require a large amount of statistics, a simple parameterisation of the smearing of the particle observable parameters can be sufficient. This means that for this kind of studies also the fast simulation can be used.
To make final conclusions from the simulation studies, often one needs to combine the results coming from full and fast simulations.

Digitization The digitization step is the final phase, where the deposited energies in the various detector elements are recorded, collected and reprocessed in order to simulate the electronic output from the detector. The digitization stage includes simulation of physics

effects specific to each type of detector and of the front-end electronics response and of noise. The output of the digitization is written into Raw Data Objects (RDO) to be used by the reconstruction programs. These reconstruction programs are the same that will be used once the experiment will start to take data.

Figure 3.1 shows how the simulated raw data, Raw Data Object (RDO), is produced from the generated Monte Carlo (MC or Truth) events. In this scheme also the data flow produced by the experiment is presented. ATLAS data will be recorded as a sequence of bytes that must be converted by the ByteStream ConversionSvc into RDO in order to be used by the reconstruction programs.

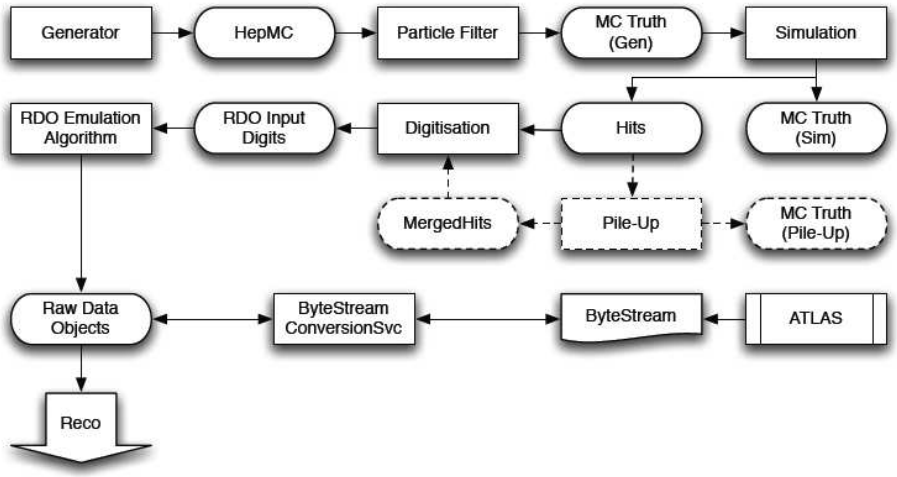

Figure 3.1: Schematic diagram showing the flow of MC data through simulation and digitisation process.

Reconstruction In order to convert this raw information to more fundamental physics objects the recorded events are processed through a set of computer algorithms that constitue the reconstruction process. This process will be discussed in more detail in section 3.2.2, neverthless in summary here is a schematical division of such a process into three main stages:

- data from each subdetector are reconstructed in stand-alone mode;
- informations from all sub detectors are combined to identify the observable objects such as tracks, muons, jets etc.;

- informations from different observable objects are combined into reconstruction algorithms for selecting the signal and rejecting backgrounds.

3.1 Monte Carlo Events Generators

Events produced by Monte Carlo (MC) generators are essential tools of physics analysis. As already discussed, to make a realistic estimation of feasibility for future analysis, to compare data with theoretical predictions, or to understand the detector performance in detail, the detector response to MC events need to be simulated.
There are many Monte Carlo generators in particle physics, the most widely used are *PYTHIA* [23], *HERWIG* [25], *ALPGEN* [26], *SHERPA* [24] and *MC@NLO* [27], which are general purpose Monte Carlo. They have been tested in many particle physics experiments and are continously updated to include new process and the most recent calculations.
Each Monte Carlo generator is interfaced to a library called LHAPDF [56] containing informations about different parton distribution functions(PDF) sets. This interface provides the possibility to choose among different PDF sets in order to generate data samples. A more detailed description on PDF and kinematic range of validity will be discussed in section 3.1.2.

In this analysis Monte Carlo event generators are used in a variety of ways, from finding characteristic spectra for variables associated with Z boson and b quarks or b-jet to finding predictions for the cross section of signal and background processes. *PYTHIA* and *SHERPA* event generators interfaced to the ATHENA framework have been used.

3.1.1 The QCD model

A general purpose Monte Carlo generator should contain a simulation of several physics aspects. After the two beam particles come in towards each other, we can try to follow the evolution of an event in timing order arranging it as follows:

- Initial State Radiation:
  One shower initiator parton from each beam starts off a sequence of branchings , such as $q \to qg$, which build up an initial state shower according to QCD calculations. The quarks can also radiate photons according to QED.

- Hard Process:
  One incoming parton of the two showers enters the hard process. The hard process

may produce a set of short lived resonances, like the Z gauge boson, whose decay to partons has to be considered in close association with the hard process itself.

- Final State Radiation:
  The outgoing partons generated in the final state of the Hard Process may branch, just like the incoming did, to build up final state showers.

- Hadronisation:
  The QCD confinement mechanism ensures that the outgoing quarks and gluons are not observable. This mechanism forces all coloured particles to bind together in order to form colour neutral hadrons, which can be experimentally detected.

- Underlying Event:
  Besides the hard process considered above, further interactions may occur between the other partons of the two incoming hadrons. Tipically these are soft interactions generating low p_T particles. In addition, in high-luminosity colliders, it is possible to have several collisions between beam particles in one and the same beam crossing, i.e. pile-up events, which further act to build up the general particle production activity that is to be observed by detectors.

- Particle decays:
  Many of the produced hadrons are unstable and decay further.

A sketch of these steps is the one in figure 3.2.

In the following sections I will go through these aspects not in the same order as given above, but rather in the order in which they appear in the program execution, i. e. starting with the hard process.

Hard Process

The Hard Process yields the physical signal: two partons from the two colliding hadrons interact to produce the final state partons.
The inclusive cross sections ($\sigma^h_{a,b}$) for hard production processes are calculable in terms of the so called QCD-improved parton model formula 1.16.
For a more detailed description of the Hard Process I refer to section 1.3.2.

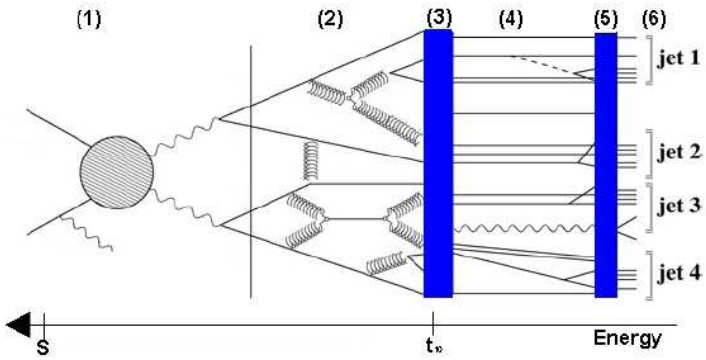

Figure 3.2: Schematic drawing of an interaction involving quarks. First the hard-scattering occurs which could include some initial and final state radiation (1). In this case a decay of two photons (wavy lines) to two pairs of quarks (straight lines) is shown. Then the Final State Radiation (FSR) process occurs (2): many gluons (spring like lines) can be emitted which can in turn decay to quark-antiquark pairs. This process occurs until the energy scale of each parton is close to t_0. The non-perturbative hadronisation process then occurs (3) which turns the partons into hadrons. The latter can decay into a series of final state particles (4) which are measured by the detector (5). Finally objects such as jets are reconstructed from what is observed in the detector (6). In this case four jets would be observed.

Initial and Final State Radiation

The *Initial* and *Final State QCD Radiation* (ISR and FSR) process, also called fragmentation, are the processes whereby the partons create many more partons. This process is illustrated in the part (1) and (2) of figure 3.2. A quark can emit a gluon,a gluon can emit another gluon or convert into a quark-antiquark pair. This process continues until the virtual masses squared of the partons are of the order of the infrared cut-off scale, t_0, taken to be of the order of 1 GeV^2 .
Fragmentation models focus on the calculation of approximate results of parton showering where the enhanced terms, such as soft or collinear parton emission from the primary parton, are taken into account for all orders of the perturbative expansion in terms dependent on α_s. The parton shower models represent an approximate perturbative treatment of QCD dynamics at scales larger than t_0. The implementation of fragmentation models in Monte Carlo simulations mostly use Sudakov form factors. These form factors determine the probability of evolving from the initial scale t to the shower cut-off scale t_0. Each parton species has its own form factor. For more details see [8, 9].

Summarizing at high energy scale the fragmentation of $q\overline{q}$ in high energy partons (gluons and $q\overline{q}$ couple) is described by *perturbative QCD*. At small energy scale the soft gluon radiation (or radiation from gluon of low p_T) must be described through fenomenological models (*non perturbative QCD*).

Underlying Event

The presence of a significant amount of soft interactions between the colliding hadrons (beam-beam remnant interactions), possible multiple parton interactions and gluon radiation from the initial partons before the hard interaction (initial state radiation) complicate things even further. These additional processes are collectively known as the *underlying event*. From an experimental point of view, in a hadron-hadron interaction with jets in the final state, the underlying event is all the activity accompanying the two hard scattered outgoing jets. The underlying event, along with the finite detector resolution, leads to the fact that it is not possible to unambiguously determine, even in Monte Carlo simulation, which hadrons came from which initial parton, i.e. which hadrons belong to which parton jet. It is impossible to separate these two components due to the lack of knowledge in modeling the underlying jet structure.
The typical approach to modelize the UE is to rely on particle and energy densities in $\eta - \phi$ regions that are well separated with respect to the high p_T objects (for example jets). In shower Monte Carlo model, the underlying event is a component of the process simulation that acts at the end of the showering and before the hadronisation, in order to complete the process description taking into account soft components (hadronic remnants and multiple interaction).
Huge progress in the phenomenological study of the underlying event in jet events has been achieved by the CDF experiment at the Tevatron [14, 15], using the multiplicity and transverse momentum spectra of charged tracks in different regions of the azimuth-pseudorapidity space, defined with respect to the direction of the leading jet. Regions that receive energy flow contributions mostly by the underlying event have been identified.

Hadronisation

After the fragmentation, the low-momentum-transfer, long-distance regime is entered, in which non-perturbative effects become important. The most important of these effects is hadronisation which converts the partons into the observed hadrons (part (3) of figure 3.2). Most models of these phenomena, when implemented in Monte Carlo simulations, assume that the two processes, fragmentation and hadronisation, occur in sequence and can thus be treated independently [8].
In principle, the shower cut-off, t_0, is an arbitrary parameter, uncorrelated with the hadro-

nisation process but when t_0 is increased, the parton shower is terminated earlier and there are fewer partons to hadronise. Thus the hadronisation models should have a parameter t_0 whose effect cancels out when the parton shower model and the hadronisation model are combined. In practice t_0 is tuned such that the final number of hadrons agrees with experimental observation.

Particle decays

Not all the particles produced are stable, some of them have a short lifetime. The particles with a life time shorter than a value fixed in the Monte Carlo generator (default is typically 1.0×10^{-8} s) are forced to decay. All other particles are considered stable by the MC generator. Unstable particles with a longer lifetime are forced to decay in the detector simulation as it will be discussed in section 3.2.1.

3.1.2 Parton Density Function (PDF)

The calculation of the production cross sections at hadron colliders for both interesting physics processes and their backgrounds relies upon a knowledge of the distribution of the momentum fraction x of the partons (quarks and gluons). If the understanding of the perturbative corrections to the hard scattering cross section of eq. 1.16 is in good shape, the uncertainty on the PDFs can limit the accuracy of the theoretical predictions.
In order to evaluate PDF uncertainties on some observables distributions or on cross section prediction, is it possible to generate different data sample using different PDF sets. Here I will briefly discuss how PDF are determined and which sets are the most common used nowadays.

Perturbative QCD does not provide the PDF's analytic dependence as a funcion of x (which has a non perturbative origin) but through the DGLAP equations [6] it provides the evolution from a fixed scale Q_0^2 to a given Q^2.
The common way to obtain PDF's as a function of x and Q^2 is to parametrize the quark and gluon density functions in order to perform a global fit of experimental data.
All global analyses use a generic form for the parametrization of both the quark and gluon distributions at some reference value Q_0:

$$F(x, Q_0) = A_0 x^{A_1} (1-x)^{A_2} P(x; A_3, \ldots) \tag{3.1}$$

The reference value Q_0 is usually chosen in the range $1-2$ GeV.
The first two factors, in general, are not sufficient to describe either quark or gluon distributions. The term $P(x; A_3, \ldots)$ is a suitably chosen smooth function, depending on one

or more parameters, that adds more flexibility to the PDF parametrization. In general, both the number of free parameters and the functional form can have an influence on the global fit. No unanimous agreement is anyway found on such parameterisations and on the number of free parameters.
The current PDF sets are derived from global fits to the available data, which include deep inelastic scattering measurements at HERA and at fixed target experiments, Drell Yan measurements and the Tevatron data on the inclusive jets production and the W charge asymmetry. Many different groups (CTEQ [48], MRST [49, 50], ZEUS [51], H1 [57]) work to provide PDF sets and an estimation of the corresponding errors. The differences among the results are due to the different experimental inputs and treatment of the theoretical and experimental uncertainties entering the global fit. The theoretical uncertainties are related both to the parameterisation at the Q_0^2 scale and to the perturbative part (missing orders and approximations). The experimental uncertainties include statistical and systematic errors on the input data and the correlations among them. The central values of the PDF's parameters correspond to the best fit; they are associated with uncertainties which are conventionally computed along the eigenvectors of the covariance matrix. In this way the error band for a given PDF set is computed and the uncertainty is then propagated to the variable under study. For a more exhaustive treatment see [9].
The newest PDFs, in most cases, provide the most accurate description of the world data and should be utilized in preference to older PDF sets.

Hard process and Parton Density Function at LHC

I showed in section 1.3.2 that the collision between two hadrons (two protons at the LHC) can be described as an interaction between two partons that constitute the hadrons (see figure 1.8). From the kinematic plane Q^2 vs x in the left part of figure 3.3 it is visible that at the LHC the very low-x region will be accessible at the electroweak scale and the very high one at the TeV scale. At LEADING ORDER (LO) Z production occurs through the $q\overline{q} \rightarrow Z$ process ($Q \sim$ 100 GeV). The momentum fraction is given for each parton by $x_{1,2} = \frac{M_Z}{\sqrt{s}}\, e^{\pm y}$, being M_Z the center of mass energy of the hard partonic process and $\sqrt{s}$ the center of mass energy of the reaction (14 TeV).
From the kinematic plane in figure 3.3 it can be seen that at central rapidities the partons have small x, $x_1 \sim x_2 \sim$ 0.005; moving away from the central region they take higher or lower x, always remaining within the range $10^{-4} < x < 0.1$ for measurable values of rapidity $|y| < 2.5$. For $Q \sim$ 100 GeV the gluon distribution is dominant at x values of less than 0.1 with the valence quark distributions dominant at higher x. The scattering happens between sea quarks; at such high scales $Q^2 = M^2 \sim$10,000 GeV^2 the gluon dominates (see figure 3.3, right) the sea quarks are mainly generated via gluon splitting $g \rightarrow q\overline{q}$.

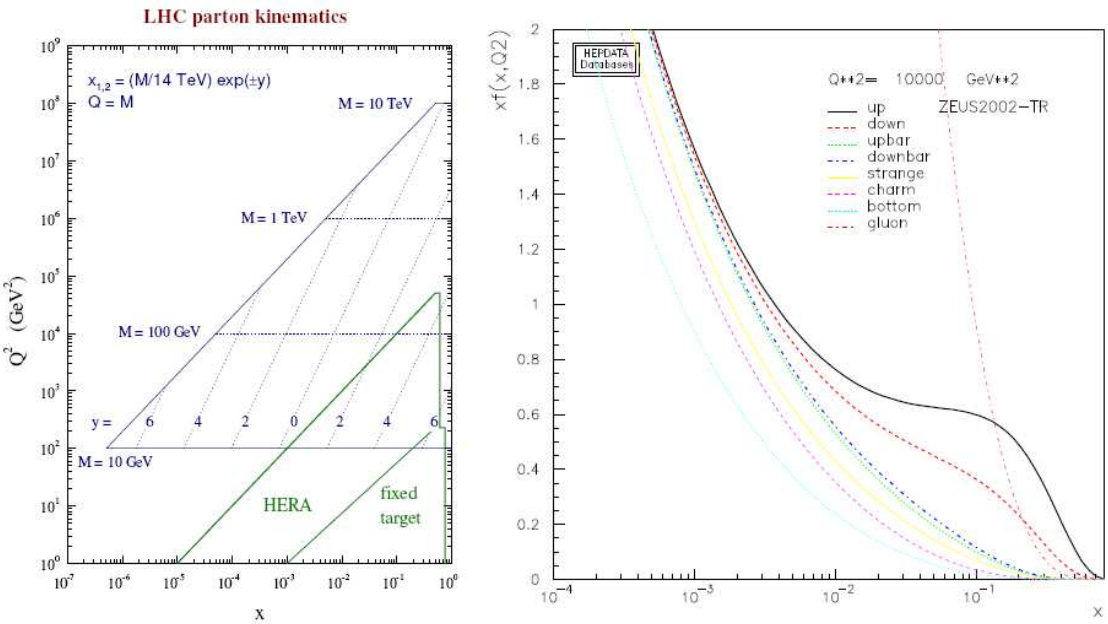

Figure 3.3: Left) The $Q^2 - x$ kinematic plane for the LHC and previous experiments. Right) PDF's distributions at $Q^2 =$ 10,000 GeV^2 obtained from CTEQ6.5M set.

One of the major influences of the HERA data has been to steepen the gluon distribution at low x.

3.1.3 Generator parameters

Many parameters are dependent on experimental observation measured rather than analytical expression and there are uncertainties on those variables. QCD processes are generally sensitive to arbitrary choice of scales; sub-processes that accompany hard scattering usually involve non-perturbative QCD processes that require parameterised modelling (see discussion in section 3.1.2). In this section I summarise these issues together with the values selected for each generator used to produce signal and background events. The following parameters were used common to all generators:

- $\alpha_{em} = \frac{1}{137.04}$;
- G_F = 1.16639 $\dot{1}0^{-5} GeV^{-2}$;
- M_Z = 91.19 GeV, Γ_{MZ} = 2.495 GeV;

- M_W = 80.42 GeV, Γ_{MW} = 2.124 GeV;
- $\sin^2\theta_W$ = 0.232;
- M_t = 175 GeV.

To generate samples used in the analysis performed with the fully simulated sample, the latest parton distribution set for leading-order generators from the CTEQ collaboration, CTEQ6L [48] have been used. This includes latest data from experiments at HERA [51] and Tevatron for an improved parameterisation.

Samples used for the analysis with the fast simulation have been generated using different PDF sets in order to compare distributions, as it will be discussed in more detail in chapter 4.

All the samples used for the analysis (both for full and fast simulation studies) do not include events with more than one proton proton collision per bunch crossing (pile up events). This is reasonable for a luminosity of less than 10^{33} cm^{-2} s^{-1} sufficient for a first measurement of the process studied in this thesis: pp $\rightarrow$ Z($\mu\mu$) + b jet + X (where X states for everything in the final state produced in association to the leading process).

3.2 The Full detector simulation and reconstruction

A detector simulation is crucial for understanding detector acceptances and in many cases for modeling backgrounds. The ATLAS full simulation parameterizes the detector geometry and material using Geant4 [29]. The kinematics of physical processes are reproduced to a certain order of calculation by a Monte Carlo generator program (see section 3.1). As already described the generator gives a set of four-vectors that are smeared by the detector simulation. The simulation produces data banks from each subdetector identical to those from collision data, and the simulated data are analysed using the same code as the collision data. The digitised (real or simulated) event data are read in by the *Reconstruction* software which identifies particles and measures their energies and momenta.

3.2.1 GEANT4 Simulation

Geant4 [29] is a common tool used in high energy physics to simulate the particle propagation through the detector and particle interaction with active and passive materials. It is based on an object oriented architecture, implemented using C++. Geant4 takes into account a large number of physics processes of interaction between the particles and the detector. Firstly it displaces the primary vertex position to take into account the finite size

of the beam overlap region,then it simulates the energy loss due to dead material inside the detector and saves into stored objects the energy deposit in the active detector elements.
The simulation requires a precise geometrical description of the detector components including the materials used in the manufacture, as well as the magnetic field maps. Detector geometry descriptions are stored in a database and retrieved by the simulation jobs. Geant4 creates a simulated detector in memory based on the description and then simulates the interaction of input particles with the detector.
Features required for the detector simulation were identified and results have been validated with test-beam data [30], which provided tuning of the relevant parameters. Validation with test-beam results shows that in almost all cases, comparison with the test-beam data are in very good agreement, normally at the level of 1% or better [31].
The precise description of the detector used in simulation and reconstruction is an important issue affecting the quality of calibration. Although implementation of the detailed detector effects and production efforts has been successful, full detector simulation is one of the most resource consuming processes in producing MC based data and significant optimisation is desirable.

3.2.2 Offline reconstruction

The events recorded after the detector simulation program are kept in a raw format (RDO) which contains the digitized information from detector sub-systems like the hits in the tracking and muon systems and the digitized counts in the calorimeter cells. In order to convert this raw information to more fundamental physics objects like electrons, and provide useful kinematic as well as quality information, the recorded events are processed through a set of computer algorithms called the offline event reconstruction. In order to study the reconstruction performances, the same algorithms which are under development for the real data are applied on simulated events.
The analysis shown in this thesis was realized using reconstruction done within Athena releases 12.0.4 and 12.0.6. A description of releases and changes that can account moving from one release into another, can be found in [22].
In the next few sections, I will give more detailed accounts on how the offline reconstruction is performed and I will refere to observables defined in section 2.2.1 such as transverse momentum, rapidity and angular distance.

Inner detector tracks

Different stategies have been developed to reconstruct tracks in the inner detector, here I will discussed the most common used. Track reconstruction can be logically sub-divided

into three stages:

1. A pre-processing stage, in which the raw data from the pixel and SCT detectors are converted into clusters and the TRT raw timing information is turned into calibrated drift circles. The SCT clusters are transformed into space-points.

2. The default track-finding exploits the high granularity of the pixel and SCT detectors to find prompt tracks originating from the vicinity of the interaction region. First, track seeds are formed from a combination of space-points in the three pixel layers and the first SCT layer. These seeds are then extended throughout the SCT to form track candidates. Next, these candidates are fitted, outlier clusters are removed, ambiguities in the cluster-to-track association are resolved, and fake tracks are rejected. The selected tracks are then extended into the TRT to associate drift-circle information in a road around the extrapolation and to resolve the left-right ambiguities. Finally, the extended tracks are refitted with the full information of all three detectors and the quality of the refitted tracks is compared to the silicon-only track candidates.

3. A post-processing stage, in which a primary-vertex finder is used to reconstruct primary vertices.

This strategy is expected to give very high detection efficiency over the full detector acceptance, $|\eta| < 2.5$.

Calorimeter Tower and Topological Cluster

Calorimeter Towers are built from all calorimeter cells contained in a region of $(\Delta\eta \times \Delta\phi)$ of size equal to (0.1×0.1). Topological Clusters are built according to criteria that identify significant energy deposits in topologically connected cells. In particular, cells with $> 4\sigma$ significance (σ being the standard deviation of fluctuation due to noise) are taken as seeds and neighbouring cells with $> 2\sigma$ significance are clustered to form energy blobs with a three-dimensional topology.

Jets

Jet algorithms are used to group the final state hadrons into jets whose properties are as close as possible to the initial parton carachteristics. We must distinguish between the so called *Truth Jets* and *Reconstructed Jets*. These definitions depend from the input of the algorithm: if the jet clustering algorithm run on ”truth” particles (generated from the Monte Carlo program) inside the detector acceptance, excluding neutrinos and muons,

the jets will be called *Truth Jets*, while if the algorithm run over calorimeter towers or topological Clusters (defined in the previous paragraph) we will refer to *Reconstructed Jets*.

The comparison between the first and the second kind of jets will be a crucial tool in order to disentangle detector and physics effects.

Two main classes of jet algorithms have been used: the *Cone* and k_T [35] algorithms. The first class, the most widely used, looks at the energy deposited in the towers of the calorimeter and define all particles within a physical cone of fixed size to belong to the same jet. The different cone algorithms differ in the method used to find the final cones, in the size of the cones, or in the way of dealing with cones which overlap. This is the class of algorithms which is discussed below.
The second class of algorithms defines jets in terms of towers which are not close to each other from a spatial point of view but are close to each other in k_T. k_T is proportional to the relative transverse momentum between two particles.
Historically, cone algorithms have been used in hadron colliders, due to concerns about speed, especially at the trigger level, and of large systematic effects in busy multi-jet environments. Fast implementations of the k_T algorithm [36], as well as detailed studies at the Tevatron performing precision measurements with the algorithm [37] need detailed comparisons of the k_T algorithm with cone-based ones at the LHC.

The offline reconstruction algorithms take as input any E_T ordered list of calorimeter objects (cells, towers or clusters). The jet reconstruction consists of the following steps:

- Removal of negative energy towers (or clusters) by combining them with adjacent ones. A list of proto-jets is also constructed using a simple pre-clustering algorithm.
- Removal of proto-jets with transverse energy smaller than a given threshold.
- Running of a jet finding algorithm (cone or $\mathrm{k_T}$ algorithm) using seeds position defined to be between proto-jets above a given threshold (default is $E_T > 2\ GeV$).
- Jet calibration.
- Removal of reconstructed jets below a given transverse energy (default is $E_T > 10\ GeV$).

Jets labelling and tagging

Jets originating from the hadronisation of b quarks can be tagged by exploiting the high mass and relatively long lifetime of B hadrons. The average lifetime of the most commonly occurring hadrons containing a b quark such as B^+, B^0, B_S ($\sim$ 1.5 ps), is long

enough to allow to a 10 GeV B meson to cover a distance of the order 1 mm before decay. In general the tracks of charged particles decaying from these hadrons have large impact parameters with respect to the primary vertex, and a reconstructable secondary vertex. Typically, jets originating from the hadronization of b quarks contain 5 - 10 tracks,with about half of them coming directly from the B meson decay. Therefore one can extrapolate the track measurements from the inner detector to identify the existence of a secondary vertex or evaluate impact parameters of the tracks with respect to the primary vertex.
To evaluate the likelihood of a given jet to contain a B hadron, the track significance is calculated for each track by taking the ratio of the distance of closest approach to the primary vertex, d_0, and the error on the measurement σ_{d_0} . Since the resolution in the x-y plane is an order of magnitude finer compared to the resolution in the z direction (tens of microns against hundreds of microns), d_0 is measured in the transverse plane only (in which case it may be denoted as a_0) although one could obtain more information from including the longitudinal impact parameter (denoted as z_0). In fact an important improvement of the performances of the b-tagging algorithm can be expected by combining the *longitudinal significance* with the *transverse* one: this algorithm is called the IP3D b-tagging algorithm. The distribution of track significance for light jets and b-jets are used to construct the likelihood function P_u and P_b and finally, a weight is given to the jet [44, 45]:

$$w_{jet} = \sum_{i \in jet} \ln \left[P_b(\frac{a_0^i}{\sigma_{a_0}^i}, \frac{z_0^i}{\sigma_{z_0}^i}) / (P_u(\frac{a_0^i}{\sigma_{a_0}^i}, \frac{z_0^i}{\sigma_{z_0}^i})) \right] . \tag{3.2}$$

The power of the IP3D b-tagging method can be significantly improved by using additional informations on the presence or absence of a secondary vertex in the jet. The algorithm using secondary vertex is commonly called SV1.

In order to evaluate the goodness of this algorithm, it is possible to define the *b-tagging efficiency*, the *mistag probability* and the c, τ, *light jets rejection*:

- **b-tagging efficiency**: is the probability of a b-jet to be tagged as a b-jet.
- **mistag probability**: is the probability that a given non b-jet is tagged ad a b-jet. This varies as a function of jet p_T and η. It also depends on whether the jet contains c quark or τ lepton.
- **rejection**: is the inverse of the mistag probability.

It has been proved that the use of both method (IP3D+SV1) can increase the rejection of light jets significantly, though it was also shown that the method has strong dependence on the track reconstruction algorithm and validation of its performance may require an extensive study with real data [44].

In this analysis, the b-tagging algorithm used is the one that makes use of the 3D impact parameter and secondary-vertex reconstruction, (IP3D+SV1). The distribution of the weight is shown in figure 3.4 separately for light, c and b-jets.

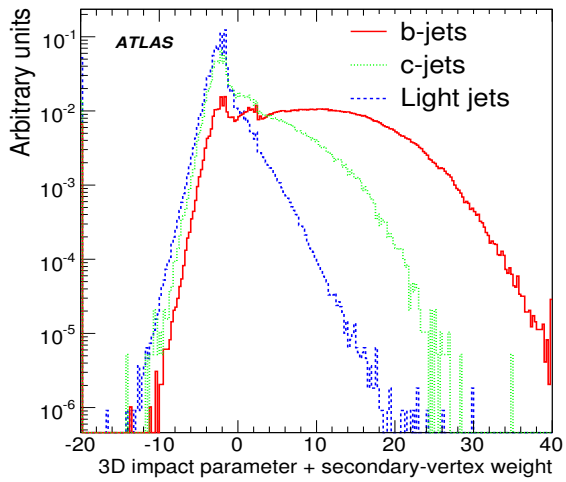

Figure 3.4: Jet *b*-tagging weight distribution for *b*-jets, *c*-jets and light jets corresponding to the IP3D+SV1 tagging algorithm.

Muons

Muon reconstruction can be done using three different strategies:

- Standalone Muons,
- Combined Muons,
- Calo-tagged Muons.

The differences among them depending on which detector is involved in.
The *standalone* reconstruction is the direct approach to reconstruct standalone muons by finding tracks in the muon spectrometer, correcting for the energy loss in the calorimeters and then extrapolating these towards the beam line. The *combined* muons are found by matching standalone muons to nearby inner detector tracks and then combining the measurements from the two systems.

Multiple independent algorithms have been developed to implement each of these strategies and the current baseline reconstruction includes two algorithms for each of the first two strategies. Here I briefly describe the algorithms that are included in this reconstruction. The algorithms are grouped into families such that each family includes one algorithm for each strategy. The output data intended for use in physics analysis includes two collections of muons, one for each family, in each processed event. I refer to the collections (and families) by the names of the corresponding combined algorithms: Staco [34] and Muid [33].

Standalone muons Most of the muons, including those of best quality, are reconstructed by independently finding tracks in the inner detector and muon spectrometer and then combining these tracks. The standalone reconstruction has two major steps: first build track segments in each of the three muon stations and then link the segments to form tracks. The Staco-family algorithm that finds the spectrometer tracks and extrapolates them to the beam line is called Muonboy [34]. On the Muid side, Moore [32] is used to find the tracks and the first stage of Muid performs the inward extrapolation.

The extrapolation must account for multiple scattering and energy loss including that in the calorimeter. Muonboy assigns energy loss based on the material crossed in the calorimeter. Muid additionally makes use of the calorimeter energy measurements if they are significantly larger than the most likely value and the muon appears to be isolated.

The standalone spectrometer tracks can also be used alone to identify muons in regions beyond the coverage of the inner detector ($2.5 < |\eta| < 2.7$), recover muons for which the combination fails and as a check of inner detector performance. Very low momentum muons (around a few GeV) may be difficult to reconstruct because they do not penetrate to the outermost stations.

Combined muons Both of the muon combination algorithms, Staco and Muid, match the muon-spectrometer tracks with inner-detector tracks to identify combined muons. The chi-square, defined as the difference between outer and inner track vectors weighted by their combined covariance matrix:

$$\chi^2_{match} = (\mathbf{T_{MS}} - \mathbf{T_{ID}})^{\mathrm{T}} (\mathbf{C_{ID}} + \mathbf{C_{MS}})^{-\mathbf{1}} (\mathbf{T_{MS}} - \mathbf{T_{ID}}) \tag{3.3}$$

provides an important measure of the quality of this match and is used to decide which pairs are retained. Here **T** denotes a vector of (five) track parameters—expressed at the point of closest approach to the beam line—and **C** is its covariance matrix. The subscript ID refers to the inner detector and MS to the muon spectrometer (after extrapolation accounting for energy loss and multiple scattering in the calorimeter).

Staco does a statistical combination of the inner and outer track vectors to obtain the combined track vector:

$$\mathbf{T} = (\mathbf{C_{ID}^{-1}} + \mathbf{C_{MS}^{-1}})^{-1} (\mathbf{C_{ID}^{-1}}\,\mathbf{T_{ID}} + \mathbf{C_{MS}^{-1}}\,\mathbf{T_{MS}}) \tag{3.4}$$

Muid fits the combined track, starting from the inner track fit and adding the points from the muon-spectrometer track.

3.3 The Fast detector simulation and reconstruction

The program ATLFAST [38] provides a fast simulation of the detector response in order to simulate large samples of signal and background events for physics studies. It is inserted in the official framework of the ATLAS experiment.
To keep the CPU time per event at a reasonable level, no interaction with materials is simulated and the detector description is based on parameterised smearing of particle kinematics according to a simplified detector model.
There are no separate steps for simulation and reconstruction. The basic informations on the detector that are taken into account, are listed here:

- geometry of the subdetector systems;
- dimension of the transition region between barrel and end-cap in the electromagnetic calorimeter;
- granularity of the hadronic calorimeter;
- effects of the magnetic field.

In the following I will briefly describe the ATLFAST algorithms concerning studies developed in this thesis.

3.3.1 Reconstruction algorithms

The reconstruction of the physics objects in ATLFAST relies to a large extent on the Monte Carlo truth information. Common to the reconstruction of all objects in ATLFAST is that by default no reconstruction efficiencies are applied. These efficiencies need to be taken into account by the user in the analysis. This applies to electrons, photons and jets as well as to ATLFAST tracks. It should be noted that efficiency factors are implicitly taken into account in the τ and b-tagging procedures.

In this section algorithms that allow to reconstruct events generated by a Monte Carlo generator will be described.

This is a schematic outline of the steps done by ATLFAST to reconstruct each event:

1. distinction between *isolated* and *non isolated* particles;
2. definition of *calorimetric clusters* from non isolated particles;
3. definition of *jets* from calorimetric clusters.

Since the physic channel studied in this thesis includes muons and jets, in the following I will briefly describe only the reconstruction alghoritms for these objects.

Muons

There is no simulation of tracking in ATLFAST either in the inner detector or in the muon spectrometer and reconstruction of muons is achieved by smearing their truth energy. For each true muon with $p_T > 0.5$ GeV the reconstructed momentum is calculated from the true muon momentum. A Gaussian resolution function which depends on p_T , η and ϕ is applied. In order to define *isolated muons* the following isolation criteria are applied to all muons that pass transverse momentum and rapidity cuts after smearing (by default: $p_T > 6$ GeV, $|\eta| < 2.5$):

- there should be no further energy deposit within a cone of $\Delta R = 0.4$ around the muon direction;
- the muon energy in a cone of $\Delta R = 0.2$ around the muon direction needs to be below a threshold (typically 10 GeV).

Muons that do not pass these isolation criteria are classified as *non isolated muons*.

Jets

Transverse energies of all *non isolated* particles are deposited in the calorimeter cells of granularity $\eta \times \phi$ 0.1×0.1 in the region $|\eta| < 3.2$ and 0.2×0.2 in the region $3.2 < |\eta| < 5$. The effect of the magnetic field on the ϕ position of charged particles is parametrized. No lateral or longitudinal shower development is simulated and no separation between hadronic and electromagnetic components is taken into account.
All the calorimeter cells in which an amount of transverse energy over a threshold (ATLFAST default: 0 GeV) has been deposited, are ordered as a function of increasing energy

($E_{T1} > E_{T2} > E_{T3} >$...). The most energetic cell, with at least $E_T > 1.5$ GeV, is considered as the seed of the cluster. Using the calorimeter cells created as above, clusters are formed using a cone algorithm with ΔR=0.4 and a minimum energy of 5 GeV is required for the resulting clusters.
The clusters may get re-classified as electrons, photons, taus or jets in one of the following steps. If they are associated to one of these objects they get removed from the list of clusters.

All clusters that have not been assigned to a true electron or to a photon are considered as jets with a required minimum transverse energy (including muons) typically set to 10 GeV. The jet energy is smeared according to the jet energy resolution, more details can be found in [12]. The jet direction coincides with the cluster direction. A separate jet calibration step corrects the jet energy for out-of-cone energy.

Jets labelling and tagging

In ATLFAST jet labelling is achieved by considering the truth parton content of the jet: a jet is labelled as a b-jet if a truth b quark with $p_T > 5$ GeV (after showering) is found within a cone of $\Delta R = 0.3$ around the jet axis. The same method is applied to tag a jet as a c or a τ-jet whenever a c quark or a τ lepton are found within a cone of $\Delta R < 0.3$ around the jet axis.
In the case none of the previous requirements are satisfied, the jet is labelled as a *light*-jet. No attempt was made to distinguish between u, d, s quarks and gluons.
In order to account for eventual large radiations from quarks and gluons from the hard process, only the last b (c) quark before hadronisation in the Monte Carlo particle collection is considered. The implementation of this condition is generator dependent.

The estimation of the b-tagging performance can be done using variables already defined in section 3.2.2: *b-tagging efficiency* (ε_b) and c and *light rejection* ($R_{c,l}$). As ε_b has a slow dependency on jet kinematics, ATLFAST set this value at a constant value of 60%. The rejection is derived from full simulation samples as a function of p_T and η separately for c, τ and *light* jets and in most physics analyses corresponds to c-jet and *light*-jet mis-tagging efficiencies of 10% and 1% respectively.

Tracks

Charged and stable particle tracks from the generator with $p_T > 0.5$ GeV and with $|\eta| < 2.5$ are considered as reconstructed ATLFAST tracks. Tracks in the Inner Detector with its solenoidal magnetic field are usually represented by the following five parameters:

- d_0: the transverse impact parameter;

- z_0: the longitudinal impact parameter;
- ϕ_0: the azimuthal angle;
- $\cot\theta_0$: the cotangent of the polar angle;
- $\frac{q}{p_T}$: the inverse transverse momentum proportional to the track curvature.

These parameters are calculated from the nominal position of the primary vertex. They are smeared with parametrized resolution functions which account for the measurement precision, energy loss and multiple scattering as well as for hadronic interactions in the Inner Detector material.
The output of the ATLFAST track selection and smearing procedure is the equivalent to a reconstructed track as resulting from full reconstruction.

Chapter 4

Studies using the FULL simulation

The main aim of this work has been to develop analysis techniques in order to extract events containing a Z boson decaying into a muon pair produced in association to a b jet from backgrounds. In this chapter I present a feasibility study of the expected number of events for signal and for the background channels for data corresponding to an integrated luminosity of 1 fb^{-1} performed with a set of fully simulated signal and background Monte Carlo samples. The same samples have been also used to test the performance of b-tagging algorithm, being this test necessary to accomplish the study of the Z+b jet channel.
The production of simulated data has been done by the ATLAS collaboration inside the Athena framework using *PYTHIA* and *SHERPA* Monte Carlo generators and the full simulation of the detector response.

4.1 Introduction

This section summarises the preparations for cross sections measurements. The aim of this summary is to understand which are the important variables that need to be evaluated using Monte Carlo data sample in order to measure cross sections when the experiment will start to take data.
Discussion on how to evaluate such variables will be given in next sections.

The measured cross section for a given channel is expressed as:

$$\sigma = \frac{N - B}{\mathscr{L}\,\varepsilon_S} \tag{4.1}$$

where N is the number of events selected applying a given set of cuts on collected data, B is the number of background events, $\mathscr{L}$ is the integrated luminosity and ε_S is the

efficiency of the signal. ε_S is often written as a product of the acceptance of the signal, (defined as the fraction of the signal that passes the kinematic and angular cuts) and the reconstruction efficiency of the signal within the fiducial acceptance [43].
The uncertainty on cross sections measurement gets contributions from the different terms. The uncertainty of N is of purely statistical origin depending only from the data collected from the experiment ($\delta N \sim \sqrt{N}$), and the relative uncertainty decreases with increasing luminosity following $\delta N/N \sim 1/\sqrt{\mathscr{L}}$. The uncertainty on the machine luminosity $\delta\mathscr{L}$ is expected to decrease through improved understading of the LHC beam parameters and of the luminosity detector response [13]. δB and $\delta\varepsilon_S$ are of both theoretical and experimental origin. They both depend from the limited Monte Carlo statistic available and from systematic limits on measurement (they can be due to reconstruction algorithms, theoretical uncertainties...).

In the next sections I will discuss on how to evaluate the efficiency of the signal ε_S and the number of background events B for an integrated luminosity of 1 fb^{-1} using the Monte Carlo data samples. In this chapter I will consider only contributions to the uncertainty on B and ε_S due to the limited statistic of Monte Carlo data sample used; a summary of the systematic uncertainties will be given in section 6.

4.2 Monte Carlo Data Samples and Cross Sections

In this section I will list the Monte Carlo data samples used to perform the analysis and their relative theoretical cross sections.

In this analysis pp $\rightarrow$ Z($\mu\mu$) + b jet + X is signal, where X states for everything in the final state produced in association to the leading process. The backgrounds can be distinguished in three cathegories. The first consists of events not containing a Z that decay into a muon pair, but involving muons in the final state that pass the isolation criteria appearing as muons from Z boson. In association to muons at least one jet is reconstructed and identified as a beauty jet. These events are: $t\bar{t}$ + X events involving at least one semileptonic decay in muon, Z $\rightarrow \tau\tau$ + X events with subsequent τ decay into muon, W $\rightarrow \mu\nu$ + X with a second muon coming from a jet or a second fake muon and QCD multi-jet events filtered to favour the presence of real muons or hadrons misidentified as muons ($b\bar{b}$ + X events). The second originates from events containing a Z boson decaying into a muon pair (as the signal), but with a c or light jet mis-identified as a beauty jet. These are Z ($\mu\mu$) + c/light jet + X events. The third category consists of Z ($\mu\mu$) + $q\bar{q}$ jets + X where q could be either beauty or charm or light jet. According to theoretical calculation that can be found in [18] the latter category is a negligible background in the LHC environment.

For this reason it has not been considered in this analyses.
Background events from cosmic muons can be eliminated in a very efficient way with timing cuts. Relying on the Tevatron results, this background was neglected in this work. This appears as a safe approximation for the ATLAS experiment, since the Tevatron experiments are built close to the surface, while the ATLAS detector is $\sim$ 100 m underground.

A list of all samples used to simulate signal and background events and their properties are reported in the following:

pp $\rightarrow$ Z($\mu\mu$) + b jet + X

The signal sample pp $\rightarrow$ Z($\mu\mu$) + b jet + X has been generated with Sherpa 1.0.9. The events are preselected with a generator-level filter requiring two muons with $p_T^\mu > 5$ GeV, $|\eta^\mu| < 3$.
These filters have an efficiency of more than 90%.

pp $\rightarrow$ Z($\mu\mu$) + c/light jet + X

This sample pp $\rightarrow$ Z($\mu\mu$) + c/light jet + X is a background when the charm or the light jet is mistagged as a beauty jet.
It has been generated with Sherpa 1.0.9. The events are preselected with a generator-level filter requiring two muons with $p_T^\mu > 5$ GeV, $|\eta^\mu| < 3$.
These filters have an efficiency of more than 90%.

pp $\rightarrow$ Z($\mu\mu$) + X

The inclusive sample pp $\rightarrow$ Z($\mu\mu$) + X includes both signal (when X contains at least one beauty jet) and background events (when X contains charm or light jets).
It has been generated with Pythia 6.403. The events are preselected with a generator-level filter requiring at least one muon with $p_T^\mu > 5$ GeV and $|\eta^\mu| < 2.8$, and a dimuon invariant mass greater than 60 GeV.
These filters have an efficiency of about 90%. This sample has been used both for signal and background studies. It has been also used in order to compare results with the ones obtained from pp $\rightarrow$ Z($\mu\mu$) + b/c/light jet + X Sherpa samples.

pp $\rightarrow$ W ($\mu\nu$) + X

The inclusive pp $\rightarrow$ W ($\mu\nu$) + X sample can be a background when X contains a jet identified as a beauty jet and a second real or fake muon pass the isolation criteria (together

with the muon from the W) appearing as from the Z boson.
It has been generated with Pythia 6.403 The events are preselected with a generator-level filter requiring $p_T^\mu > 5$ GeV, $|\eta^\mu| < 2.8$.
These filters have an efficiency of about 70%. This sample has been used not only as a background, but also to control the mis tagging rate as it will be discussed in section 4.5.

pp $\rightarrow t\bar{t}$ + X

The pp $\rightarrow t\bar{t}$ background dijet sample has been generated with a Pythia 6.403 using a generator level filter which requires two electro magnetic clusters of energy and at least one semileptonic decay.
These filters have an efficiency of about 55%.

pp $\rightarrow$ Z($\tau\tau$) + X

The inclusive pp $\rightarrow$ Z($\tau\tau$) + X sample is a background when X contains a jet identified as a beauty jet and when the τ leptons decay into muons that pass the isolation criteria appearing directly as from the Z boson.
It has been generated with Pythia 6.403. The events are preselected with a generator-level filter requiring at least one τ lepton with $p_T^\tau > 5$ GeV and $|\eta^\tau| < 2.8$ and a $\tau\tau$ invariant mass greater than 60 GeV.
These filters have an efficiency of about 5%.

QCD background (pp $\rightarrow b\bar{b}$ + X)

QCD multi-jet backgrounds for isolated highly-energetic muons result mainly from decays of $b\bar{b}$ mesons. I thus use a $b\bar{b}$ ($\mu\mu$) sample to evaluate this background. The sample has been generated with Pythia 6.403. Two muons, one with $p_T^\mu > 4$ GeV and the other with $p_T^\mu > 6$ GeV, within the trigger acceptance of $|\eta^\mu| < 2.4$ are required in the final state.
These filters have an efficiency of the order of 10^{-4} %.

A summary of the relevant informations (including cross sections) for the datasets used is shown in table 4.1. Reference cross sections used for this analysis are collected in [42]. From now on I will not include the X letter in mentioning the samples, implying that each sample in the final state can contain other particles or jets produced in association to the leading process.

Samples	Number of events	$\int Ldt$ (pb^{-1})	Cross sections σ (pb)
pp $\rightarrow Z \rightarrow \mu\mu$ + b jet	9500	181.6	52.3
pp $\rightarrow Z \rightarrow \mu\mu$ + c/light jet	4000	4.3	930
pp $\rightarrow Z \rightarrow \mu\mu$	263550	130.1	2015
pp $\rightarrow W \rightarrow \mu\nu$	114800	5.6	20510
pp $\rightarrow t\bar{t}$	62000	117.6	833
pp $\rightarrow Z \rightarrow \tau\tau$	152400	75.63	2015
pp $\rightarrow b\bar{b}$	29500	0.27	110500

Table 4.1: Fully simulated signals and background samples. W($\mu\nu$), Z($\mu\mu$) and Z($\tau\tau$) inclusive cross sections are normalised to the NNLO prediction; all the other sample cross sections are computed at NLO. Cross sections quoted here are collected in [42].

4.3 Events Selection

In this section I will discuss on how to select the Z ($\mu\mu$) + b jet signal from background events.

The selection efficiency of a sample is defined as the fraction of the sample that passes the kinematic and angular cuts on muons and jets in the final state. In the following I will list and discuss on these cuts and I will report the efficiencies obtained after the application of the cuts themselves on the events of different data samples.

4.3.1 Muons

The muon reconstruction is done with the muon spectrometer combined with the inner detector (see also section 3.2.2 for further details).
The Staco collection [34] is the current default for physics analysis inside the Atlas Collaboration but future analyses may make use of the Muid collection [33] or a mixture of muons drawn from both of these and any future collections. I used the Staco muon container requiring for each event at least two muons with opposite charge. The reconstructed muon tracks should satisfy $p_T > 15$ GeV and $|\eta| < 2.4$.
Muons in jet tend to be produced within a decay cascade of further particles, and should therefore not appear isolated in the detector, in contrast to the leptonic decays of Z boson. Isolation is applied by requiring the angular distance between the two muons ($\Delta R_{\mu\mu} = \sqrt{\Delta\eta^2_{\mu\mu} + \Delta\phi^2_{\mu\mu}}$) greater than 0.5.
The invariant mass of the muon pair is required to fulfil 70 GeV $< M_{\mu\mu} <$ 110 GeV. If

more than two muons are reconstructed, the pair with the invariant mass closest to the M_Z = 91.1876 ± 0.0021 [1] is chosen.

Figure 4.1 (a) shows the transverse momentum spectrum for all the muons found in the analyzed data samples within $|\eta| < 2.4$, before any other cut is applied. Figure 4.1 (b) shows the angular distance $\Delta R_{\mu\mu}$ between two muons of opposite charge, transverse momentum above 15 GeV and $|\eta| < 2.4$. The two plots are scaled to $\int Ldt = 1\,\mathrm{fb}^{-1}$ of integrated luminosity. From figure 4.1 (b) it is clear that the decision to cut on the angular distance between the two muons $\Delta R_{\mu\mu} > 0.5$ has been taken primarly to reduce QCD ($b\bar{b}$) background.

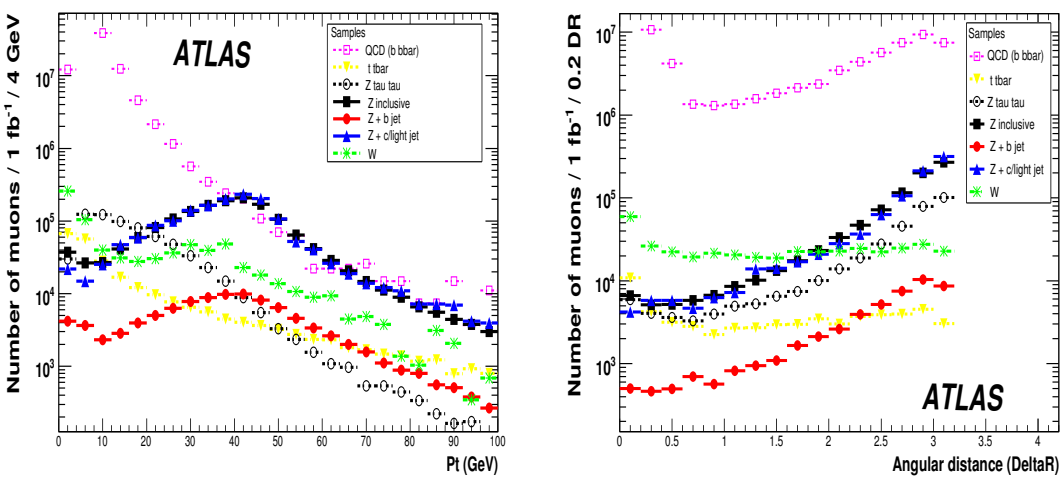

(a) (b)

Figure 4.1: (a) : Distribution of the muon transverse momentum in $|\eta| < 2.4$ before any other selection cut. (b): Distribution of the angular distance $\Delta R_{\mu\mu}$ between two muons of opposite charge, transverse momentum above 15 GeV and $|\eta| < 2.4$. The two plots are scaled to $\int Ldt = 1\,\mathrm{fb}^{-1}$ of integrated luminosity.

Figure 4.2 shows the invariant mass of the muon pair, after cuts on muons. The plot is normalized to 1 fb^{-1} integrated luminosity.

From this figure we see that cutting on muons considerably reduce backgrounds not containing a Z decaying into muons ($t\bar{t}$, Z $\rightarrow \tau\tau$, W $\rightarrow \mu\nu$ and QCD multi-jet $b\bar{b}$ events). The subsequent request on the invariant mass range of the muon pair (70 GeV $< M_{\mu\mu} <$ 110 GeV) allows to an even better selection of the signal over the backgrounds of above.

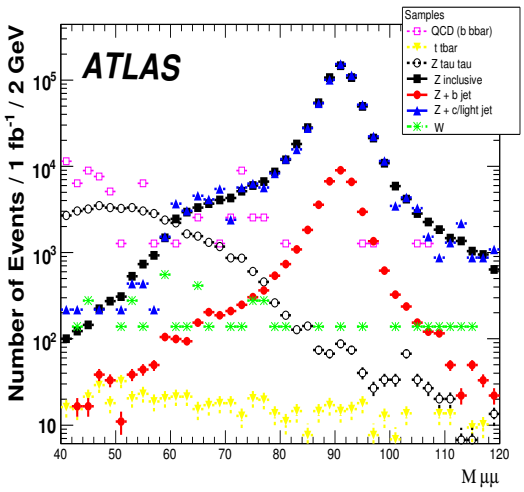

Figure 4.2: Invariant mass of the muon pair after muon selection cuts. The plot is normalized to 1 fb^{-1} integrated luminosity.

4.3.2 Jets

In this thesis the standard cone algorithm jet reconstruction available in the ATLAS software is used. A jet is therefore defined by a direction, an energy and a cone size that corresponds to the jet opening angle. I used jets clustered with the standard ATLAS seeded-cone algorithm with a radius of ΔR=0.4, built from topological cluster (see section 3.2.2).
It is required at least one jet in the event with transverse momentum $p_T > 20$ GeV in the range $|\eta| < 2.4$. In order to remove jets faking muons in the signal analysis, the angular distance between Figure 4.3 shows the transverse momentum (a) and pseudo rapidity (b) distributions for signal and background events.

Figure 4.4 shows the transverse momentum (a) and pseudo rapidity (b) distributions of jets after cuts on muons and muon pair discussed in the previous section. All distribution are normalized to $\int Ldt = 1\,\mathrm{fb}^{-1}$ of integrated luminosity.

.

Comparing fig. 4.3 and fig. 4.4 we can conclude that the shape of distributions is not influenced by the cuts on muons and muon pair. Those cuts only reduce the fraction of background from the signal.

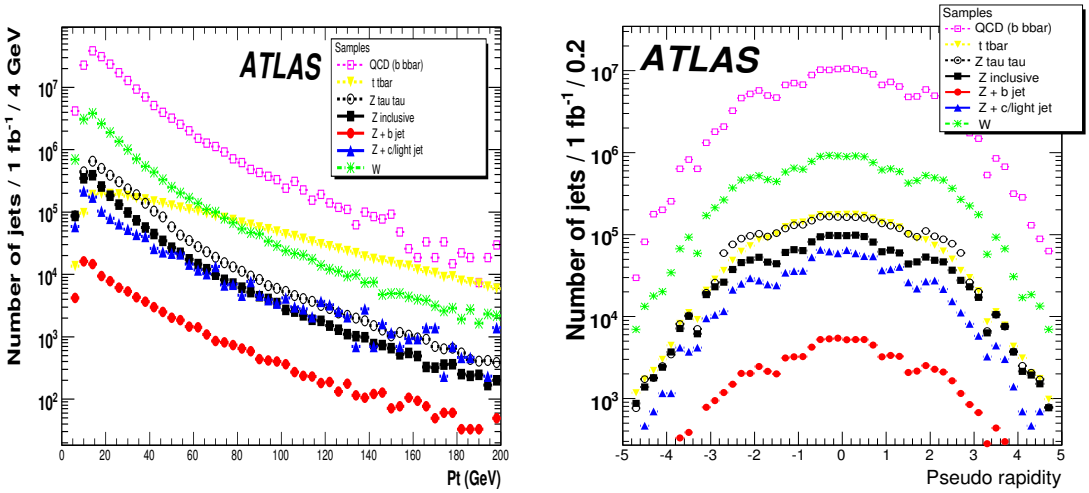

(a) (b)

Figure 4.3: Transverse momentum (a) and rapidity (b) distributions of jets.

4.3.3 Jet tagging

Realistic estimation of rejection/mistag rate is crucial to the studies which depend on b-tagging.
In this analysis jets are labelled as b-jets using the b tagging algorithm with the highest light-jet rejection power. This algorithm makes use of the 3D impact parameter and secondary-vertex reconstruction, IP3D+SV1. As already discussed in section 3.2.2, tracks from B-hadrons decays are expected to have on average a large and positive transverse impact parameter a_0 and a large and positive longitudinal impact parameter z_0. Combining the longitudinal and trasverse significance in the function: $w_t = P_b(S_{a_0,z_0})/P_u(S_{a_0,z_0})$ and applying a cut on the likehood function is possible to discriminate b jets from c and light jets (see [44] for additional information about the algorithm).
In this analysis I cut on the b tagging weight parameter $weight \geq 5$.
An explanation on why the value of 5 has been chosen to cut on the b-tagging weight will be given in the following section.

4.3.4 Tests of b-tagging

Here I will discuss how to choose the value for the b tagging weight parameter in order to maximize both the efficiency in selecting Z + b jet events and the rejection of the

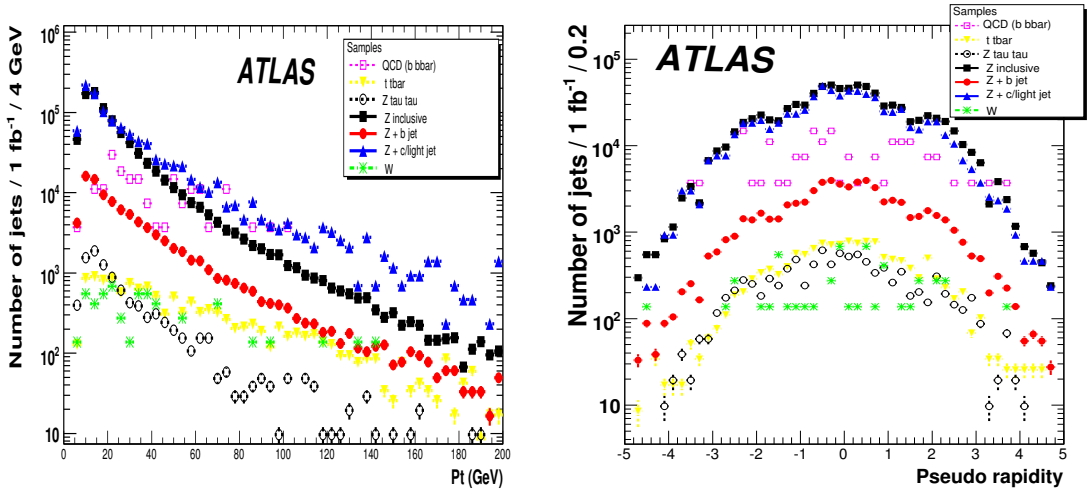

(a) (b)

Figure 4.4: Transverse momentum (a) and rapidity (b) ditributions of jets after cuts on muons inside the invariant mass range 70 GeV $< M_{\mu\mu} <$ 110 GeV and before any cut on jets.

backgrounds where a Z is produced in association to a charm or a light jet and I will give an explanation on why it has been chosen to require the b tagging weight greater than 5.

Definitions and Events Selection

In order to define the Z + b jet efficiency and Z + c/light jet rejection, it is needed to know how many jets derive from bottom, charm and light quarks. In other words, we need to know the true flavor of the jet from the Monte Carlo truth informations. I remind that a jet is labelled as a b-jet if a b quark with $p_T > 5$ GeV is found in a cone size ΔR =0.3 around the jet axis. Same procedure applies for c and τ jets. If no beauty or charm or τ is found, the jet is labelled as light (u, d, s, g).

In section 3.2.2 I defined *b-jet efficiency*, *mistag probability* and *rejection* per jet, here I recall the definitions and describe the cuts used in this analysis, but I will apply them per event.

The *Z + b jet efficiency* ε_b is defined as the ratio between the number of events containing at least one Cone 0.4 true b-jet (from the MC truth informations) with $E_T > 15$ GeV and $|\eta| < 2.5$ above a chosen b tagging weight cut, and the number of events containing

at least one Cone 0.4 true b-jet inside the same transverse energy and rapidity ranges but before cutting on the b tagging weight.

The Z + *b jet mistag probability* is the probability that a given event containing a non b-jet (from the MC truth informations) inside the same transverse energy and rapidity ranges ($E_T > 15$ GeV and $|\eta| < 2.5$) is tagged ad a Z+ b-jet event ($\varepsilon_{mis_{c/l}}$).

The Z + *c/light jet rejection* factor is defined as the inverse of, respectively, c and light jets mistag probability: $R_{c/l} = 1/\varepsilon_{mis_{c/l}}$. As an example R=100 means 1% mistag rate.

The b-tagging efficiency for Z + b jet events has been derived using the Monte Carlo sample pp $\rightarrow$ Z($\mu\mu$) + b jet , while the evaluation of the rejection factor for Z+c/light jet was done using the inclusive pp $\rightarrow$ Z($\mu\mu$) sample (because of the poor statistic of pp $\rightarrow$ Z($\mu\mu$) + c/light jet sample).

Results and distributions

Figure 4.5 (a) shows the b-tagging efficiency as a function of the weight parameter after event selection cuts (listed in section 4.3). Figure 4.5 (b) shows the rejection factor for c and light quarks as a function of the b-tagging efficiency after the same selection cuts.
From the two figures it is possible to decide at which weight it is good to cut in order to maximize b tagging efficiency ε_b and c and light rejection $R_{c/l}$.
I decided to cut at *b tagging weight* ≥ 5: this ensures an efficiency of $\sim 60\%$ for signal events and gives rejection factors $R_c \sim 7$ for Z($\mu\mu$) + c jet and $R_l \sim 110$ for Z($\mu\mu$) + light jet background events, in fairly good agreement with what is found for other physics channels [44, 45].

In order to see how the chosen cut on the b tagging weight parameter acts on the transverse momentum distributions of jets of different flavors produced in association to a Z boson, I used the pp $\rightarrow$ Z($\mu\mu$) inclusive data sample and I selected from the Monte Carlo Truth information the flavor of the jets dividing in the following categories:

- b jets;
- c jets;
- light or gluon jets;
- all jets of all flavour (it is the sum of all the three previous categories).

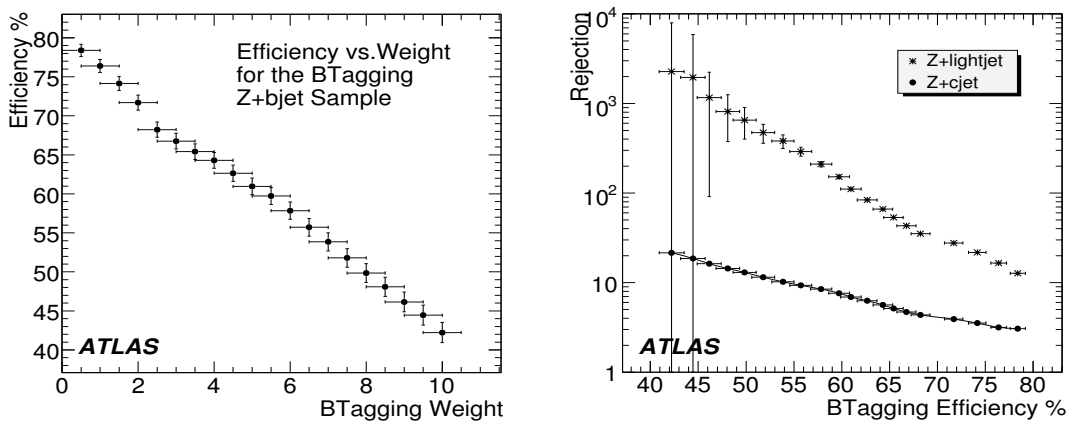

(a) (b)

Figure 4.5: B-tagging efficiency as a function of the weigth parameter (a). Rejection factor for c (black squares) and light (black stars) jets as a function of the b-tagging efficiency (b).

Figure 4.6 (a) shows the jet transverse momentum spectrum for beauty, charm and light/gluon jets after cuts on muon pair and on jets. Figure 4.6 (b) shows the same events of (a) when the cut on the b-tagging weight is also added.

These distributions reflect the efficency for Z($\mu\mu$) + b jet events selection and the rejection factor for Z($\mu\mu$) + c/light jet events reachable when we apply the cut on b tagging weight parameter *weight* ≥ 5. In fact it can be noticed that the application of this cut allows to extract the signal events with an efficiency of about 60% and that the selected events obviously contain background contamination from events containing a Z boson and jets that are mistagged as b jets.

Figure 4.7 (a) shows the jet multiplicity for all the samples after selection on muon pair. The same distribution after requiring b tagging weight parameter *weight* ≥ 5 is in figure 4.7 (b). The distributions are normalized to $\int Ldt = 1\,\mathrm{fb}^{-1}$ of integrated luminosity.

As it is expected, samples that are dominated by the presence of at least one b-jet per event (signal and QCD $b\bar{b}$ background) are not so much influenced by the cut on b tagging weight, while the other samples are depressed. The depression factor increases with the increasing of jets multiplicity.

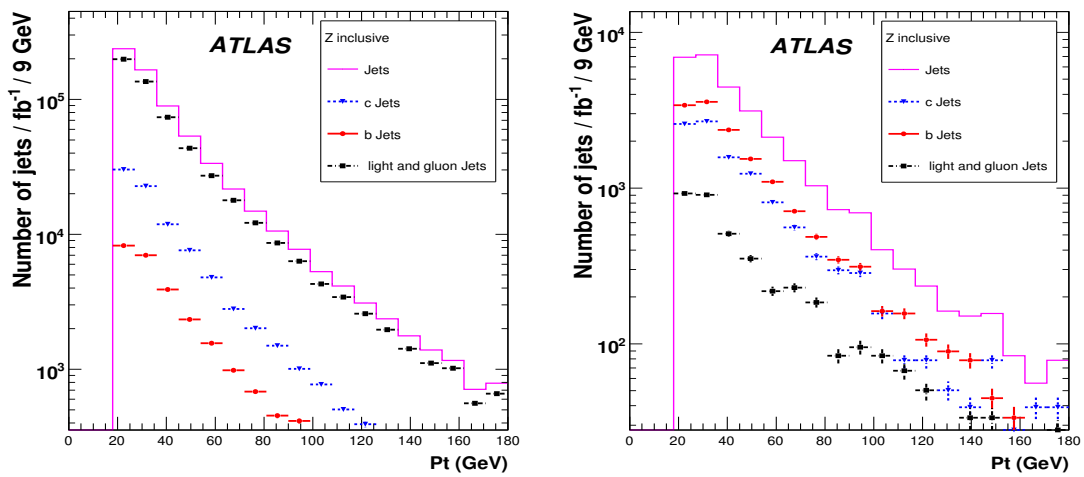

(a) (b)

Figure 4.6: Jet transverse momentum spectrum for beauty, charm and light/gluon jets in the pp $\rightarrow$ Z($\mu\mu$) inclusive data sample, before (a) and after (b) the cut on the b-tagging weight.

4.3.5 Event selection efficiency

In this section I want to give the event selection efficiencies on signal and background samples obtained after the application of cuts on muons and jets in the final states discussed in section 4.3.
The signal and background samples used for this analysis have been described in section 4.2. I recall and list here all the requirements for events selection:

- at least two muons of opposite charge per event;
- $p_T^{\mu} > 15$ GeV;
- $|\eta^{\mu}| < 2.4$;
- $\Delta R_{\mu\mu} > 0.5$;
- 70 GeV $< M_{\mu\mu} <$110 GeV.
- $\Delta R_{\mu-jet} > 0.4$;
- $p_T^{jet} > 15$ GeV;

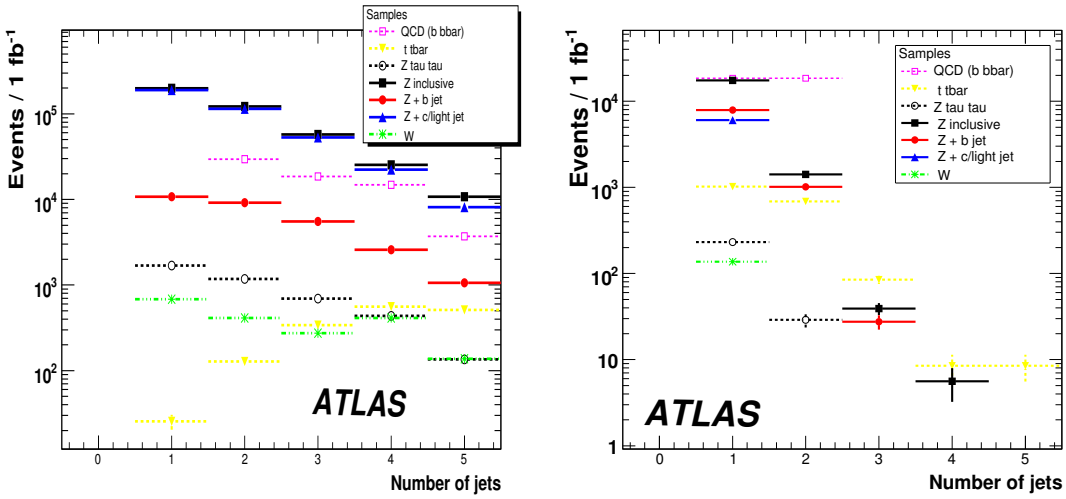

(a) (b)

Figure 4.7: Jet multiplicity before cutting on jets (a) and after requiring b tag weight > 5 (b). All distributions have been obtained after cuts on muons and muon pair invariant mass and normalized to $\int Ldt = 1\,\text{fb}^{-1}$ of integrated luminosity.

- $|\eta^{jet}| < 2.5$;

The selection efficiency is defined as

$$\varepsilon = \frac{N_{sel}}{N_{tot}} \tag{4.2}$$

where N_{sel} is the number of events selected after the requirements of above, while N_{tot} is the number of events in each original sample of Monte Carlo data (see table 4.1). The uncertainty on efficiency is of purely statistical origin.

The achievable efficiencies after the cuts on muons and muon pair invariant mass are shown in table 4.2. All cuts have been applied sequentially. The percentages are referred to the total number of events in each sample.

After the selection of events that satisfies cuts on muons and di-muon invariant mass, requirements on jets multiplicity, angular distance between jets and muons, transverse momentum, rapidity distribution and b tagging weight have been applyed. Efficiencies obtained applying these cuts sequentially are listed in table 4.3.

Results of tables 4.2 and 4.3 have been used to estimate the fraction of signal and background events in a selected sample of 1 fb^{-1} of data. These estimations allow to

Samples	at least 1 μ^+ and 1 μ^- $\Delta R_{\mu-\mu} > 0.5$	$p_T^{\mu} > 15$ GeV $\lvert\eta^{\mu}\rvert < 2.4$	$70 < M_{\mu\mu} < 110$ GeV
$Z \to \mu\mu$	56.9±0.3	43.3±0.2	40.8±0.2
$Z \to \mu\mu$ + b jet	91.1±2.0	74.1±1.6	70.8±1.6
$Z \to \mu\mu$ + c/light jet	92.7±3.0	74.1±2.5	69.4±2.4
$t\bar{t}$	11.4±0.1	1.8±0.1	0.49±0.03
$W \to \mu\nu$	2.52±0.05	0.044±0.006	0.013±0.003
$Z \to \tau\tau$	23.1±0.2	3.3±0.1	0.40±0.02
QCD $b\bar{b}$	76.1±0.1	0.12±0.02	0.06±0.01

Table 4.2: Selection efficiencies (expressed in %) after the cuts on muons and muon pair.

Samples	at least 1 jet per event	$\Delta R_{\mu-jet}$ >0.4	$p_T^{jet} > 20$ GeV $\lvert\eta^{jet}\rvert < 2.5$	btag weight $w_{jet} > 5$
$Z \to \mu\mu$	28.8±0.2	22.0±0.1	14.9±0.1	1.13±0.02
$Z \to \mu\mu$ + b jet	56.6±1.3	42.7±1.1	28.3±0.8	15.4±0.6
$Z \to \mu\mu$ + c/light jet	45.4±1.8	31.2±1.4	17.6±0.9	0.5±0.1
$t\bar{t}$	0.49±0.03	0.39±0.03	0.39±0.03	0.34±0.02
$W \to \mu\nu$	0.013±0.003	0.010±0.003	0.010±0.003	0.009±0.001
$Z \to \tau\tau$	0.29±0.01	0.23±0.01	0.15±0.01	0.020±0.003
QCD $b\bar{b}$	0.06±0.01	0.05±0.01	0.05±0.01	0.03±0.01

Table 4.3: Selection efficiencies (expressed in %) after the cuts on jets (cuts on muons from table 4.2 are also included).

obtain the number of background events B and the efficiency of the signal events (ε_S) that are in the formula 4.1. Such estimations will be discussed in the next section.

4.4 Number of events and ratio of cross sections

In this section I will give a first estimation of the expected number of events and the corresponding fraction of the total sample for signal and for the background channels after applying the cuts outlined in in section 4.3 for an integrated luminosity of $1\,\mathrm{fb}^{-1}$. The obtained values will be used to evaluate the cross section ratio between the signal $Z \to \mu\mu$ + b jet and the inclusive $Z \to \mu\mu$ + jets cross section.

4.4.1 Number of events

The number of events N_{ev} passing a given set of selections is expressed as follows:

$$N_{ev} = \mathscr{L}\,\sigma\,\varepsilon \tag{4.3}$$

where $\mathscr{L}$ is the integrated luminosity; σ is the cross section of the channel we are considering; ε is the selection efficiency of the sample defined as the fraction of the sample that passes the kinematic and angular cuts.

I used the formula 4.3 to give an estimation of the sample composition for an integrated luminosity of $1\,\mathrm{fb}^{-1}$ after the events selection discussed in section 4.3. Cross sections used to perform the calculation are listed in table 4.1, efficiencies are reported in tables 4.2 and 4.3.

The uncertainty on the number of selected events gets contributions from all the variables in 4.3. In this analysis the uncertainty on the machine luminosity $\mathscr{L}$ has not been considered.
The uncertainties due to the theoretical cross sections calculations are negligible respect to uncertainties on the efficiencies. δN_{ev} has been therefore evaluated from the propagation of efficiencies uncertainties quoted in tables 4.2 and 4.3. These are due to the limited number of events of the Monte Carlo data samples available for this analysis.

Table 4.4 shows the composition (in %) of a selected sample of $Z \to \mu\mu$ + jet events. The requirement on b tagging weight to select events containing a b jet has not yet been applied.

Samples	%	$N_{ev} \pm \delta_{ev}$
$Z \to \mu\mu$	83 ± 3	300000 ± 2000
$t\bar{t}$	0.8 ± 0.1	3300 ± 200
$W \to \mu\nu$	0.6 ± 0.2	2000 ± 600
$Z \to \tau\tau$	0.8 ± 0.1	3000 ± 200
QCD $b\bar{b}$	15 ± 3	55000 ± 11000

Table 4.4: Fraction of the total sample of $Z \to \mu\mu$ + jets events (in %) and number of expected events for an integrated luminosity of 1 fb^{-1} after applying the cuts outlined in section 4.3 not including b tagging. The quoted uncertainties refer to the finite Monte Carlo statistics.

The invariant mass of muon pair after all the selection cuts but the b tagging weight, is shown in fig. 4.8 (a). Not including the cut on the b tagging weight means that we are

selecting $Z \to \mu\mu$ + jets with no preference on the jets flavor. The dominant background to this selected sample comes from QCD jets events, as evident from table 4.4.

Samples $Z \to \mu\mu$ + b jet and $Z \to \mu\mu$ + c/light jet have been used to estimate the fraction of the $Z \to \mu\mu$ inclusive sample containing a beauty or a charm jet.The result is that the fraction of events containing a b jet correctly tagged is (63 $\pm$ 8) % over the total. This means that after all cuts (including the b tagging, see table 4.3) the number of events selected in the $Z \to \mu\mu$ sample contains a fraction of mistagged events of the order of (37 $\pm$ 11) %. Errors associated to the estimation are due only to statistics.
This result is in agreement with the signal efficiency $\varepsilon_b \sim 60\%$ found in section 4.3.4 using the $Z \to \mu\mu$ inclusive sample. Based on rejection results for events containing light jets ($R_l \sim 110$) and for events with c jet ($R_c \sim 7$), we can assume that the contamination of the signal is essentially due to $Z \to \mu\mu$ + c jet events (being the one from $Z \to \mu\mu$ + light jet negligible).

Taking into account the fraction of mistagged events it is possible to give a final estimation of signal events and background contamination after all cuts, (including b tagging weight). Table 4.5 shows the composition (in %) of a selected signal sample after all selection cuts have been applied.

Samples	%	$N_{ev} \pm \delta_{ev}$
$Z \to \mu\mu$ + b jet	25 $\pm$ 5	14500 $\pm$ 200
$Z \to \mu\mu$ + c jet	13 $\pm$ 3	8500 $\pm$ 200
$t\bar{t}$	4.5 $\pm$ 1.1	2800 $\pm$ 200
$W \to \mu\nu$	2.9 $\pm$ 0.8	1800 $\pm$ 200
$Z \to \tau\tau$	0.6 $\pm$ 0.2	400 $\pm$ 60
QCD $b\bar{b}$	63 $\pm$ 34	33000 $\pm$ 11000

Table 4.5: Fraction of the total sample (in %) and number of expected signal and background events for an integrated luminosity of 1 fb^{-1} after all selection cuts. The quoted uncertainties refer to the finite Monte-Carlo statistics.

The composition of the sample can also be seen from the distribution of the invariant mass of the muon pair in figure 4.8 (b).

As expected, the most important background after all cuts is the QCD ($b\bar{b}$) jets. This is due to the fact that the cross section is very high with respect to the signal and also because this background contains true b jets. Cutting on the b tagging weight allow to reduce

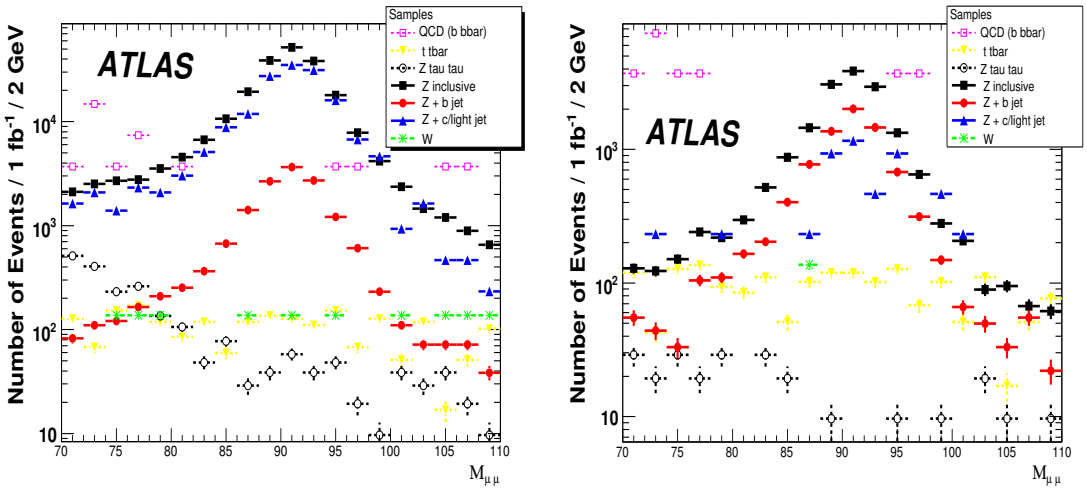

(a) (b)

Figure 4.8: Invariant mass of the two muons after cuts on muons, muon pair and jets not including the b tagging weight cut (a) and including it (b). The plots are normalized to 1 fb^{-1} integrated luminosity.

background from samples not containing b jets, but increase the fraction of background with true b jets in the selected events.
It is possible to reduce this background reducing the invariant mass range of the muon pair in order to exclude a bigger fraction of ($b\bar{b}$) events. If I cut on the invariant mass range $M_Z\pm$ 10 GeV (instead of the previous $70 < M_{\mu\mu} < 110$ GeV) leaving unchanged all other cuts on muons and jets, the fraction of the signal sample increases respect to the background.

Results after applying all cuts on muons and jets in the new invariant mass range of $M_Z\pm$ 10 GeV are shown in table 4.6. Errors are due only to statistics.

In this case the QCD ($b\bar{b}$) has been reduced and we can also see that the error associated to this background estimation is very big due to the limited statistics of the sample itself. More we reduce the mass range and more the low statistic does not allow to have a precise estimation of this background.
In order to better estimate the contamination of the signal due to this background further studies are required with larger QCD jets MC samples. Neverthless, in the future it will be possible to reduce the percentage from this backgrond exploiting different methods. One of this method could be to fit on the di-muon pair invariant mass.

In addition, Tevatron experience [**?**, 46] make us confident that real data will help in

Samples	%	$N_{ev} \pm \delta_{ev}$
$Z \to \mu\mu$ + b jet	45 ± 9	13600 ± 200
$Z \to \mu\mu$ + c jet	24 ± 5	7200 ± 200
$t\bar{t}$	5.1 ± 1.5	1600 ± 200
$W \to \mu\nu$	0.6 ± 0.6	200 ± 200
$Z \to \tau\tau$	0.3 ± 0.2	100 ± 40
QCD $b\bar{b}$	25 ± 22	7700 ± 5500

Table 4.6: Fraction of the total sample (in %) and number of expected signal and background events for an integrated luminosity of 1 fb^{-1} after all selection cuts in the invariant mass range of $M_{\mu\mu} \pm$ 10 GeV. The quoted uncertainties refer to the finite Monte-Carlo statistics.

improving the discrimination between signal and QCD ($b\bar{b}$) jets background. In such a case one of the main background remains Z($\mu\mu$) + c jet . A method to better discriminate this background from the signal will be discussed in the next chapter.

4.4.2 Ratio of cross sections

In this section I want to give a first estimation of cross section ratio between the signal $Z \to \mu\mu$ + b jet and the inclusive $Z \to \mu\mu$ + jets cross section using results reported in tables 4.4 and 4.5. Looking at ratios instead of a single cross section is also useful because some systematic uncertainties can be partially removed.

The value obtained from the analysis described in the previous section is the following:

$$[\frac{\sigma(Z \to \mu\mu + b jet)}{\sigma(Z \to \mu\mu + jets)}]_{analysis} = 0.048 \pm 0.001 \tag{4.4}$$

The uncertainty refers only to the finite Monte Carlo statistics.

We can make a comparison between this result and the theoretical prediction obtained running the MCFM [28] program within the same cuts on muons, muon pair and jets that have been used in the analysis to select the signal (see sec. 4.3). The cone algorithm 0.4 has been chosen to define jets and the PDF sets CTEQ6M has been used.

The cross section obtained with MCFM for the signal channel is in agreement with the one found from the analysis on Monte Carlo data samples:

$$[\frac{\sigma(Z \to \mu\mu + bjet)}{\sigma(Z \to \mu\mu + jets)}]_{MCFM} = 0.0479 \pm 0.0002 \tag{4.5}$$

Theoretical uncertainties have been automatically estimated by MCFM. They arise from the choice of the renormalisation and factorisation scales, and they also include PDF uncertainty.

The same ratio has been already evaluated by CDF [46] and D0 [47] experiments at Tevatron, finding a very good agreement with theoretical predictions calculated using the MCFM program.

4.5 b-tagging algorithm using pp $\to$ W $(\mu\nu)$ inclusive sample

For analysis using b tagging, the estimation of the backgrounds from well-known Standard Model processes requires to know the tagging and mistagging efficiency for the various flavors of jets with high accuracy. The quality of Monte Carlo simulation of these properties is unknown and therefore strategies must be developed to measure the tagging and mistagging efficiencies directly from data. The b-tagging efficiency can be checked using b-enriched samples.

We have seen in the previous section that a non negligible amount of background in the selected sample is due to mis-tagged jets from c and light quarks. This can be controlled by looking at the number of tagged jets in data samples that in principle should not contain b-jets at first order: W + jets production, for example, is such a kind of events. The W + jets events will be available with large statistics, in addition jets produced in association with W boson will cover the full p_T range of the signal.

The inclusive $W \to \mu\nu$ sample has been used to estimate the mis tagging rate as a function of the transverse momentum of the jet produced in association to the W boson.

4.5.1 Events Selection and Results

I analized events containing a muon from W decay within kinematic cuts on muon and jets in the final state already listed in section 4.3. I recall them here:

- at least one muon in the event with:

- $p_T^{\mu} > 15$ GeV;
- $|\eta^{\mu}| < 2.4$;

- at least one reconstructed Cone 0.4 jet with:.
  - $p_T^{jet} > 20$ GeV;
  - $|\eta^{jet}| < 2.5$;

After these selections, I looked for events where at least one jet is tagged as a b-jet by the b-tagging algorithm ($w_{jet} > 5$). In this way it has been possible to calculate the number of event with at least one mistagged jet with respect to the total number of events as function of the jet transverse momentum p_T.
As we can see in figure 4.9 we expect a mistagging rate at the level of few percent over the full p_T range of the signal per event.
This result is in good agreement with previous results obtained using fast simulation on a W+jet sample [61].

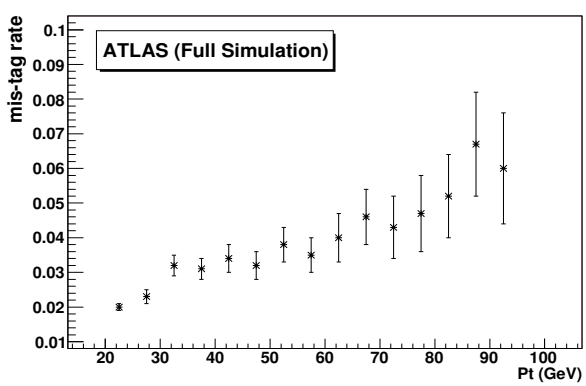

Figure 4.9: Mistagging rate of b-jets evaluated from fraction of b-tagging jets in the pp $\rightarrow$ W $(\mu\nu)$ sample: relative error on background level per 5 GeV jet p_T bin.

Chapter 5

Studies using the FAST simulation

The production of data sample used to perform the analysis discussed in this chapter has been done inside the Athena framework. The Monte Carlo chosen to produce these data samples is *PYTHIA*.
The pseudo data obtained with the fast simulation have been used basically for two reasons: to perform preliminary studies on the parton distribution function of the b quark using different PDF sets and to study the behaviour of some variables that can help in distinguishing b jets from c jets. This latter study was done to see if is it possible to find variables that allow to reach a better or comparable efficiency and purity of the signal and in particular a better rejection of Z($\mu\mu$) + c jet events respect to the one obtained using the b tagging weight variable.

5.1 Preliminary studies of b density function

An important source of theoretical systematic uncertainties at the LHC is represented by the Parton Distribution Functions (PDF). If the understanding of the perturbative corrections to the hard scattering in the Z inclusive and Z+ jets cross sections is in good shape [60], the uncertainty on the PDFs can limit the accuracy of the theoretical predictions on cross section measurements. This uncertainty will limit the differential cross section measurements and distributions of various observables in different channels (for example the transverse momentum, the rapidity distribution of weak bosons or jets).

In this section I will show a preliminary study involving two different PDF sets in the pp $\rightarrow$ Z($\mu\mu$) + jets channel: CTEQ6l [48] and MRST2004 [50]. The study has the purpose to give a first rough estimation of the impact of the PDF uncertainty on transverse momentum and rapidity distribution of the Z boson produced in association to a b-jet.

5.1.1 Monte Carlo Data Samples

The samples used for this study have been generated with the PYTHIA Monte Carlo package [23] interfaced to the library containing informations about different PDF sets: LHAPDF [56]. The detector response has been simulated using the ATLFAST package [38].
In order to produce these samples I started from the official JobOption used by the Atlas collaboration to generate and fully simulate the pp $\rightarrow$ Z($\mu\mu$) inclusive channel [55]. The above JobOption has been modified to require the presence of at least one jet in the final state, to change the PDF sets and to be interfaced to the ATLFAST package.

The following samples have been produced:

- pp $\rightarrow$ Z($\mu\mu$) + jets : CTEQ6l [48];
- pp $\rightarrow$ Z($\mu\mu$) + jets : MRST2004 [50].

The two samples have been generated without requiring any filter on muons from the Z decay, but asking for a transverse momentum of the the jets greater than 10 GeV in order to avoid divegences in the cross sections. 200K events have been generated for each of the above samples. The energy scale and Bjorken variable range of validity for each PDF sets is reported in table 5.1 . For the study discussed in this thesis, the two ranges are equivalent, since we are not sensible to x values less than 10^{-5} GeV^2 and Q^2 bigger than 10^7 GeV^2.

PDF set	x_{min}	x_{max}	Q^2_{min} (GeV^2)	Q^2_{max} (GeV^2)
CTEQ6l	10^{-6}	1	1.69	10^8
MRST2004	10^{-5}	1	1.25	10^7

Table 5.1: Energy scale and Bjorken variable range of validity for each set of PDF .

5.1.2 b parton and b jets distributions

In this section I want to discuss if the discrepancies between transverse momentum or rapidity distributions of the b jets obtained with different PDF sets are due to the hadronization and reconstruction procedure or to the intrinsic differences in the treatment of b parton

density function between CTEQ and MRST collaborations. In the latter case we could use this difference to estimate the uncertainty on differential cross section measurements for the Z ($\mu\mu$) + b jet channel due to the b PDF. For this purpose I will show a comparison between distributions of true b quarks (identified from the Monte Carlo Truth) and reconstructed b-jets (tagged from the ATLFAST b tagging algorithm discussed in section 3.3.1).

In order to select the Z+b-jet signal I applied cuts both at parton level (on Monte Carlo Truth b partons) and at reconstruction level (on ATLFAST b-jets). I required al least one b parton/jet per event with transverse momentum $p_T > 15$ GeV, and inside the pseudorapity range $|\eta| < 2.5$. Motivations for these choice have been already discussed in section 5.2.1.

Figure 5.1 assures that detector effects do not modify the shape of p_T and rapidity distribution of the b jet. They have been obtained using the CTEQ6l PDF set, but same results can be obtained using MRST2004. All the plots are normalized to the number of entries.

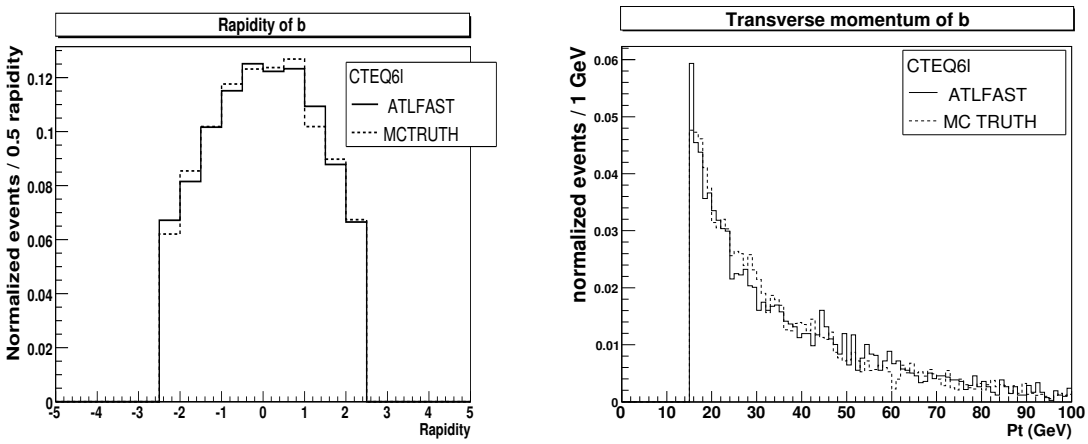

(a) (b)

Figure 5.1: Comparison between MC TRUTH and ATLFAST reconstruction of b distributions in Z+b events: η (a) and p_T (b) distributions of the b parton (MC TRUTH: dotted line) and jet (ATLFAST) .

The difference in transverse momentum and rapidity distributions of the b-jet using the two PDF sets is shown in fig. 5.2. The plots are normalized to 1 fb^{-1} of integrated luminosity. Only in the central rapity and low transverse momentum distributions we have

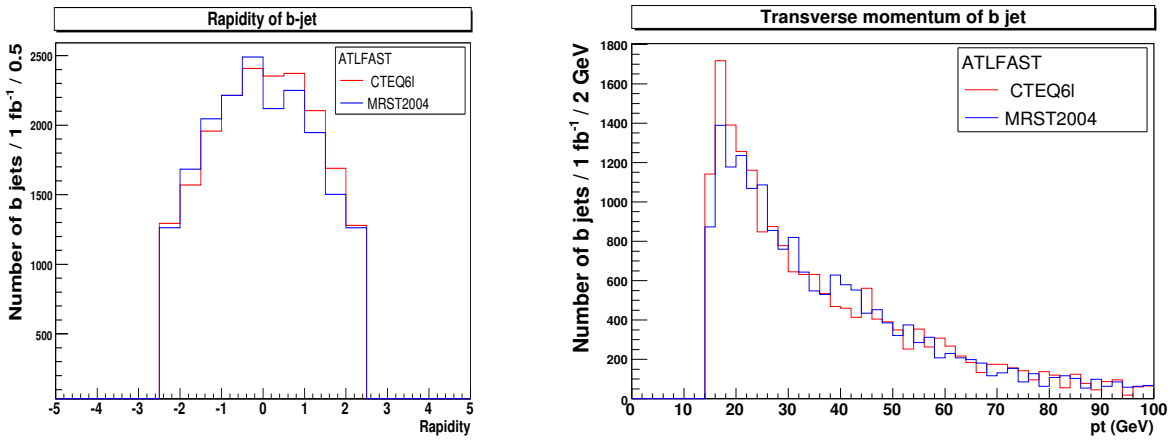

(a) (b)

Figure 5.2: (a) η distribution of the b-jets in Zb events (ATLFAST) (b) p_T distribution of the b-jets in Zb events (ATLFAST).

differences of $\approx 5\%$ between the two sets of PDF. Neverthless comparing these distributions with fig. 5.1 we can conclude that the only discrepancy that can be used to estimate the uncertainty on differential cross section measurements for the Z+b jet channel due to the b PDF is the one in the central rapidity region: this discrepancy is absent when we compare Monte Carlo true b quarks with ATLFAST reconstructed b-jets. This should mean that the discrepancy is not due to the hadronization or to the reconstruction procedure, but to a difference between the two PDF sets.
The same does not happen in the transverse momentum distributions: when we compare the Monte Carlo true b quarks and the ATLFAST reconstructed b-jets momentum distribution we see that it already presents a discrepancy in the low p_T region.
Anyway further studies including errors associated to the PDF should be done in order to give a more precise estimation of this discrepancy.

5.2 Studies of background from Z+c-jet

The measurement of the Z + b-jet cross section will be limited by systematic uncertainties and one important source of systematic uncertainty is related to the background due to c-jets that are misidentified as b-jets.
The identification of b-jets takes advantage of several of their properties which allow us to distinguish them from jets which contain only lighter quarks. First of all being the

fragmentation hard, the b-hadron retains about 70% of the original b quark momentum. Furthermore, the mass of b-hadrons is relatively high ($>$ 5 GeV), thus, their decay products have the opening angle of the decay products large enough to allow separation and a large transverse momentum with respect to the jet axis. The third property is the relatively long lifetime of hadrons containing a b quark, of the order of 1.5 ps ($c\tau \approx 450\mu$m). I remind here (see also sec. 3.2.2) that a b-hadron in a jet with $p_T = 10$ GeV will therefore have a significant flight path length $\langle l \rangle = \beta\gamma c\tau$, traveling on average about 1 mm before decaying. Such displaced vertices can first be identified inclusively by measuring the impact parameters of the tracks from the b-hadron decay products. As already mentioned in section 3.3.1, I remind that the transverse impact parameter, d_0, is the distance of closest approach of the track to the primary vertex point, in the $r - \varphi$ plane. The longitudinal impact parameter, z_0, is the z coordinate of the track at the point of closest approach in the beam line direction. The tracks from b-hadron decay products tend to have rather large impact parameters which can be distinguished from tracks stemming from the primary vertex. This approach will be referred to later on as *impact parameter b-tagging*.
Finally, the semi-leptonic decays of b-hadrons can be used by tagging the lepton in the jet. In addition, thanks to the hard fragmentation and high mass of b-hadrons, the lepton will have a large momentum relative to the jet axis. This is the so-called *soft lepton tagging* (the lepton being soft compared to high-p_T leptons from Z decays).

In this section I will discuss the behaviour of some variables that could be used to distinguish Z+b-jet from Z+c-jet events, with the goal of being able to measure both type of events. I am also going to show that, rather than cutting on the single variables, an alternative approach for the precise estimation of such background could be a Multivariate Analysis where selected variables are taken into account simultaneously by a complex algorithm (i.e. Neural Network, Likelihood Estimator, etc) to discriminate between signal and background. The description of these algorithms can be found in [53].
This study is motivated by the idea to find variables different from the ones used so far to construct the b tagging weight and to see if they can be combined in such a way to increase the purity of Z+b-jet sample, reducing the background from mistagged Z+c-jet events.

5.2.1 Simulated Data Sample and Event selection

All the samples have been generated with the PYTHIA Monte Carlo package [23]. The detector response has been simulated using the ATLFAST package [38].
In order to produce these samples I started from the official JobOption used by the Atlas collaboration to generate and fully simulate the pp $\rightarrow$ Z($\mu\mu$) inclusive channel [55].

The above JobOption has been modified to require the presence of at least one jet of a precise flavor associated to the Z boson in the final state and in order to be interfaced to the ATLFAST package. The contribution from virtual photon production (Drell-Yan) was switched off.

The following samples have been produced:

- pp $\rightarrow Z \rightarrow \mu\mu$ + b jet + X;
- pp $\rightarrow Z \rightarrow \mu\mu$ + c jet + X.

From now on I will not include the X letter in mentioning the samples, implying that each sample in the final state can contains other particles and jets produced in association to the leading process.
The above samples have been produced in two ways: first with only the hard process and subsequent fragmentation and conversion of partons into hadrons that can decay if they are not stable (but any initial or final state radiation (ISR, FSR) and underlying event (UE)) and second including also ISR, FSR and UE (for more details see sec. 3.1.1). For simplicity from now on I will refere to the first kind of samples as *only hard process* samples implying that hadronization and decay of unstable particles are always included. Pile up interactions coming from superposition of different events are not present in the produced samples.
The number of generated events, Pythia cross sections per samples and the corresponding integrated luminosity are reported in Table 5.2.

		Only hard process		**Hard process + ISR, FSR, UE**	
Process	**Events**	**Pythia Cross Section (pb)**	$\int Ldt$ (pb^{-1})	**Pythia Cross Section (pb)**	$\int Ldt$ (pb^{-1})
Z + b-jet	50K	40.03	1250	40.47	1235
Z + c-jet	50K	49.48	1010	49.41	1010

Table 5.2: Number of generated events, Pythia cross sections and integrated luminosity for generated samples.

The analysis has been perfomed using the informations stored into the ntuples, in particular the muons, the jets and the tracks blocks already defined in section 3.3.1.
The Cone 0.4 jet algorithm has been used for the jet reconstruction.
As it has been shown in the previous chapter cuts on muons and muon pair do not influence the distributions of jets, so in order not to loose statistic, I decided to cut only on

jets. I required at least one jet in the event with transverse momentum $p_T^{jet} > 15$ GeV and inside the rapidity range $|\eta^{jet}| < 2.5$.

In table 5.3 the number of events obtained after applying the selection cuts on the generated samples with only hard process is shown.

MC TRUTH (HARD PROCESS ONLY)			**ATLFAST (HARD PROCESS ONLY)**		
Cuts	**Z+ b-jet Events**	**Z+c-jet Events**	**Cuts**	**Z+b-jet Events**	**Z+c-jet Events**
at least 1 MC jet	43542	48332	at least 1 reco jet	31793	38388
$p_T^{jet} > 15$ GeV	28488	32146	$p_T^{jet} > 15$ GeV	24586	29689
$\|\eta^{jet}\| < 2.5$	23740	26953	$\|\eta^{jet}\| < 2.5$	20297	24565

Table 5.3: Number of events after cuts (only hard process).

In table 5.4 the number of events obtained after the selection cuts on the generated sample with also ISR, FSR and UE switched on is shown.

MC TRUTH (FULL PROCESS)			**ATLFAST (FULL PROCESS)**		
Cuts	**Z + b jet Events**	**Z + c jet Events**	**Cuts**	**Z + b jet Events**	**Z + c jet Events**
at least 1 MC jet	47858	49527	at least 1 reco jet	37895	43961
$p_T^{jet} > 15$ GeV	34160	39569	$p_T^{jet} > 15$ GeV	28647	35368
$\|\eta^{jet}\| < 2.5$	30080	35408	$\|\eta^{jet}\| < 2.5$	24598	30963

Table 5.4: Number of events after cuts (ISR, FSR and UE switched on).

For the selected events the following variables have been studied:

- invariant mass of charged tracks in the jet;
- maximum impact parameter among the charged tracks in the jet;
- relative transverse momentum between the jet axis and the candidate muon from b or c decay.

In section 5.2.2 the results obtained using only the first two of these variables will be discussed. In section 5.2.3 also the relative transverse momentum will be added to perform the analysis.

Multivariate Analysis

In the following sections the preliminary results obtained analyzing the variables described above with the Toolkit for Multivariate Analysis (TMVA) [53] will be shown.
The analysis proceeds by first choosing variables that can help in distinguishing signal from background events. For each variable, statistical properties like mean, variable ranges are computed to search for optimal cuts. Cut optimisation requires an estimator that quantifies the goodness of a given cut ensemble. TMVA provides a ROOT [54] integrated environment for the evaluation of multivariate classification techniques (classifiers) and the user can choose between a whole set of such classifiers. Maximising this estimator minimises (maximises) the background efficiency, ε_B (background rejection, $r_B = 1 - \varepsilon_B$) for each signal efficiency ε_S.
The main advantage in using a Multivariate Analysis is essentially because it does not apply cuts on variables in sequence, but it makes a combination of chosen variables in order not to reduce the initial sample (like we do when we cut sequentially) and to enhance efficiency on signal selection and backgroud rejection. TMVA is widely used in High Energy Physics.
For this first exercise I have used the following three classifiers: Fisher Discriminant, Multi Layer Perceptron (MLP) Neural Network and Likelihood Estimator.

The Likelihood Estimator consists of building a model of probability density functions that reproduces the input variables for signal and background. For a given event, the likelihood for being of signal type is obtained by multiplying the signal probability densities of all input variables, and normalising this by the sum of the signal and background likelihoods. Correlations among the variables are ignored.
The Fisher Discriminant event selection is performed in a transformed variable space with zero linear correlations, by distinguishing the mean values of the signal and background distributions. No discrimination at all is achieved when a variable has the same sample mean for signal and background, even if the shapes of the distributions are very different.
The Multi Layer Perceptron organizes the neurons in layers and only allowing directional connections from one layer to the immediate next one. Each directional connection between the output of one neuron and the input of another has an associated weight. The value of the output neuron is multiplied with the weight to be used as input value for the next neuron.

A typical TMVA analysis consists of two indipendent phases:

- the training phase, where the multivariate classifiers are trained, tested and evaluated, using two separate input data files: one for the signal and one for the background;

- the application phase, where the trained classifiers are applied to the classification problem implemented by the user in the analysis, using a more realistic input data file with a mixture of signal and background events.

So far only the training phase has been implemented in this analysis. Work is in progress to implement also the application phase.

The Multivariate Analysis has been performed on the samples with ISR, FSR and UE switched off, in order to have a better control on the variables.

5.2.2 Impact parameter and invariant mass tracks b-tagging

Several techniques can be adopted to determine the heavy flavor content of a jet in order to extract the fraction of b jets. Here I will focus on the two possible discriminating variables:

- *mass_tracks*: invariant mass of all the charged tracks inside a cone $\Delta R = 0.4$ around the jet axis;
- $d0max$: maximum impact parameter among all the charged tracks inside a cone $\Delta R = 0.4$ around the jet axis.

Due to the presence of neutral particles that do not leave tracks in the Inner Detectora full reconstruction of the invariant mass is not possible. Still the invariant mass of charged tracks can constitute a good discrimination between jets containing b and c quarks.
Figure 5.3 shows the invariant mass of all the charged tracks inside a bottom and charm jet in Z+b/c jet events in the case of the only hard process (a) and when also ISR, FSR and UE were switched on (b). What we can conclude from this figure is that in order to discriminate between the two different flavors of the jets we can cut on this variable, as it will be shown in the following. For future analysis a better use of this variable could be to fit the shape of the distributions since they look different between bottom and charm jets.

Another good discriminating variable between b and c quarks is the impact parameter itself: as already discussed I expect to have a greater impact parameter for the b-hadrons events with respect to c-hadrons, mainly due to the longer life time of hadrons containing b quarks respect to hadrons containing c quarks. This is confirmed by the fig. 5.4 where the d0max ditribution for tracks coming from bottom or charm jets in Z+b/c jet are shown.

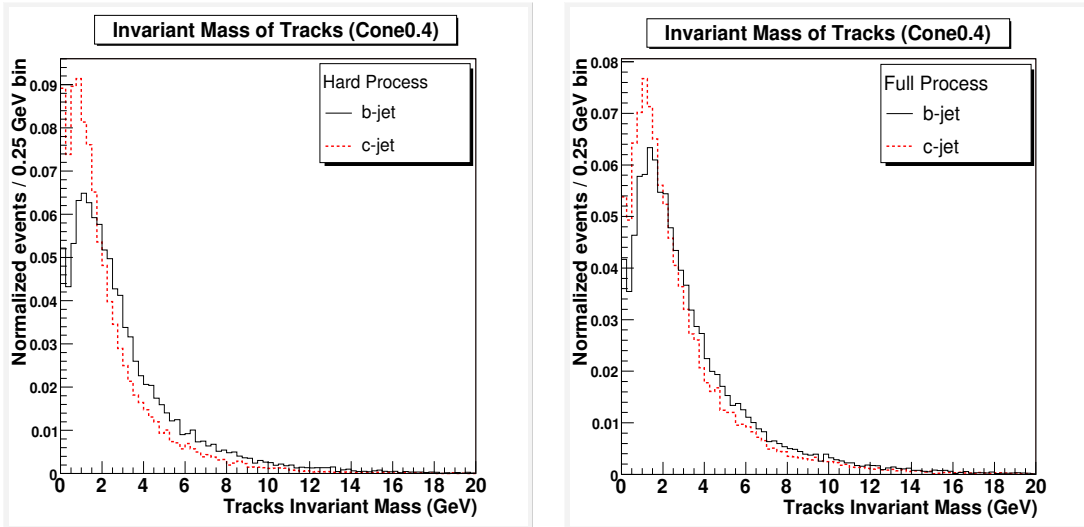

(a) (b)

Figure 5.3: The invariant mass of the charged tracks in a cone of $\Delta R = 0.4$ respectively for only hard process (a) and full process (b) for Z+b jet (black) and Z+c jet (red) events. Histograms are normalized to the number of entries.

In order to show the effect of different cuts on the invariant mass of charged tracks (*mass_tracks*) and on the maximum impact parameter (*d0max*), I define the *efficiency* in selecting $Z \to \mu\mu$ + b jet (5.1):

$$\varepsilon = \frac{N_b}{S} \tag{5.1}$$

where (N_b) is the number of Z+ b-jet events (signal) after cuts on jets and on different values of the chosen parameter, while S is the number of signal events after only the cuts on jets.

I define for the background the *rejection* factor r for $Z \to \mu\mu$ + c jet events (5.2):

$$r = 1 - \frac{N_c}{B} \tag{5.2}$$

where (N_c) is the number of Z+c-jet background events after cuts on jets and on different values of the chosen parameter, while B is the number of background events after only the cuts on jets.

Errors associated to *efficiency* and *rejection* have been calculated propagating errors on

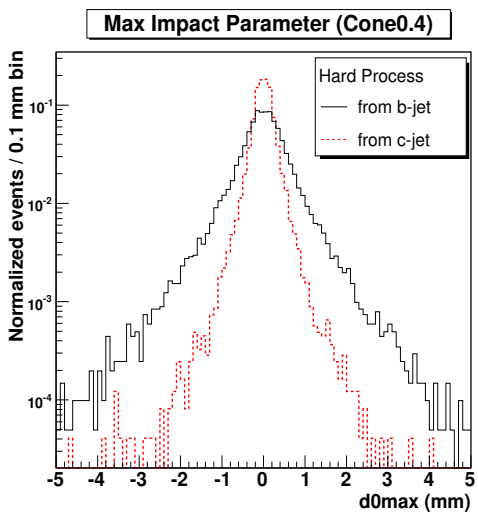

(a)

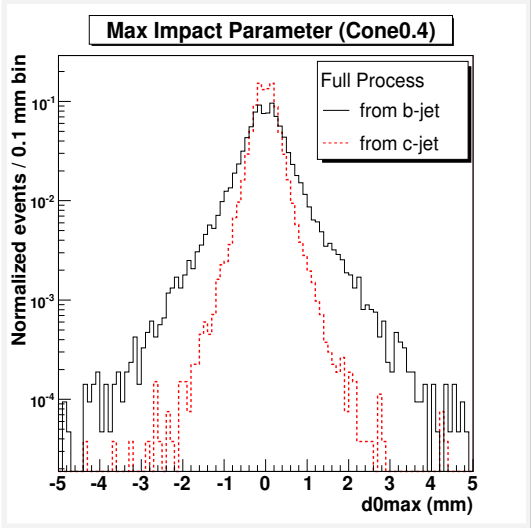

(b)

Figure 5.4: The maximum impact parameter among the charged tracks in a cone of $\Delta R = 0.4$ respectively for only hard process (a) and full process (b) for Z+b jet (black) and Z+c jet (red) events. Histograms are normalized to the number of entries.

the number of selected events (for example $\delta N_b = \sqrt{N_b}$).

The following results are obtanined from the sample of 50K events with only the hard process switched on. Table 5.5 shows efficiency and rejection factor obtained for different cuts on $d0max$ value.

cuts on $\lvert d0max \rvert$	Efficiency Z+b	Rejection Z+c
no cuts	1.00 ± 0.01	
> 1 mm	0.83 ± 0.01	0.36 ± 0.01
> 2 mm	0.66 ± 0.01	0.67 ± 0.01
> 3 mm	0.52 ± 0.01	0.81 ± 0.02
> 4 mm	0.41 ± 0.01	0.89 ± 0.02
> 5 mm	0.33 ± 0.01	0.93 ± 0.03

Table 5.5: Efficiency and rejection factor when cutting on d0max.

Table 5.6 shows efficiency and rejection factor obtained for different cuts on *mass_tracks* value.

cuts on *mass_tracks*	Efficiency Z+b	Rejection Z+c
no cuts	1.00 ± 0.01	
> 0.5 GeV	0.90 ± 0.01	0.16 ± 0.01
> 1 GeV	0.80 ± 0.01	0.34 ± 0.01
> 2 GeV	0.54 ± 0.01	0.62 ± 0.01
> 3 GeV	0.36 ± 0.01	0.77 ± 0.01
> 4 GeV	0.24 ± 0.01	0.85 ± 0.02
> 5 GeV	0.17 ± 0.01	0.90 ± 0.02
> 6 GeV	0.12 ± 0.01	0.93 ± 0.03

Table 5.6: Efficiency and rejection factor when cutting on *mass_tracks*.

The table 5.7 shows efficiency and rejection factor obtained combining cuts on both *d0max* and *mass_tracks*.

After the analysis on the single parameters cuts and on the combination of them, I can define some ranges of values where the efficiency and the purity of the selected events are quite good. For the $|d0max|$ parameter, the range is defined as $1 \leq |d0max| \leq 3$ mm and for the *mass_tracks*, the range is defined as $0.5 \leq mass\_tracks \leq 1.0$ GeV. Using these cuts I can achieve an efficiency of about 60% and a rejection factor of about 65-70%.

Results from Multivariate Analysis

The same two variables used above, can be used as the input variables to train the three TMVA classifiers. The distributions of the input variables for signal and background are shown in figure 5.5.

It is useful to quantify the correlations between the input variables. These are drawn in form of a correlation matrix in figure 5.6.

The resulting relations between background rejection versus signal efficiency are shown in figure 5.7 for the three classifiers.

Looking at the rejection background versus efficiency signal plot (fig. 5.7) it is clear that the Likehood Estimator is the best discriminating method with an efficiency of $\approx$ 70% with a background rejection factor of $\approx$ 60%. The motivation can be explained if we

cuts on 2 variables	Efficiency Z+b	Rejection Z+c
$mass\_tracks > 0.5$ GeV & $\lvert d0max \rvert > 1$ mm	0.78 ± 0.01	0.43 ± 0.01
$mass\_tracks > 0.5$ GeV & $\lvert d0max \rvert > 2$ mm	0.63 ± 0.01	0.69 ± 0.01
$mass\_tracks > 0.5$ GeV & $\lvert d0max \rvert > 3$ mm	0.50 ± 0.01	0.83 ± 0.02
$mass\_tracks > 1$ GeV & $\lvert d0max \rvert > 1$ mm	0.70 ± 0.01	0.53 ± 0.01
$mass\_tracks > 1$ GeV & $\lvert d0max \rvert > 2$ mm	0.57 ± 0.01	0.75 ± 0.01
$mass\_tracks > 1$ GeV & $\lvert d0max \rvert > 3$ mm	0.45 ± 0.01	0.86 ± 0.02

Table 5.7: Efficiency and rejection factor when cutting both on d0max and on $mass\_tracks$.

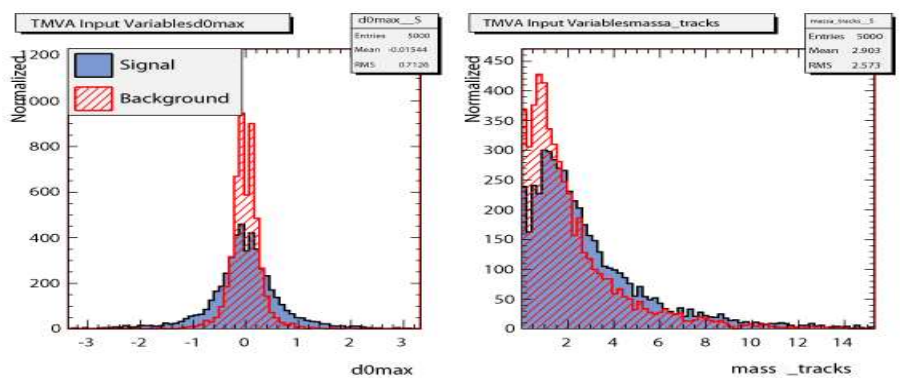

Figure 5.5: Input variable distributions to train the TMVA classifiers.

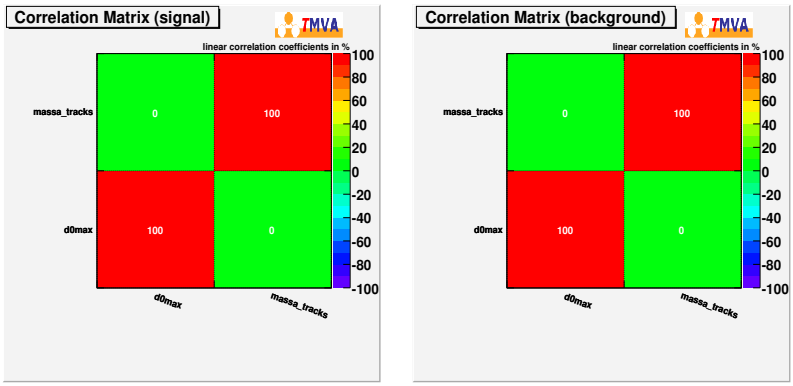

(a) (b)

Figure 5.6: Correlation between input variables: linear correlation coefficients for the signal (a) and background (b) training samples.

consider that in the Likelihood Estimator method the event selection is essentially done fitting the histograms of input variables, while in the method of Fisher Discriminant the event selection is performed by distinguishing the mean values of the signal and background distributions. No discrimination is achieved when a variable has the same sample mean for signal and background, even if the shapes of the distributions are very different: as it can be seen in fig.5.5, this is the case of the $d0max$ parameter.

A comparable result can be also achieved if we cut on $|d0max| > 1$ mm and $mass\_tracks >$ 1 GeV (see table 5.7), but the advantage in using a Multivariate Analysis is that we do not loose statistics cutting on variables. Neverthless, if we want to reach a better value for rejection in order to have sample with a small background, it is convenient to find additional discriminating variables to introduce in the Multivariate Analysis. This is what I am going to show in the next section.

5.2.3 Soft muon b-tagging

I now want to exploit the features of the events which contain a muon from b or c decay. The branching fraction of a b or c jets into leptons is $\approx 10\%$ [1]. In spite of the poorer statistics, the sample containing a muon has a very clean signature of a high p_T muon at large angle with respect to the jet axis. In the following I will refer to these muons as *non isolated* muons, to distinguish them from the isolated muons from Z decay.

The analysis has been done comparing statistics and distributions obtained from the truth Monte Carlo informations (called from now on *MC TRUTH*), with those obtained

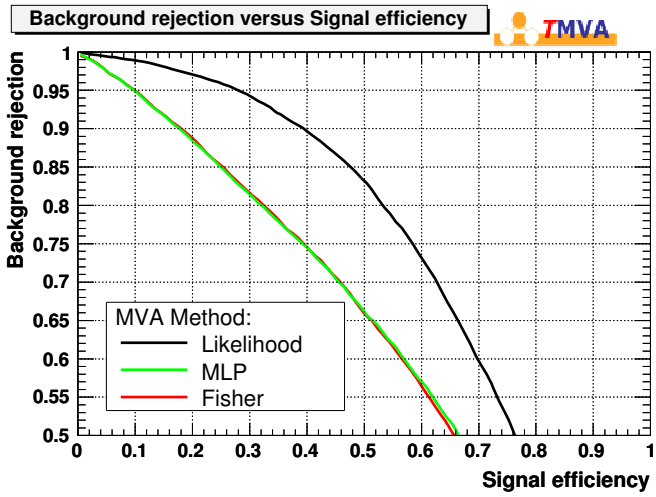

Figure 5.7: Background rejection versus signal efficiency obtained by cutting on the classifier outputs for the events of the test sample.

with the fast simulation (labelled as *ATLFAST*).

Since Monte Carlo jets are built from the truth particles, at the truth level it is possible to distinguish among three different categories:

- muons that come directly from a B hadron inside a b jet ,
- muons that come from a D hadron that has been produced through the decay of a B hadron inside a b jet ,
- muons that come from a D hadron inside a c jet .

The Z + b jet sample contains the first two categories, while the Z + c jet sample contains only the third category.
I remind that in ATLFAST the jet is labelled as b (c) if a b quark (c quark) with a p_T above 6 GeV, in a pseudorapidity range $|\eta| < 2.5$, lying in a cone of $\Delta R < 0.3$ is found. If not, it is labelled as a light jet (see section 3.3.1). ATLFAST variables do not allow to separate muons that come directly from a D hadron inside a c jet and muon from a D hadron produced after the decay of a B hadron inside a b jet (at parton level this is equivalent to the decay $b \to c$). This explains why there are more b jet events in the ATLFAST sample compared to what I should expect from MC truth.

To select a non isolated muon and to distinguish it from the muons from the Z boson, (after requirements on these muons), I asked for:

- $p_T^{\mu} < 20$ GeV
- $\Delta R_{\mu-jet} < 0.4$
- $M_{\mu\mu} < 70$ GeV

where $M_{\mu\mu}$ is the invariant mass in case more than two muons are present in the event. These cuts are complementary to the ones used to select isolated muons from the Z decay (see section 4.3.1).

Tables 5.8 and 5.9 show the composition on the final samples after all the cuts just described.

MC TRUTH			**ATLFAST**	
Z+b	**Z+b→c**	**Z+c**	**Z+b**	**Z+c**
495	735	769	1055	645

Table 5.8: Number of events with a third muon (only hard process switched on).

MC TRUTH			**ATLFAST**	
Z+b	**Z+b→c**	**Z+c**	**Z+b**	**Z+c**
628	925	1114	1974	1396

Table 5.9: Number of events with a third muon (ISR, FSR and UE switched on).

Figure 5.8 shows the muon transverse momentum from true b and c jets (from MC Truth information) in the only hard process sample (a) and when also ISR, FSR, UE have been switched on (b).

Figures 5.9 (a) and (b) show the angular distance between muon and true jets obtained using MC truth variables respectively for sample with only hard process and with also ISR,FSR and UE switched on. Figures 5.9 (c) and (d) show the same $\Delta R_{\mu-jet}$ distribution obtained from the ATLFAST reconstructed variables. The plots in figure 5.9 (a) and 5.9 (b) have been obtained requiring $p_T^{\mu} > 6$ GeV and $|\eta^{\mu}| < 2.5$, namely the same cuts used in ATLFAST for muon reconstruction (see section 3.3.1).

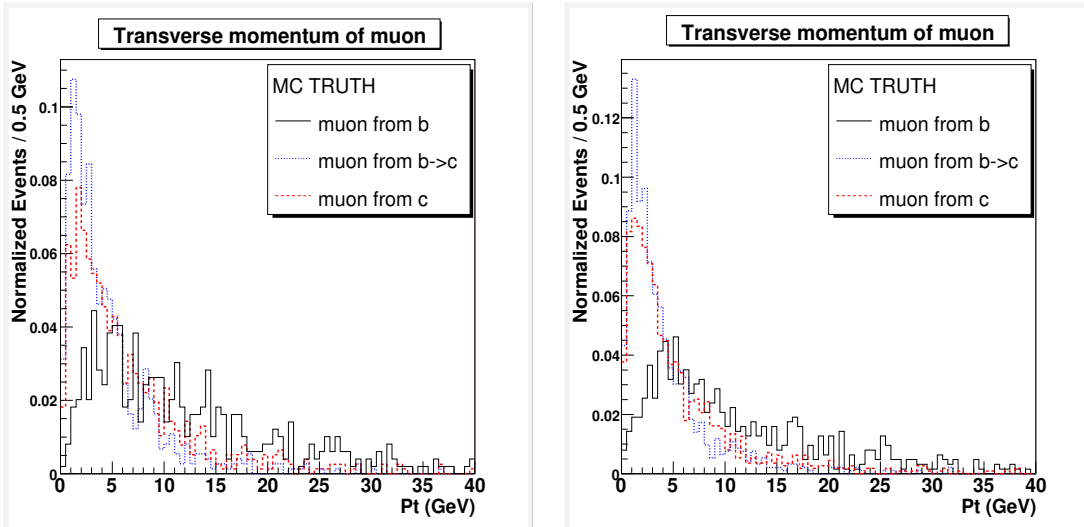

(a) (b)

Figure 5.8: Transverse momentum of muon from true b and c jets in MC samples with only hard process (a) and with also ISR, FSR, UE switched on (b).

Relative transverse momentum between muon and jet axis

To the two discriminating variables used in the analysis discussed in sez. 5.2.2, another possible discriminating variable can be added when a beauty or charm quark decay into a muon: the relative transverse momentum between the muon and the jet axis . It is defined as:

$$p_T^{Rel} = |\vec{p_\mu}| \sin(\arccos(\frac{\vec{p_\mu} \cdot \vec{p_{jet}}}{|\vec{p_\mu}||\vec{p_{jet}}|})) \tag{5.3}$$

A schematic draft of p_T^{Rel} is shown in figure 5.10.

Due to the bigger mass of the b quark, muons from b jets show to have a p_T^{Rel} value greater than muons from c jets, as it is shown in the plots in fig. 5.11 for both Monte Carlo truth and ATLFAST.

For this analysis three variables were used to discriminate Z+b jet from Z+c jet events:

- $ptrel$: relative transverse momentum between muon and jet,
- $mass\_tracks$: invariant mass of all the charged tracks inside a cone $\Delta R = 0.4$ from the jet axis ,

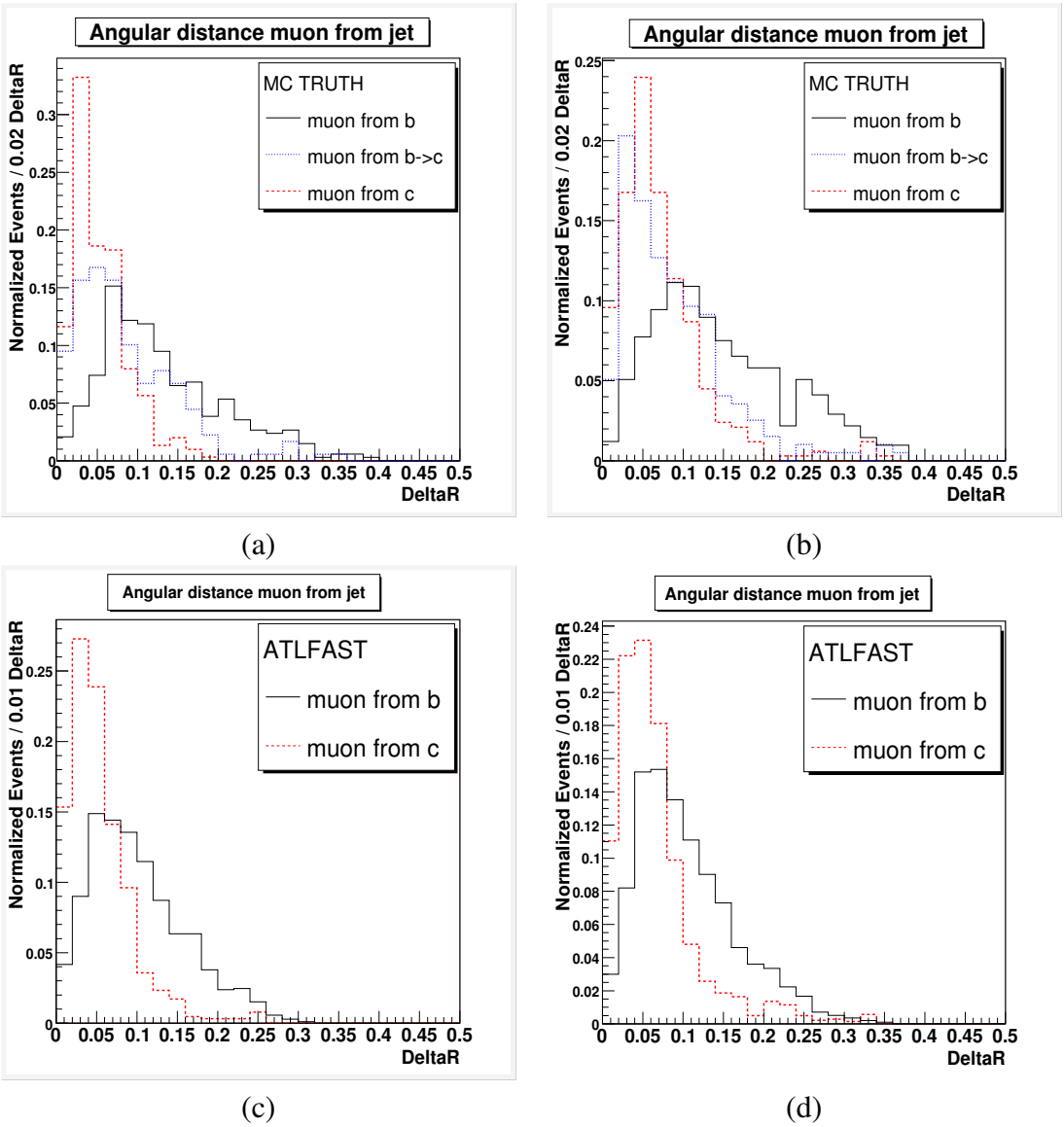

Figure 5.9: Angular distance between muon and MC jet in the sample with only hard process (a) and with also ISR, FSR, UE switched on (b). Angular distance between muon and ATLFAST reconstructed jet in the sample with only hard process (c) and with also ISR, FSR, UE switched on (d).

- $d0max$: maximum impact parameter among all the charged tracks inside a cone $\Delta R = 0.4$ from the jet axis.

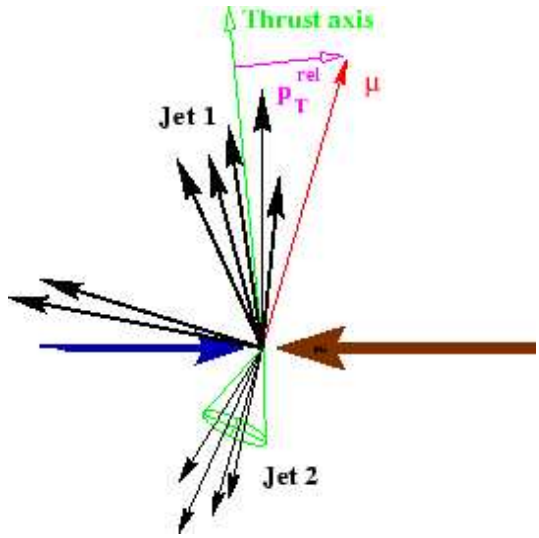

Figure 5.10: Relative momentum (p_T^{Rel}) of muon respect to the jet axis.

Efficiency and rejection as a function of cuts on single variables, are shown in fig. 5.12.

The table 5.10 shows efficiency and rejection factor obtained combining cuts on two variables among p_T^{Rel}, $d0max$ and $mass\_tracks$, while the table 5.11 is obtained combining cuts on all the three parameters.

Summarizing the results, I can obtain a good efficiency of $\approx 70\%$ and purity of $\approx 80\%$ when cutting in the following ranges: $1 \leq |d0max| \leq 3$ mm , $1.0 \leq mass\_tracks \leq 2.0$ GeV and $0.5 \leq p_T^{Rel} \leq 1.0$ GeV.

Results from Multivariate Analysis

The variables used to train the three classifiers are the ones described above.

Since only a fraction of $\approx$ 10 % of beauty and charm quark decay into muons, if I require the precence of at least one non isolated muon (definied as in section 5.2.3), the sample will be reduced to a factor $\approx$ 4-6 % of the initial sample. Due to a non sufficient sample of simulated data, for this analysis I increased the statistics of the initial data samples to 350k events (hard process only).

The distributions of the input variables for signal and background are shown in figure 5.13.

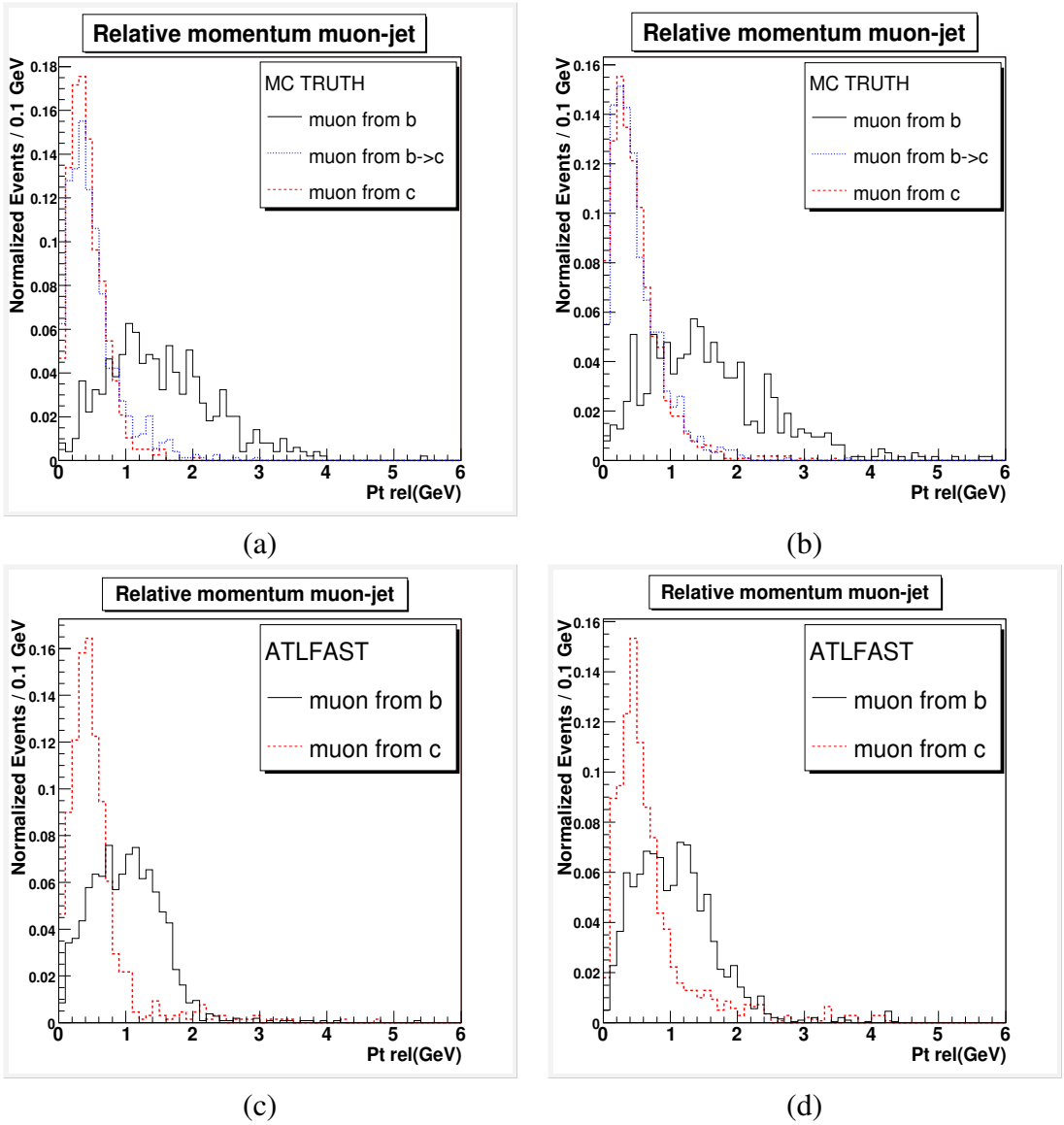

Figure 5.11: p_T^{Rel} between muon and MC true jet in the sample with only hard process (a) and with also ISR, FSR, UE switched on (b). p_T^{Rel} between muon and ATLFAST reconstructed jet in the sample with only hard process (c) and with also ISR, FSR, UE switched on (d).

Figure 5.14 shows the correlations between the input variables.

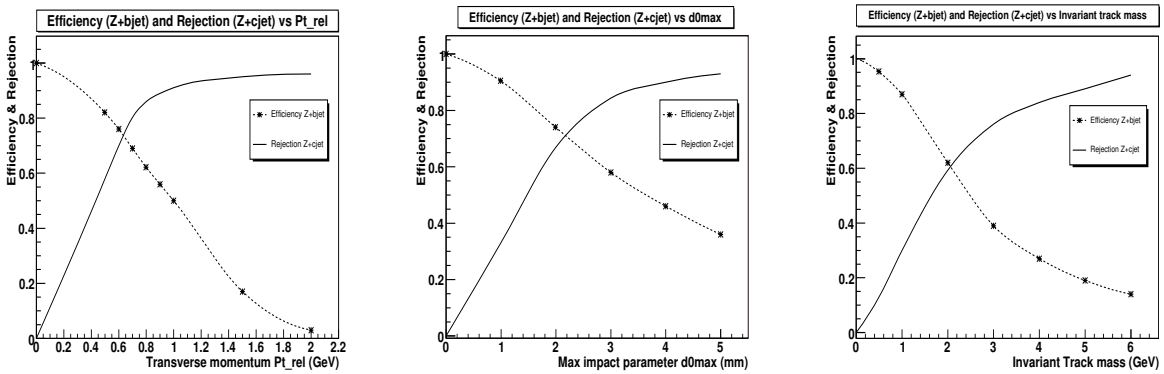

(a) (b) (c)

Figure 5.12: Efficiency and rejection after applying cuts on relative tranverse momentum between muon and jet (p_T^{Rel}) (a), on the maximum impact parameter among all tracks inside the jet ($d0max$) (b) and on the invariant mass of all tracks inside the jet ($mass\_tracks$) (c).

cuts on 2 variables	**Efficiency Z+b**	**Rejection Z+c**
$p_T^{Rel} > 0.5$ GeV & $\lvert d0max \rvert > 1$ mm	0.73 ± 0.05	0.73 ± 0.08
$p_T^{Rel} > 0.5$ GeV & $\lvert d0max \rvert > 2$ mm	0.60 ± 0.04	0.86 ± 0.12
$p_T^{Rel} > 0.5$ GeV & $\lvert d0max \rvert > 3$ mm	0.46 ± 0.03	0.94 ± 0.20
$p_T^{Rel} > 1$ GeV & $\lvert d0max \rvert > 1$ mm	0.44 ± 0.04	0.95 ± 0.20
$p_T^{Rel} > 1$ GeV & $mass\_tracks > 1$ GeV	0.72 ± 0.03	0.68 ± 0.07

Table 5.10: Efficiency and rejection factor when cutting on p_T^{Rel} and $d0max$.

cuts on 3 variables	**Efficiency Z+b**	**Rejection Z+c**
$p_T^{Rel} > 0.5$ GeV & $mass\_tracks > 0.5$ GeV & $\|d0max\| > 1$ mm	0.71 ± 0.05	0.74 ± 0.09
$p_T^{Rel} > 0.5$ GeV & $mass\_tracks > 1$ GeV & $\|d0max\| > 1$ mm	0.66 ± 0.04	0.77 ± 0.09
$p_T^{Rel} > 0.5$ GeV & $mass\_tracks > 2$ GeV & $\|d0max\| > 1$ mm	0.49 ± 0.04	0.85 ± 0.12
$p_T^{Rel} > 0.5$ GeV & $mass\_tracks > 3$ GeV $\|d0max\| > 1$ mm	0.32 ± 0.03	0.90 ± 0.15
$p_T^{Rel} > 0.5$ GeV & $mass\_tracks > 2$ GeV & $\|d0max\| > 2$ mm	0.41 ± 0.03	0.90 ± 0.15
$p_T^{Rel} > 0.5$ GeV & $mass\_tracks > 0.5$ GeV & $\|d0max\| > 3$ mm	0.45 ± 0.03	0.94 ± 0.19
$p_T^{Rel} > 0.5$ GeV & $mass\_tracks > 1$ GeV & $\|d0max\| > 2$ mm	0.55 ± 0.04	0.87 ± 0.13

Table 5.11: Efficiency and rejection factor when cutting on p_T^{Rel}, $mass\_tracks$ and $d0max$.

Figure 5.15 shows the classifier output distributions for signal and background events from the test sample. By TMVA convention, signal (background) events accumulate at large (small) classifier output values. Hence, cutting on the classifier output, I can select the signal sample with efficiencies and purities that respectively decrease and increase with the cut value. The resulting relations between background rejection versus signal efficiency are shown in figure 5.16 for all classifiers that were used in this work.

By a preliminary glance at the plots of figure 5.15, it is possible to see that the Likehood Estimator is the best discriminating method, also if respect to the previous study with only two variables, in this case the difference among all methods is not that appreciable. This result depends on how the three methods are built, as already discussed in sec.5.2.2.

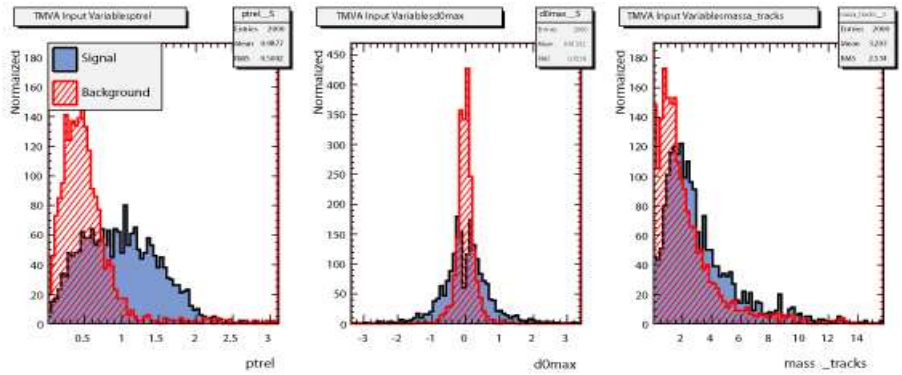

Figure 5.13: Input variable distributions to train the TMVA classifiers.

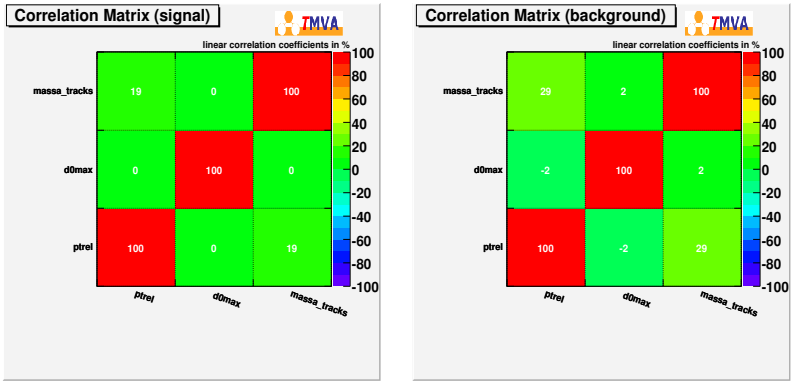

(a) (b)

Figure 5.14: Correlation between input variables: linear correlation coefficients for the signal (a) and background (b) training samples.

In the future the combined use of those methods and the comparison among results obtained with different techniques can provide a powerful tool to control the systematics. Templates must be constructed from the best possible signal and background models. Other systematic effects on cross section meausurement will be discussed in the next chapter.

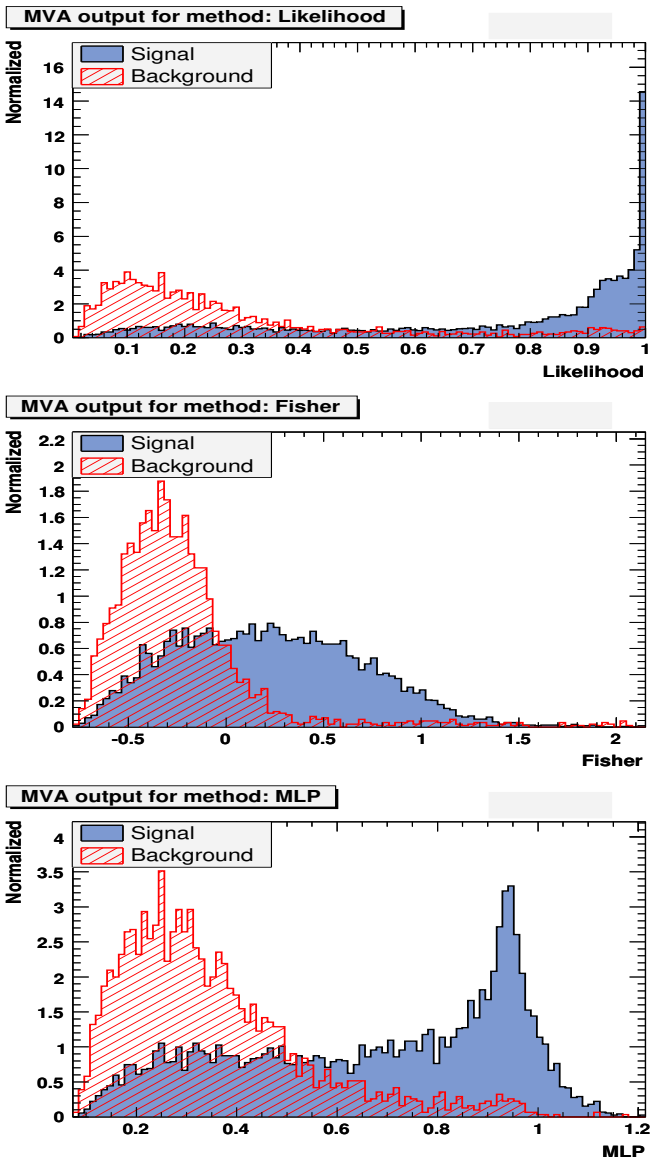

Figure 5.15: Classifier output distributions for signal and background events from the test sample. Likelihood Estimator (upper plot), Fisher Discriminant (middle plot) and MLP-NeuralNet (bottom plot) are shown.

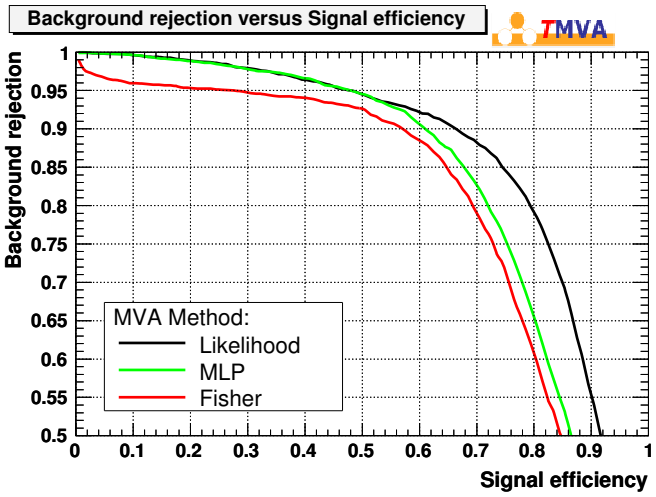

Figure 5.16: Background rejection versus signal efficiency obtained by cutting on the classifier outputs for the events of the test sample.

Chapter 6

Systematics Uncertainties

The uncertainties on cross section measurement due to systematic effects have been neglected in the analysis discussed in the previous chapters. Here I briefly discuss the major contributors to the systematic uncertainty on Z $\rightarrow \mu\mu$ + b jet cross section measurement.

The primary concern arises from the determination of jet energy scale and estimation of b-tagging efficiency and rejection, which may alter the sample composition significantly. One of the main theoretical uncertainties originates from the uncertainty on the parton content of the proton (PDF) that affect calculation of signal and background cross sections.

6.1 Jet Energy scale

Errors due to a miscalibration of the jet energy scale (JES) are expected to be one of the dominant systematics for the determination of Z ($\mu\mu$) + b jet cross-section.
The evaluation of JES uncertainty was done for the Z/W + jets channels [43, 63], in first approximation we can consider that the obtained results do not change much when we replace a light jet with a b jet.

If the energy is miscalibrated by a positive correction, more jets pass the selection cut and therefore there will be more high multiplicity events and viceversa when the energy is miscalibrated by a negative correction.
Figure 6.1 shows the relative systematic error on the ratio between measurement and theory for the inclusive Z (e^+e^-) + jets cross section (a) and for the transverse momentum of the leading jet (b) expected for different uncertainties on the Jet Energy Scale. Ratio of 1 correspond not to have systematic uncertainties.

ATLAS expects a limited precision on the jet energy scale in the first years, starting from uncertainties at the level of 10% and converging eventually towards 1% : 1% corresponding to the experiment challenging goal, 3% turn-on expected value, 10% for the worst case. If 3% error on JES is achived in early data, the systematic uncertainty on the inclusive cross section is at the same level as the sum of all the other statistical and systematic uncertainties. In this case, the overall precision on the data/theory ratio expected with the first fb^{-1} of data is at the level of 8-15% for topologie with 1-3 jets.
In the worst scenario, a jet energy scale uncertainty of 10% results in the dominant error on the cross section. In this case, the total uncertainty on the cross section is at the level of 15-30%. But, if it is achieved the challenging uncertainty in JES of 1%, systematic errors decreases to less than 0.5 %.

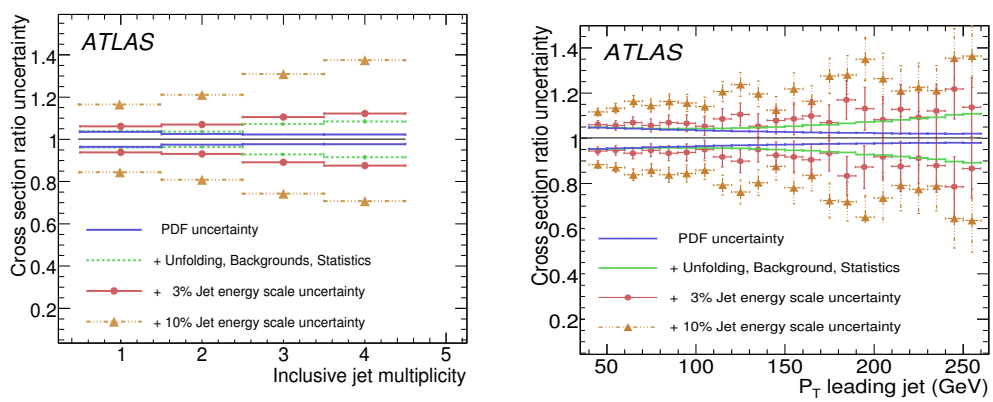

(a) (b)

Figure 6.1: Uncertainty on the ratio of measurement and theory for the inclusive jet cross-section (a) and the p_T, of the leading jet (b) for the $Z \to e^+e^- + jets$, process [43].

6.2 PDF

An important source of theoretical systematic uncertainties on cross sections measurements at the LHC is represented by the Parton Distribution Functions (PDF). In the last years the PDF's knowledge has largely improved mainly thanks to HERA [58]. This improvement reduces the error on the Z + jets cross section calculations: each PDFs group now quotes uncertainties lower than 5%. The effect of such uncertainty on the on the ratio of measurement and theory for the inclusive Z (e^+e^-) + jets cross section and and for the

transverse momentum of the leading jet, has been shown in figure 6.1. We can conclude that it becomes less important respect to other systematic effects with the increasing of jets multiplicity and/or of the transverse momentum of the leading jet. Neverthless the estimation of above was realized using the CTEQ5 pdf set, using different sets it has been shown that they are in agreement within an error of $\sim 8\%$ [59, 60].

Since at leading order the Z + b jet production can have origin from the interaction of a gluon and a b quark and because up to now the knowledge on the b content of the proton is less precise respect to the light quarks that can give origin to the Z + jets process [9], we expect that the error on the cross section measurement due to the PDF uncertainty will increase of a few percent respect to the one quoted for the inclusive Z+jets channel.

6.3 b-tagging algorithm

Vertex tagging of jets requires fine tuning of the inner detector performance. Determination of the b-tagging efficiency requires careful study of control samples. The b-tagging performance has been studied for several physics channels considering different tagging algorithms [45].
The contributions to the b tagging uncertainties have different origins: they come from the impact of the tracker material on performance, the sensitivity to the calibration of tagging algorithms, the impact of the pixel detector conditions, the sensitivity to the Monte Carlo modelling. The overall impact is expected to be a 10-15% relative change in light jet rejection power. The impact on b tagging performance due to each contribution is discussed in detail in [45].

In section 4.5 I discussed a strategy to measure the mistagging rate directly from data using the $W \to \mu\nu$ inclusive sample that does not contain b-jet at the first order in perturbartion theory. The result is that this method allows to keep the mistagging below a value of 5% for the gauge boson transverse momentum of $\lesssim 100$ GeV. So far no study in ATLAS has estimated the accuracy with which fake rates can be measured. However, based on the Tevatron experience, it seems that a 10% relative error could be achievable with 100 pb^{-1}.

Conclusions

The production of a Z boson together with jets containing heavy-quarks (c, b) is an important signal at the hadron colliders. In this analysis I have presented a feasibility study of the production of Z bosons decaying to muons in association with b-jets performed with a set of simulated signal and background Monte Carlo samples corresponding to an integrated luminosity of $1\,\mathrm{fb}^{-1}$.

This channel will serve as one of the Standard Model benchmarks for physics analyses as well as Beyond Standard Model signals. Furthermore, it represents a clear and high statistics channel to perform studies on the b parton content of the proton (PDF). The precise measurement of Z + b jet cross section will help in reducing the current uncertainty on the partonic content of the proton. Such uncertainty is presently affecting the potential for discovering new physics at LHC.
In order to measure the cross section when the experiment will start to take data, we need to have a good control of the possible background and of the principal sources of systematic uncertainties. The main aim of this work has been to develop analysis techniques in order to evaluate the contamination of the signal from backgrounds and to study possible methods to extract signal from such backgrounds.

$Z \to \mu\mu$ + b jet events suffer from two different kind of backgrounds. The first consists of events not containing a Z that decay into a muon pair, but involving muons in the final state that pass the isolation criteria appearing as muons from Z boson. In association to muons at least one jet is reconstructed and identified as a beauty jet. These events are: $t\bar{t}$ events involving at least one semileptonic decay in muon, $Z \to \tau\tau$ events with subsequent τ decay into muon, $W \to \mu\nu$ with a second muon coming from a jet or a second fake muon and QCD multi-jet events filtered to favour the presence of real muons or hadrons misidentified as muons ($b\bar{b}$ events). The second originates from events containing a Z boson decaying into a muon pair (as the signal), but with a c or light jet mis-identified as a beauty jet. These are Z ($\mu\mu$) + c/light jet events. It has been shown that the former, except QCD ($b\bar{b}$) jets production, can be reliably estimated from current Monte Carlo

predictions, although in situ verification with data will be needed. $b\bar{b}$ background dealing with rare fluctuations of large cross section processes can only be crudely estimated from current Monte Carlo simulation. With the selection cuts used in the analysis presented in this work we expect to select the signal events with an efficiency of of $\sim 40\%$ for an integrated luminosity of $1\,\mathrm{fb}^{-1}$, corresponding to a few months of running at moderate luminosity ($0.3\ nb^{-1}s^{-1}$). The dominant contribute to the background comes from jets production in QCD processes ($b\bar{b}$). The backgrounds from $t\bar{t}$,Z $\rightarrow \tau\tau$, $W \rightarrow \mu\nu$ and Z + light jet are negligible, while the contamination from Z + c jet should be of the order of $10-30\%$. The main limitation to the background estimation comes from the limited statistic of the available Monte Carlo samples, especially the QCD ($b\bar{b}$) sample: after selection cuts only a few events remain and the statistical error is really big. In order to better estimate the contamination of the signal due to this background further studies are required with larger MC samples. Neverthless, I showed that it is possible to reduce the percentage from this background optimizing cuts on the variables and exploiting different methods to distinguish signal from background (like fit on the di-muon pair invariant mass). In addition, Tevatron experience [?, 46] make us confident that real data will help in improving the discrimination between signal and QCD ($b\bar{b}$) jets background. In such scenario one of the main backgrounds to be reduced is from Z + c jet events where the c is mistagged as a b jet.

The second part of this work concerned the study of a strategy to reduce this background reducing the mistagging rate of c jets. Two different methods for tagging of b jets have been considered, which allow for the selection of samples with different levels of efficiency and purity: the first is based on the impact parameter of tracks associated to the jet and on the invariant mass of these tracks, the second includes also the transverse relative momentum between muon and jet for events containing a third muon coming from the semi leptonic decay of a B hadron inside the b jet. In the latter case the suppression of the background is certainly better, but the statistic sample is strongly reduced. In both cases I investigated the potential of different techniques and I showed that is possible to have a better discrimination (especially for the case with a third muon) using a Multivariate Analysis.

With the first method (impact parameter and invarian mass b tagging) it is possible to reach a signal efficiency in selecting Z+ b jet event of $\approx 70\%$ a rejection factor of background events of $\approx 60\%$, while with the second method (soft muon tagging) the efficiency is $\approx 90\%$ and the rejection is $\approx 60\%$.

The first method can be useful in a first phase when the statistic will be quite small, while the second (which exploit the third muon in the event) can be used when the statistic will be improved.

In the future the combined use of those methods and the comparison among results ob-

tained with different techniques can provide a powerful tool to control the systematics and templates must be constructed from the best possible signal and background models. Furthermore, I have investigated the possibility to control the mistagging rate directly from data. The b-tagging efficiency can be controlled by looking at the number of tagged jets in data samples that in principle should not contain b jets at first order, like W + jets events. What I have shown is that we expect a mistagging rate per event below the 5% over the full p_T range of the signal.

The uncertainties on signal efficiency and background contamination in the selected sample due to systematic effects have been neglected in this analysis, but important elements of the systematic errors that will affect the cross section measurement of the Z $\rightarrow \mu\mu$ + b jet channel have been enumerated and discussed. The main contributors to systematic uncertainties come from the determination of jet energy scale, the estimation of b-tagging efficiency and rejection and from the uncertainty on the parton content of the proton (PDF). The overall systematic uncertainty on cross section measurement considering these three contributors is expected to be between 15% and 30% depending essentially from the performance and the knowledge of the ATLAS experiment.

Acknowledgements

Il primo grazie va ai miei genitori per avermi aiutata a crescere, a sognare e a capire che le aspirazioni possono essere realizzate, basta crederci davvero! Questo dottorato ne una delle prove.

Un sentito ringraziamento rivolto al Prof. Filippo Ceradini che in questi anni di dottorato mi ha dato la possibilità di continuare ad ampliare le conoscenze nel mondo della fisica lasciando che io seguissi i miei interessi e le mie inclinazioni scientifiche sia per ciò che riguarda la mia formazione che nella realizzazione di questo lavoro.
Un profondo grazie va alla Professoressa Fernanda Pastore che mi ha seguita passo dopo passo durante tutto il periodo della mia formazione universitaria, dagli anni di laurea fino al termine di questo dottorato:grazie per il supporto ma anche per l'affetto.
Grazie alle Dott.sse Ada Farilla, Monica Verducci ed Alessandra Tonazzo che hanno collaborato con me nelle varie fasi di realizzazione di questi tesi con dedizione ed entusiasmo.
Grazie a per aver fatto un po' di chiarezza Voglio ringraziare il Dott. Carlo Carloni Calame per essere riuscito con la sua calma e pazienza, ma anche con la sua simpatia a fare un po' di chiarezza nel buio mundo dei generatori Monte Carlo, il Dott. Iacopo Vivarelli per l'aiuto nelle prime fasi di utilizzo del software di simulazione veloce dell'esperimento(ATLFAST) e il Dott. Federico Nguyen per avermi introdotto sulla misteriosa strada dell'analisi multivariata.
Un grazie indirizzato a tutto il gruppo di ricerca di ATLAS di Roma Tre: grazie alla Dott.ssa Domizia Orestano, al Dott. Toni Baroncelli, al Dott. Mauro Iodice e al Dott. Fabrizio Petrucci per avermi dato la la possibilità di "divagare un po' " dalla fisica dei dati simulati per approcciarmi alla fisica delle calibrazioni delle camere a deriva dello spettrometro a muoni. Tra tutti loro un particolare ringraziamento va a Fabrizio per i suoi consigli e incoraggiamenti anche nei momenti di maggiore difficoltà: grazie per la prontezza e la simpatia!
Un ringraziamento di cuore alla Dott.ssa Manuela Cirilli che è sempre stata il mio punto di riferimento al CERN: grazie per il tempo dedicatomi, ma soprattutto per la cioccolata che ha allietato i miei turni di notte di presa dati di raggi cosmici in Control Room!

Un sincero grazie è indirizzato agli amici che hanno condiviso con me questi anni di dottorato: a Simona-Thelma per le avventure vissute insieme e per la travolgente e contagiosa risata, a Valentino per il suo rincuorante “buongioooorno” seguito dallo “scambiamoci un po’ di affetto” capace di rallegrare le giornate, a Massimiliano per la caparbietà nel cercare di offrirmi caffè su caffè (ci sono voluti quasi 3 anni però alla fine ho accettato!), a Gabriele per il suo “pessimismo cosmico” che non mi ha mai fatto sentire sola, a Cristian e a Luca per aver piacevolmente accorciato le giornate in acquario con pause di chiacchiere e sorrisi, a Fabiola che nonostante la distanza resta sempre l’amica con cui condividere le (dis)avventure del mondo della fisica.
Uno speciale ringraziamento va a Roberto per la pazienza nel rispondere ai miei SOS di natura teorica (forse ora mi è più chiaro cosa sia una scala di fattorizzazione!), ma soprattutto “per tutto il resto”.

Grazie a Marina, la mia migliore amica, per essermi stata sempre accanto, anche nei momenti di dubbi e perplessità nei quali mi sono imbattuta durante questi anni di dottorato: sei davvero una amica speciale!
Un particolare grazie va a Filippo per essermi stato sempre e comunque vicino con morbidi abbracci e rincuoranti parole.

Questi anni di studio e lavoro sono stati allietati da scuole e conferenze nelle quali ho ampliato l’orizzonte delle mie conoscenze sia nel campo della fisica che in quello delle amicizie! E’ per questo che voglio ringraziare tutte le ragazze e i ragazzi con cui ho potuto confrontarmi e con i quali ho condiviso una parte di questo mio percorso. Un grazie speciale va a Nicoletta per le giornate passate insieme tra uffici, control room, caffetteria del CERN e... relais de l’entrecote, a Diego per le impagabili risate, a Rossella per il suo ottimismo e la sua allegria.
Le giornate all’universit non sarebbero certo state le stesse se non avessi potuto condividerle con tutti i miei “figli e nipoti” dell’aula 27! Andrea, Paolo, Michelina, Stefano, Michelangelo, Irene, Laura, Cecilia, Tom, Emilio, Sara Sara, Valina, Simone grazie a tutti voi per le pause pranzo e le chiacchierate! Non pu mancare un ringraziamento al segretario Andrea per i mille favori!!!
La tenacia nel portare avanti questo lavoro è anche il frutto dell’affetto di tanti altri amici e parenti: grazie a Elena, Milena, Agnese, Alessandra, Andrea, Arianna, Caterina, Raffaella, Maria Rosaria, Daniela, Stefano, Giulio, Maria, Erika e Attilio.
Almost last (but not least) I want to thank Moustapha for his help in writing the thesis, but especially for his contagious optimism.

Colgo in ultimo l'occasione per ringraziare tutti quelli che lottano, protestano e manifestano per garantire il diritto allo studio e alla ricerca: è anche grazie a chi crede nel progresso scientifico e ne capisce l'importanza che questo lavoro è stato possibile.

Bibliography

[1] W.-M. Yao et al. *Journal of Physics*, G 33, 1, 2006, http://pdg.web.cern.ch/pdg/pdg.html

[2] C.Quigg *Gauge Theories of the Strong, Weak and Electromagnetic Interactions.* , The Benjamin/Cummings Publishing Company, London, 1983

[3] P.Higgs Phys.Lett.,12:132, 1964

[4] F.Englert and R.Brout Phys. Rev. Lett. 13: 321-23, 1964

[5] G. Guralnik, C. R. Hagen and T. W. B. Kibble Phys. Rev. Let. 13: 585-87, 1964

[6] G.Altarelli, G.Parisi, Nucl. Phys. B126, 289, 1977

[7] S.Dawson, hep-ph ,9612229 ,1997

[8] R.K. Ellis, W.J. Stirling and B.R. Webbwr, *QCD and Collider Physics* , Cambridge Monographs on Particle Physics, Nuclear Physics and Cosmology, 1996

[9] R.K. Ellis, W.J. Stirling and B.R. Webber, *Hard interactions of quarks and gluons: a primer for LHC physics* Rep.Prog.Phys, 70, 89-193, 2007

[10] D. Boussard *et al.*, *The Large Hadron Collider Conceptual Design Report,* CERN/AC, 95-05, 1995

[11] http://lepewwg.web.cern.ch/LEPEWWG/

[12] [ATLAS Collaboration], *The ATLAS Experiment at the CERN Large Hadron Collider*, 2008 JINST 3 S08003

[13] [ATLAS Collaboration], *ATLAS Forward Detectors for Measurement of Elastic Scattering and Luminosity*, CERN/LHCC/2008-004

[14] [CDF Collaboration] *Charged jet evolution and the underlying event in proton antiproton collisions at 1.8-TeV*, Phys.Rev. D, 56, 2002, 092002.

[15] [CDF Collaboration], *The underlying event in hard interactions at the Tevatron anti-p p collider*, Phys.Rev. D, 70, 2004, 072002, [arXiv:hep-ex/0404004]

[16] J. Campbell, R. K. Ellis, F. Maltoni and S. Willenbrock, *Higgs-Boson Production in Association with a Single Bottom Quark*, Phys. Rev. **D 67** (2003) 095002 [arXiv:hep-ph/0204093]

[17] J. Campbell, F. Maltoni *et al.*, *Higgs Boson Production in Association with Bottom Quarks* Phys. Rev., 2004, arXiv:hep-ph/0405302

[18] J. Campbell, R. K. Ellis, F. Maltoni and S. Willenbrock, *Associated Production of a Z Boson and a Single Heavy-Quark Jet*, Phys. Rev. D 69, 074021, 2004, [arXiv:hep-ph/0312024]

[19] *Fermi National Accelerator Laboratory* **http://www.fnal.gov**

[20] The LEP Collaboration Aleph, Delphi, L3, OPAL Collaborations and the LEP Electroweak working group *Precision Electroweak Measurements and Constraints on the Standard Model* CERN-PH-EP/2007-039, arXiv:0712.0929

[21] https://twiki.cern.ch/twiki/bin/view/Atlas/WorkBookAthenaFramework
https://twiki.cern.ch/twiki/bin/view/Atlas/WorkBookPackages.

[22] https://twiki.cern.ch/twiki/bin/view/Atlas/AthenaReleases
https://twiki.cern.ch/twiki/bin/view/Atlas/ReleaseRecipes
http://atlas-computing.web.cern.ch/atlas-computing/projects/releases/status/.

[23] T. Sjöstrand, S. Mrenna and P. Skands, *High Energy Physics Event Generation with PYTHIA6.1,* JHEP05 (2006) 026, (LU TP 06-13, FERMILAB-PUB-06-052-CD-T) [hep-ph/0603175].

[24] T. Gleisberg, S. Höche, F. Krauss, A. Schälicke, S. Schumann, J. Winter, JHEP, 0402, 056,2004

[25] G. Corcella, I.G. Knowles, G. Marchesini, S. Moretti, K. Odagiri, P. Richardson, M.H. Seymour and B.R. Webber, *HERWIG 6.5,* JHEP, 0101-010, 2001; [hep-ph/0011363], [hep-ph/0210213]

[26] M.L. Mangano, M. Moretti, F. Piccinini, R. Pittau, A.D. Polosa, JHEP, 0307, 001, 2003

[27] S. Frixione, B. R. Webber, *The MC@NLO 3.2 Event Generator,* CERN-PH-TH, 2006-012, 2006;

[28] J. Campbell, R.K. Ellis, `http://mcfm.fnal.gov/`;J. Campbell, R.K. Ellis, Phys. Rev. **D**65 113007 (2002).

[29] J.Allison *et al.*, *Geant4 developments and applications* IEEE Transaction on Nuclear Science, 53(1):270-278, 2006

[30] C.Alexa *et al. Geant4 hadronic physics validation with LHC test-beam data: first conclusions.* CERN-LCGAPP, 10, 2004

[31] [ATLAS Computing Group], *Technical design report*, ATLAS TDR, 2005

[32] D. Adams et al., *Track Reconstruction in the ATLAS Muon Spectrometer with MOORE*, ATLAS Note, ATL-SOFT-2003-007, 2003.

[33] Th. Lagouri et al, *A Muon Identification and Combined Reconstruction Procedure for the ATLAS detector at CERN LHC*, IEEE Trans.Nucl.Sci., 51 (2004) 3030-3033.

[34] S.Hassini, *et al.*, NIM A572, 77-79, 2007

[35] S. D. Ellis, J. Huston, K. Hatakeyama, P. Loch and M. Tonnesmann, Prog. Part. Nucl. Phys. **6**0, 484 (2008) [arXiv:0712.2447 [hep-ph]].

[36] M. Cacciari and G. P. Salam, Phys. Lett. B **6**41, 57 (2006) [arXiv:hep-ph/0512210].

[37] A. Abulencia *et al.* [CDF - Run II Collaboration], Phys. Rev. D **7**5, 092006 (2007) [Erratum-ibid. D **7**5, 119901 (2007)] [arXiv:hep-ex/0701051].

[38] D.Cavalli *et al.*, *Performance of the ATLAS fast simulation ATLFAST* ATLAS Note, com-phys-012, 2007

[39] R.Lefevre, C. *In situ determination of the scale and resolution of the jet energy measurements using* $Z^0 + jets$ *events*, ATLAS Internal Note, ATL-PHYS-2002-026, 2002

[40] J. Proudfoot, *et al.*, *Jet Energy Scale Calibration in Vector Boson Events using Rome Simulation Data*, ATLAS Internal Note, ATL-COM-PHYS-2005-067, 2005

[41] [ATLAS Collaboration] *Jet and Missing Et Combined Performance CSC Chapter* ATL-COM-PHYS-2008-074

[42] [ATLAS Collaboration], *ATLAS reference cross-section note*, ATL-COM-PHYS, 2008-077, 2008;

[43] [ATLAS Collaboration] *Standard Model CSC Note* ATL-COM-PHYS-2008-064

[44] S. Correard *et al.*, *b-tagging with DC1 data*, ATL-PHYS-2004-006, (2004)

[45] [ATLAS Collaboration] *b-tagging CSC chapter* ATL-COM-INDET-2008-011

[46] [CDF Collaboration], *Measurement of the b Jet Cross Section in Events with a Z Boson in $p\bar{p}$ Collisions at $\sqrt{s} = 1.96TeV$*, hep-ex/0605099, May 2006

[47] V. M. Abazov *et al.* [D0 Collaboration], *A measurement of the ratio of inclusive cross section $\sigma(pp \to Z + b_{jet})/\sigma(pp \to Z + jet)$ at $\sqrt{s} = 1.96$ TeV*, [arXiv:hep-ex/0410078], (26 Oct 2004)

[48] J. Pumplin, D.R. Stump, J. Huston, H.L. Lai, P. Nadolsky, W.K. Tung, *New Generation of Parton Distributions with Uncertainties from Global QCD Analysis*, hep-ph/0201195, JHEP07, 012, 2002;

[49] A.D.Martin *et al.*, *MRST2001: partons and alpha$_S$ from precise deep inelastic scattering and Tevatron jet data,* Eur.Phys.J ,C23,73, 2002, [hep-ph/0110215]

[50] A.D.Martin *et al.*, *Physical Gluons and High E_T Jets* [hep-ph/0410230]

[51] S.Chekanov *et al.*, *ZEUS next-to-leading-order QCD analysis of data on deep inelastic scattering*, Phys.Rev.D67, 012007, 2003 ;

[52] J. M. Campbell, J. W. Huston and W. J. Stirling, Rept. Prog. Phys. 70, 89 (2007);

[53] A.Hoecker *et al.*, *TMVA, Toolkit for Multivariate Data Analysis with ROOT.* CERN-OPEN-2007-007, June 2007, [arXiv physics/0703039]

[54] R.Brun *et al.*, *ROOT An Object-Oriented Data Analysis Framework* User Guide

[55] http://atlas-sw.cern.ch/cgi-bin/viewcvs-atlas.cgi/offline/Generators/DC3_joboptions/share/

[56] http://projects.hepforge.org/lhapdf/

[57] C.Adloff *et al.*, *Measurement and QCD analysis of neutral and charged current cross sections at HERA* Eur. Phys. J,C30, 1, 2003;[hep-ex:0304003]

[58] S.Alekhin *et al.*, *HERA and the LHC - A workshop on the implications of HERA for LHC physics,* CERN, 2005-014, 2006; [hep-ph/0511119v1]

[59] A. Tricoli, A. Cooper-Sarkar, C.Gwenlan, *Uncertainties on W and Z production at the LHC* CERN, 2005-014, 2005; [hep-ex:0509002]

[60] M.Bellomo, C.Carloni Calame, S. Diglio, M.Malberti, C.Rovelli *W,Z and pdf's measurements with early data in ATLAS and CMS* Nuovo Cimento B 123 3-4 (2008), DOI: 10.1393/ncb/i2008-10554-2

[61] M. Cacciari, E. Laenen, S. Diglio, A. Tonazzo, M. Verducci et. al. *Theoretical review of various approaches in heavy quark production*, CERN-2005-014 (14 December 2005)[arXiv:hep-ph/0601012-3]

[62] S.Diglio, A.Farilla, A.Tonazzo, M.Verducci, *Associated production of a Z boson and a b-jet in ATLAS* ATL-PUB-PHYS, 2007-014, 2007; [hep-ex:0710.4461]

[63] E.Dobson *W/Z+jets studies in ATLAS* ATL-COM-PHYS-2008-091